Modeled and observed properties related to the direct aerosol radiative effect of biomass burning aerosol over the Southeast Atlantic

Sarah J. Doherty[1,2], Pablo E. Saide[3,4], Paquita Zuidema[5], Yohei Shinozuka[6,7], Gonzalo A. Ferrada[8], Hamish Gordon[9], Marc Mallet[10], Kerry Meyer[11], David Painemal[12,13], Steven G. Howell[14], Steffen Freitag[14], Amie Dobracki[5], James R. Podolske[7], Sharon P. Burton[13], Richard A. Ferrare[13], Calvin Howes[3], Pierre Nabat[10], Gregory R. Carmichael[8], Arlindo da Silva[15], Kristina Pistone[6,7], Ian Chang[16], Lan Gao[16], Robert Wood[2] and Jens Redemann[16]

[1] Cooperative Institute for Climate, Ocean and Ecosystem Studies, Seattle, WA, USA
[2] Department of Atmospheric Science, University of Washington, Seattle, WA, USA
[3] Department of Atmospheric and Oceanic Sciences, University of California, Los Angeles, CA USA
[4] Institute of the Environment and Sustainability, University of California, Los Angeles, CA, USA
[5] Rosenstiel School of Marine and Atmospheric Science, University of Miami, Miami, FL, USA
[6] Bay Area Environmental Research Institute, Moffett Field, CA, USA
[7] NASA Ames Research Center, Moffett Field, CA, USA
[8] Center for Global and Regional Environmental Research, The University of Iowa, Iowa City, IA, USA
[9] Engineering Research Accelerator and Center for Atmospheric Particle Studies, Carnegie Mellon University, Pittsburgh, PA, USA
[10] CNRM, Université de Toulouse, Météo-France, CNRS, Toulouse, France
[11] NASA Goddard Space Flight Center, Greenbelt, Maryland, MD 20771, USA
[12] Science Systems and Applications Inc., Hampton, Virginia 23666, USA
[13] NASA Langley Research Center, Hampton, Virginia 23691 USA
[14] University of Hawaii at Manoa, Honolulu, HI, USA
[15] Global Modeling and Assimilation Office, NASA Goddard Space Flight Center, Greenbelt, MD, USA
[16] School of Meteorology, University of Oklahoma, Norman, OK, USA

Correspondence to: Sarah J. Doherty (sarahd@atmos.washington.edu)

Abstract. Biomass burning smoke is advected over the southeast Atlantic Ocean between July and October of each year. This smoke plume overlies and mixes into a region of persistent low marine clouds. Model calculations of climate forcing by this plume vary significantly, in both magnitude and sign. The NASA EVS-2 (Earth Venture Suborbital-2) ORACLES (ObseRvations of Aerosols above CLouds and their intEractionS) project deployed for field campaigns off the west coast of Africa in three consecutive years (Sept., 2016; Aug., 2017; and Oct., 2018) with the goal of better characterizing this plume as a function of the monthly evolution, by measuring the parameters necessary to calculate the direct aerosol radiative effect. Here, this dataset and satellite retrievals of cloud properties are used to test the representation of the smoke plume and the underlying cloud layer in two regional models (WRF-CAM5 and CNRM-ALADIN) and two global models (GEOS and UM-UKCA). The focus is on comparisons of those aerosol and cloud properties that are the primary determinants of the direct aerosol radiative effect, and on the vertical distribution of the plume and its properties. The representativeness of the observations to monthly averages are tested for each field campaign, with the sampled mean aerosol light extinction

generally found to be within 20% of the monthly mean at plume altitudes. When compared to the observations, in all models the simulated plume is too vertically diffuse, has smaller vertical gradients, and, in two of the models (GEOS and UM-UKCA), the plume core is displaced lower than in the observations. Plume carbon monoxide, black carbon, and organic aerosol masses indicate under-estimates in modeled plume concentrations, leading in general to under-estimates in mid-visible aerosol extinction and optical depth. Biases in mid-visible single scatter albedo are both positive and negative across the models. Observed vertical gradients in single scatter albedo are not captured by the models, but the models do capture the coarse temporal evolution, correctly simulating higher values in October (2018) than in August (2018) and September (2017). Uncertainties in the measured absorption Ångstrom exponent were large but propagate into a negligible (<4%) uncertainty in integrated solar absorption by the aerosol and therefore in the aerosol direct radiative effect. Model biases in cloud fraction, and therefore the scene albedo below the plume, vary significantly across the four models. The optical thickness of clouds is, on average, well simulated in the WRF-CAM5 and ALADIN models in the stratocumulus region and is under-estimated in the GEOS model; UM-UKCA simulates significantly too-high cloud optical thickness. Overall, the study demonstrates the utility of repeated, semi-random sampling across multiple years that can give insights into model biases and how these biases affect modeled climate forcing. The combined impact of these aerosol and cloud biases on the direct aerosol radiative effect (DARE) is estimated using a first-order approximation for a sub-set of five comparison gridboxes. A significant finding is that the observed gridbox-average aerosol and cloud properties yield a positive (warming) aerosol direct radiative effect for all five gridboxes, whereas DARE using the gridbox-averaged modeled properties ranges from much larger positive values to small, negative values. It is shown quantitatively how model biases can offset each other, so that model improvements that reduce biases in only one property (e.g., single scatter albedo, but not cloud fraction) would lead to even greater biases in DARE. Across the models, biases in aerosol extinction and in cloud fraction and optical depth contribute the largest biases in DARE, with aerosol single scatter albedo also making a significant contribution.

1 Introduction

Climate forcing by both direct aerosol-radiation interactions and aerosol-cloud interactions offsets about a third of greenhouse gas forcing and also contributes the largest uncertainty to total anthropogenic forcing (Forster et. al., 2021). Forcing by aerosols is, in general, dependent on the vertical location of the aerosol relative to clouds, and especially so for absorbing aerosol (e.g., Samset et al., 2013). In the Southeast Atlantic region this is particularly true. From August through October there is a spatially broad, high-concentration smoke plume that overlies, and in places and times mixes with, a persistent boundary layer cloud deck. As such, direct radiative forcing in the region is a strong function not only of smoke concentration, composition and vertical distribution, but also of the albedo below the plume. Over the SE Atlantic, this albedo is arguably driven primarily by cloud fraction and liquid water path, as well as by cloud droplet number concentration, with the latter controlled by aerosol-cloud microphysical interaction. Large-scale models have been shown to

have large uncertainties and biases in their simulations of both aerosol absorption (e.g., Sand et al., 2021; Brown et al., 2021) and low marine clouds (e.g., Noda and Sato, 2014; Kawai and Shige, 2020) in this region.

Modeled direct radiative forcing across the SE Atlantic has ranged from strongly negative to strongly positive, with much of this range determined by modeled cloud fraction (e.g., see Figure 2 of Zuidema et al., 2016 and Stier et al., 2013). In one study, the direct aerosol radiative effect in the region changed from negative to positive as cloud fraction increased above 40% (Chand et al., 2009), assuming a mid-visible aerosol single scatter albedo (SSA) of 0.85 and for cloud optical depths averaging 7.8 (or cloud albedo of 0.5). For aerosol with lower SSA or for higher cloud albedo this transition would occur at a lower cloud fraction (Mallet et al., 2020). The sign and magnitude of the responses to this forcing (i.e. cloud adjustments formerly referred to as the "semi-direct effect") also depend strongly on the underlying cloud properties and the relative vertical locations of the aerosol and cloud (e.g. Penner et al., 2003; Johnson et al., 2004; Sakaeda et al., 2011; Bond et al., 2013; Matus et al, 2015). Absorbing aerosol aloft has been linked to increased lower tropospheric stability and enhanced cloud cover and thickness, compared to cleaner environmental conditions. This has been attributed to heating of the air aloft, limiting the entrainment of dry air from the free troposphere into the marine boundary layer (Wilcox, 2010; Gordon et al., 2018), in turn enhancing low cloud cover (e.g., Johnson et al., 2004; Wilcox, 2010), with Herbert et al. (2020) indicating a dependence on the cloud-aerosol layer distance. However, if the aerosol mixes into the clouds, atmospheric heating there may reduce cloud cover (Koch and Del Genio, 2010; Zhang and Zuidema, 2019).

The large uncertainty in aerosol climate forcing in the SE Atlantic was the impetus for the NASA ORACLES (ObseRvations of Aerosols above CLouds and their intEractionS) project, funded through the NASA Earth Venture Suborbital (EVS-2) program (Redemann et al., 2021), as well as complementary campaigns (Zuidema et al., 2016; Formenti et al., 2019; Haywood et al., 2021). The ORACLES project explicitly measured aerosol properties necessary to calculate the direct aerosol radiative effect (DARE). The campaign included deployments of the NASA P-3 research aircraft to the SE Atlantic region based out of Walvis Bay, Namibia (27 August-27 September 2016) and São Tomé, São Tomé e Príncipe (09 August-02 September 2017 and 24 September-25 October 2018). The NASA ER-2 aircraft also deployed to Walvis Bay 26 August-29 September 2016. The P-3 carried a suite of instruments to measure in-situ gas concentrations and aerosol microphysical, optical and chemical properties, to measure cloud microphysical properties, and to remotely sense both aerosols and clouds. It generally flew between 100m and 6km above the sea surface, capturing in-situ data in ramped or spiral profiles, horizontal variations in level legs, and aerosol and trace gas columnar properties (e.g., aerosol optical depth, AOD) when flying below aerosol layers. The ER-2 flew at high altitude (19 km) and carried remote sensing instruments only, observing both aerosols and clouds. (See Redemann et al., 2021 for a more complete overview of the ORACLES campaigns).

Here, aerosol and cloud properties observed during the three ORACLES deployment periods are compared to two regional models, the Weather Research and Forecasting model coupled with the physics package of Community Atmosphere Model

105 (WRF-CAM5) and the Centre National de Recherches Aire Limitée Adaptation dynamique Développement InterNational model (CNRM-ALADIN; hereafter simply ALADIN) and two global models, the Goddard Earth Observing System model (GEOS) and the United Kingdom Chemistry and Aerosols Unified Model (UM-UKCA). Descriptions of each model are given below. The WRF-CAM5 and GEOS models are included because they were used for aerosol and meteorological forecasting during the ORACLES campaign. Similarly, the UM-UKCA modeling team participated in the U.K. CLARIFY

110 (Cloud-Aerosol-Radiation Interactions and Forcing) campaign, which deployed out of Ascension Island (**Figure 1**) in 2017 (Haywood et al., 2021). In 2016 both ORACLES and the French AEROCLO-SA (AEROsol radiation and CLOuds in Southern Africa; Formenti et al., 2019) campaign deployed out of Walvis Bay, Namibia, with the latter focusing on near-coast aerosols. The ALADIN regional model version 6 used here (Mallet al., 2019, 2020; Nabat et al., 2020) simulated aerosol and clouds over the SE Atlantic as part of the AEROCLO-SA campaign.
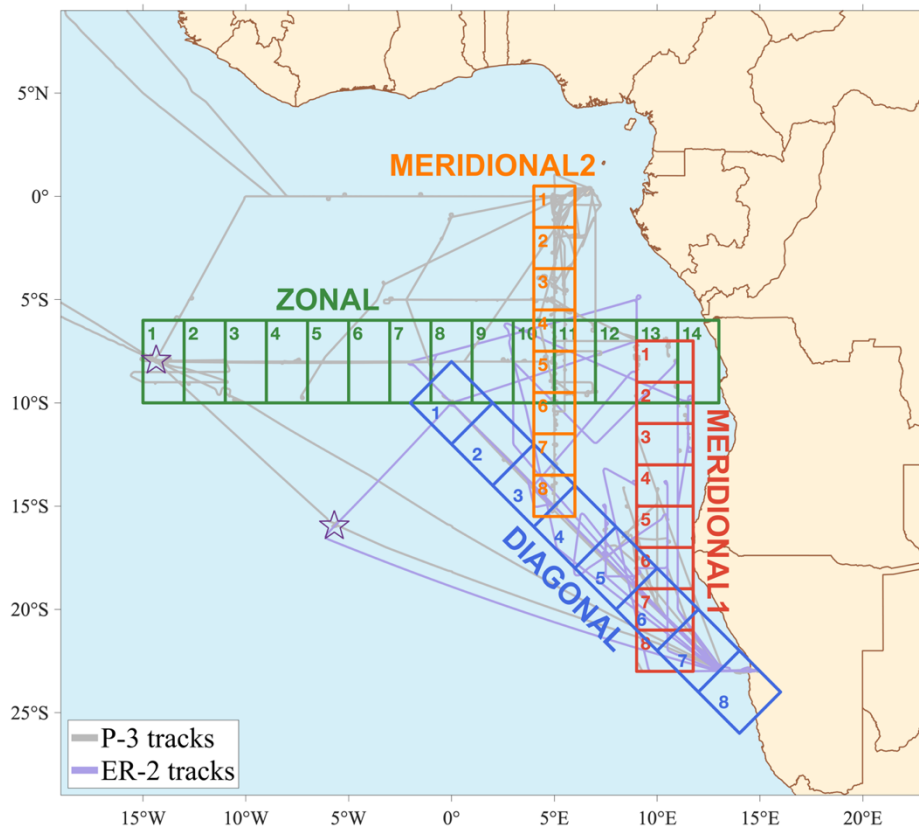
Figure 1. The four transects used in the model-observation comparison are shown along with the P-3 (2016, 2017 and 2018) and ER-2 (2016) aircraft flight tracks. Gridboxes within each transect are numbered from north/west to south/east. See Supplementary Table S.1 for the gridbox coordinates. The locations of Ascension Island (8S, 14W) and St. Helena Island (16S, 6W) are shown as stars.

The properties included here (Section 2.1) allow for a first-order calculation of DARE (Section 5). Forcing through aerosol-cloud interactions is driven by a more complex set of processes – including the time-history of aerosols and clouds (Diamond et al. 2018), aerosol physical and chemical properties (e.g., McFiggans et al., 2006; Kacarab et al., 2020), the micro- and macro-physical properties of the clouds (e.g. Stevens and Feingold, 2009; Koren et al., 2014; Gupta et al., 2021), and the thermodynamic state of the atmosphere. There is limited treatment herein of this broader set of variables, though testing model accuracy in representing cloud fraction does provide a critical zero-order step toward determining whether models might be capturing processes key to quantifying forcing through aerosol-cloud interactions.

This study builds on Shinozuka et al. (2020), which compared modeled and observed column aerosol properties for the September 2016 ORACLES deployment only. There, comparisons were presented as box-whisker plots of two-dimensional (2D; i.e. column) and three-dimensional (3D) variables. For 3D variables, values were binned into three discrete layers: the marine boundary layer, the free troposphere below 3 km, and 3-6 km altitude. The Shinozuka et al. (2020) study focused on comparisons of layer-average carbon monoxide (CO) and aerosol properties, as well as the smoke layer bottom and top altitudes. Comparisons were made to six models: in addition to the four included herein, the EAM-E3SM and GEOS-Chem models provided statistics for the variables analyzed in Shinozuka et al. (2020).

2 Comparison overview

The comparisons presented here focus on vertically-resolved aerosol properties, where data are averaged into 500 m altitude bins from the surface up to 6 km, and on the clouds below the biomass burning smoke plume. The observed and modeled aerosol and cloud properties are compared for multiple transects across the southeast Atlantic (**Figure 1**). Observed values of the aerosol properties are from the ORACLES research flights, while observed cloud properties are from satellite retrievals, since calculation of cloud fraction and optical depth from observations made from the aircraft are too limited to be of use in the statistical comparison presented here.

2.1 Comparison variables

The focus is on variables that are strongly related to the direct aerosol radiative effect of biomass burning aerosol. Vertically-resolved comparisons are made for the following variables measured in-situ from the NASA P-3, and measured with the high-spectral-resolution lidar, HSRL-2 (σ_{ep} only), which deployed on the ER-2 in 2016 and the P-3 in 2017 and 2018:

- Carbon Monoxide (CO) mixing ratio
- Black Carbon (BC) concentration
- Organic Aerosol (OA) concentration
- Light extinction (σ_{ep}) [530nm from the in situ observations; 532nm from the HSRL-2; 550nm from the models]

- Single Scatter Albedo (SSA) [530nm from the observations; 550nm from the models]
- Aerosol Absorption Ångström Exponent (AAE) [440-670nm for the observations; 400-600nm for the WRF-CAM5, GEOS and ALADIN models; 380-550nm for UM-UKCA]
- Aerosol Scattering Ångström Exponent (SAE) [440-670nm for the observations; 400-600nm for the WRF-CAM5, GEOS and ALADIN models; 380-550nm for UM-UKCA]
- Relative Humidity (RH)

The aerosol optical properties σ_{ep}, SSA, AAE, and SAE are measured in-situ at low RH. The values of σ_{ep} retrieved from HSRL-2 and simulated by all four models are reported at ambient RH; the UM-UKCA model additionally reports dry σ_{ep}.

The properties most critical to the underlying cloud albedo – the cloud fraction and cloud optical thickness – are evaluated by comparing 2D

- mean warm cloud fraction (CF_{warm})
- geometric mean warm cloud optical thickness (COT_{warm})

from the models to those retrieved from the polar-orbiting MODerate resolution Imaging spectroradiometer (MODIS; CF_{warm} and COT_{warm}) and geostationary Spinning Enhanced Visible and InfraRed Imager (SEVIRI; CF_{warm} only).

2.2 Comparison transects, altitude bins and statistics

Comparisons are made along several transects of gridboxes (**Figure 1** and Supplemental **Table S.1**). The locations of the transects are dictated by frequent research flight paths, which varied across the three years of the project. A decided focus of the ORACLES field campaigns was to devote about half of the P-3 flight hours in each year to sampling along "Routine" flight tracks (Redemann et al., 2021). The explicit goal was to sample the transect across a set of randomly-distributed days throughout the field deployment in order to build a dataset representative of the deployment month.

During ORACLES 2016 the Routine flights followed a diagonal latitude/longitude transect (Diagonal transect, **Figure 1**, terminating near Namibia). With deployment based out of São Tomé in 2017 and 2018, the Routine flights were along a north-south oriented track centered on 5E (Meridional2, **Figure 1**). The Routine flight pattern usually consisted of a series of in-transit profiles and horizontal legs in the aerosol layer and in the boundary layer clouds. In 2017 and 2018, with the HSRL-2 lidar on board the P-3, the south-bound leg on Routine flights was usually flown at an aircraft maximum altitude (approximately 5-6 km) to survey the aerosol and cloud layers below. The north-bound run was then a combination of vertical profiling, horizontal legs, and sawtooth legs (for clouds). Each Routine flight included a different combination of legs and profiles, so only the latitude/longitude line of the flights (not their altitudes) were common to all. In 2016, on most Routine flight days the NASA ER-2 would also fly along the Routine track and, in some cases, overfly the P-3.

In addition to the dedicated Routine track in 2016, a significant number of P-3 Target of Opportunity flights (Redemann et al., 2021) were flown along a north-south transect near the southern African coast. As such, the Meridional1 (**Figure 1**) set of comparison gridboxes is also selected. Finally, for all three years a Zonal transect is established running from Ascension Island to the west African coast. The Zonal transect is located approximately at the latitudinal center of the southern African biomass burning plume, along the northern edge of the main stratocumulus deck. Free troposphere transport in this region is driven by the southern African Easterly Jet, which is centered around 8°S (Adebiyi and Zuidema, 2016); as such, in the free troposphere the Zonal transect, to first order, covers a gradient in age from east (younger) to west (more aged).

The Zonal transect is located significantly farther from the deployment bases than the other comparison transects, so most gridboxes in this transect have little P-3 data. In 2016, only the ER-2 had sufficient sampling for meaningful comparisons with models along this transect. In 2017, when the P-3 did a "suitcase" flight to Ascension Island (Redemann et al., 2021) there was some coverage of the western-most Zonal gridboxes. For the Zonal transect, the only aerosol observations included in the comparison are profiles of σ_{ep} from the HSRL-2 on board the ER-2 in 2016. In all three years, comparisons of CF_{warm} and COT_{warm} are included along the Zonal transect, since these observations are from satellite and so have good statistics in all three years.

In the discussions below, gridboxes are numbered from northwest to southeast for the Diagonal transect, north to south for the two Meridional transects, and west to east for the Zonal transect (**Figure 1**). Averages within each deployment year cover the following dates:

- 30 August through 27 September, 2016;
- 9 August through 2 September, 2017; and
- 24 September through 25 October 2018.

These include the transit flights from Namibia (2016) and to and from São Tomé (2017 & 2018). For ease, we refer to these as the September 2016, August 2017 and October 2018 monthly averages.

Observed and modeled statistics are calculated for 500 m deep altitude bins from the surface to 6km, with two exceptions. Relative humidity is aggregated into 250m deep bins to more clearly show the transition from the boundary layer to the free troposphere. Light extinction from the HSRL-2 has 315 m vertical resolution, and this resolution is retained. Mean biases are calculated as averages of ratios in 1 km altitude bins for more robust statistics. For the in-situ observations, data are included in statistics whether made on level legs or during profiles, so the number of datapoints included in statistics can vary significantly with altitude within a given gridbox (**Figure 2**).

The aerosol properties compared here were measured from the aircraft, and so are available on specific days and for specific locations on each flight. In the aerosol comparisons, the model statistics used are calculated for only those dates and locations where the aircraft was present. In contrast, the observed CF_{warm} and COT_{warm} statistics are from satellite-based
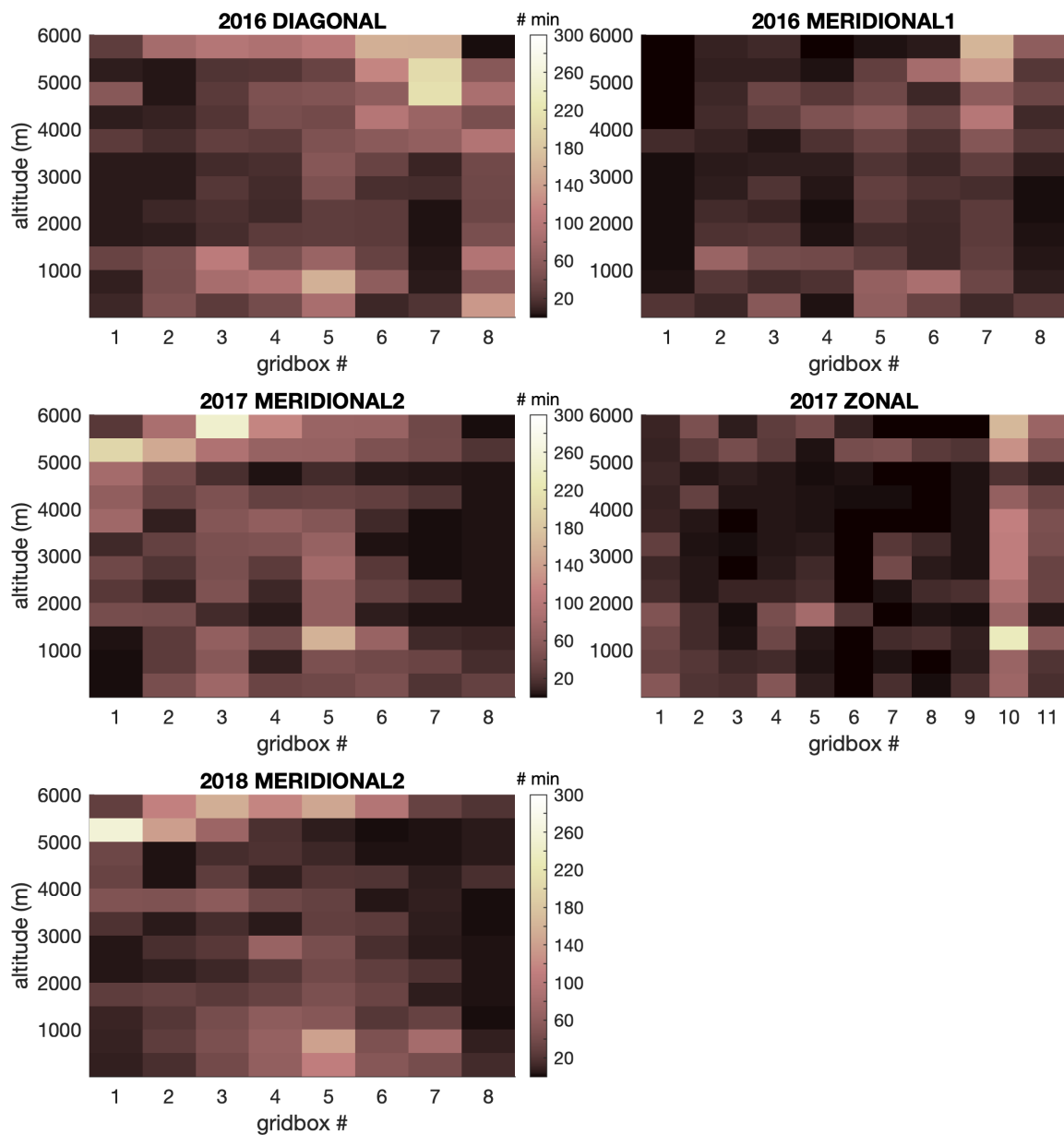
Figure 2. The number of minutes the P-3 aircraft spent in each gridbox and 500m altitude bin for the comparison transects shown in Figure 1. The 2016 Diagonal and 2017 and 2018 Meridional2 transects cover "Routine" flight tracks, which targeted semi-random sampling. Not all in-situ measurements have data available for all times, so the number of minutes of available data may be less than the number of minutes the P-3 was present in a given gridbox and altitude bin.

8

225 measurements (Section 3.2) and so are available for every day of each year's deployment. In this case, both observed and model statistics are calculated for every day of the deployment period across every comparison gridbox.

To test for the representativeness of the observed aerosol properties, for some variables two sets of modeled statistics are calculated for each gridbox and altitude layer: first for only those locations and times when the aircraft was present, and

230 second for all daylight hours (defined here as 06:00-18:00 UTC) across the duration of that years' deployment. Comparison of the two allows for testing the representativeness of the observations for assessing monthly averages, assuming the model realistically captures aerosol variability. To test this, we calculated the fractional variability in σ_{ep} in the 2-5km altitude range within the comparison gridboxes in the WRF-CAM5 and GEOS models and in the observations. We found that the three are similar for the 2016 Diagonal and Meridional1 transect gridboxes, with the models alternately having lower and higher

235 fractional variability than was observed. Along the 2017 Meridional2 transect, WRF-CAM5 and the observed variability were similar but the GEOS variability was 10-30% higher. Along the 2018 Meridional2 transect the converse was true: the relative variability in σ_{ep} was similar for GEOS and the observations, but was about 20% lower for WRF-CAM5.

Shinozuka et al. (2020) also tested the representativeness of observed column properties (aerosol optical depth) for the

240 September, 2016 campaign only. The vertically-resolved data provide additional, more detailed information on representativeness, something columnar passive satellite observations cannot provide. In addition, here representativeness is tested for all three campaign years.

3 Dataset descriptions

3.1 Observed aerosol properties, CO concentrations & relative humidity

245 Detailed descriptions of the instruments used to measure aerosols and gases are given in Appendix 9.1 of Shinozuka et al. (2020). Here, the characteristics of each measurement most relevant to the presented comparison are discussed. All in-situ observations are derived from the 1 sec resolution data collected on the P-3, available on the NASA public data archive (see Data Availability). Several of the measurements used here (e.g., absorption; see below) are very noisy at this resolution. To reduce noise the 1 sec resolution data are smoothed using a weighted average, calculated with a Gaussian weighting function

250 covering ±30 sec on either side of each 1 sec resolution data point. The weighting function has 61 values, with the peak at value 31. The standard deviation was set to 12; this produces a weighting function such that the data points at time t-30 sec and t+30sec are weighted at 4.4% of the value at time t. A much larger standard deviation would have weighted values more than 30sec from the time of interest too heavily (e.g. by 17% for a value of 16), and a much smaller standard deviation would have produced a weighting function that approached zero in less than 30sec. Values of in-situ σ_{ep}, SSA, SAE and AAE are

255 derived after this smoothing function is applied to the scattering and absorption data. In all cases, statistics for a given

altitude bin and comparison gridbox are included for the in-situ observations only if at least 10 min of data in total are available.

Aerosol optical properties were measured in-situ at low (<40%) RH via an aerosol inlet with a 50% cut-off diameter of approximately 5μm (McNaughton et al., 2007). Above the boundary layer, the aerosol during ORACLES was dominated by accumulation mode biomass burning smoke with a volumetric mean diameter of <0.4μm (e.g. see Figure 8 of Shinozuka et al., 2020), so it is expected that the in-situ instruments capture the properties of the vast majority of aerosol contributing to column radiative impacts and all of the biomass aerosol.

Carbon monoxide was measured with an ABB/Los Gatos Research $CO/CO_2/H_2O$ Analyzer modified for flight operations, with a precision of 0.5 ppbv for 10 sec averages (Liu et al., 2017; Provencal et al., 2005). Black carbon was measured as refractory BC (rBC) using a Single Particle Soot Photometer (SP2) (Schwarz et al., 2006; Stephens et al., 2003) calibrated with Fullerene soot. The SP2 measurement of rBC mass is estimated to have an uncertainty of 25% at the provided 1 sec resolution. A High-Resolution Time of Flight Aerodyne aerosol mass spectrometer (HR-ToF-AMS), operated in high sensitivity V-mode, was used to measure organic aerosol (OA) mass with an estimated accuracy of 50% at 1 sec time resolution.

Aerosol light scattering (σ_{sp}) at 450, 550, and 700 nm was measured on board the P-3 at low (<40%) RH with a TSI model 3563 nephelometer, with the corrections of Anderson and Ogren (1998) applied. In 2018, two TSI nephelometers were operated, with one periodically measuring sub-micron aerosol only. When both were measuring the total aerosol, reported σ_{sp} is the average of the two. In 2018, the 450 nm channel on the nephelometer wasn't working, so SAE data are not available for that year.

As discussed below, most models report aerosol optical properties at ambient RH. Relative humidity profiles and aerosol hygroscopic growth factors inform whether this could be a significant source of differences between the modeled and observed aerosol optical properties and so are shown here. The observed ambient RH was calculated based on dew point measured using an Edgetech 137 Vigilant hygrometer. Hygroscopic growth factors for 530nm light scattering were quantified during ORACLES using a pair of Radiance Research nephelometers, run at low (<40%) RH and approximately 85% RH respectively. However, there were instrumental issues that resulted in significant data gaps in 2016 and 2018, and instrumental problems across the full 2017 campaign. This complicates correcting to humidified scattering values for the statistical comparisons with the models. As such, here we use these data only to estimate the effect of humidification on scattering, based on aerosol characteristics aggregated across all observations (not just those in the comparison transects) within each field season.

290   Dry aerosol light absorption (σ_{ap}) at 470, 530, and 660nm was calculated using measurements from one (2017 and 2018) or two (2016) three-wavelength Radiance Research Particle Soot Absorption Photometers (PSAPs). For 2016, the values from the two PSAPs are averaged; for 2017 and 2018 only one of the PSAPS consistently measured the total ambient aerosol absorption, so only data from that PSAP was used. Filter-based absorption measurements such as the PSAP are known to have loading-based artefacts that produce a positive bias that requires correction (e.g. Bond et al., 1999; Virkkula, 2010).

295   Early versions of the PSAP instrument measured σ_{ap} at only one wavelength, 530nm, so correction factors at this wavelength are better understood than at 470 and 660nm, where they are untested for accuracy. Here, two sets of correction factors have been applied to the PSAP data: the wavelength-averaged and the wavelength-specific corrections, both described in Virkkula (2010). These correction factors are very similar at 530nm but yield different values of σ_{ap} at 470nm and 660nm. They therefore yield different values of derived absorption Ångström exponent, but nearly identical 530nm SSA.

300

Scattering at the 450, 550, and 700 nm wavelengths (λ) is used to calculate a linear fit to log(σ_{sp}) versus log(λ), yielding the scattering Ångström exponent, SAE. The absorption Ångström exponent, AAE, is analogously calculated from σ_{ap} at 470nm, 530nm, and 660nm for, as noted above, σ_{ap} derived using the two sets of Virkkula (2010) correction factors. The observed values of σ_{ep} and SSA included here are at 530nm, for low-RH aerosol. They are calculated by adjusting the measured, low-

305   RH 550nm σ_{sp} with the above-calculated SAE. This adjusted σ_{sp} is then summed with the 530nm σ_{ap} to get σ_{ep}, and SSA is calculated as the ratio of 530nm σ_{sp} to 530nm σ_{ep}. SAE and SSA are calculated only when σ_{ep} is greater than 10 Mm^{-1} and AAE is only calculated when σ_{ap} is greater than 5 Mm^{-1} in order to avoid including data dominated by noise.

All of the above measurements were made from the P-3 aircraft. Data from the airborne second-generation High Spectral

310   Resolution Lidar version 2 (HSRL-2) that was flown on the ER-2 aircraft in 2016 and the P-3 in 2017 and 2018 are also included in the comparison. The HSRL-2 is a remote-sensing instrument so retrieved values of σ_{ep} are at ambient RH, and therefore are more directly comparable to the modeled values. The HSRL-2 independently detects backscatter from aerosols and molecules using the spectral distribution of the returned signal, thereby retrieving σ_{ep} without having to make assumptions about the backscatter-to-extinction ratio of the aerosol (Shipley et al., 1983; Hair et al., 2008; Burton et al.,

315   2018). The HSRL-2 retrieves σ_{ep} at 355nm and 532nm with 315m vertical resolution; here we use the 532nm data only for comparison to modeled 550nm σ_{ep}.

3.2 Observed cloud properties

From the standpoint of aerosol forcing, the clouds of most interest in the SE Atlantic are Stratocumulus and Cumulus (warm, low) clouds in the boundary layer, as these clouds are most prevalent in the region and underlie the aerosol plume, so they

320   are a strong controlling factor on the direct aerosol radiative effect sign and magnitude. As such, here we compare the warm, low cloud (<2.5km, T>273K) fraction (CF$_{warm}$) from models to that retrieved in several satellite products.

11

Cloud optical thickness for these clouds (COT$_{warm}$) is approximately lognormally distributed (e.g. Supplemental **Figure S.1**), so for COT$_{warm}$ we compare the geometric mean of all values within the comparison gridboxes. This statistic was selected as the most physically meaningful, since it more closely represents the cloud optical thickness, and therefore cloud impact on scene albedo, for heterogeneous scenes.

CF$_{warm}$ and COT$_{warm}$ are derived for several retrieval products and are compared to each other as well as to the observations. As described later (Section 4.4) the SEVIRI-LaRC values of CF$_{warm}$ (Section 3.2.3) and the MODIS-ACAERO values of COT$_{warm}$ (Section 3.2.2) are used as the benchmark for the comparison to the modelled values.

3.2.1 MODIS-Standard cloud products

The Collection 6 MODIS Level 3 (L3) daily cloud products (Platnick et al., 2015a) from both the Aqua (MYD08) and Terra (MOD08) satellites are used to calculate average warm cloud fractions, CF$_{warm}$. These L3 products are statistical aggregations at 1°x1° resolution (latitude x longitude) of the MODIS Level-2 pixel-level cloud retrievals (Platnick et al., 2015b; Platnick et al., 2017). Since Aqua and Terra are polar-orbiting satellites, their cloud retrieval statistics from the ORACLES comparison gridboxes are from, on average, 10:20 local (Terra) and 13:40 local (Aqua). Herein we refer to these as the "MODIS-Standard" retrieved cloud properties.

The L3 MODIS variables used for CF$_{warm}$ are Cloud_Retrieval_Fraction_Liquid and Cloud_Retrieval_Fraction_PCL_Liquid, with the latter allowing for inclusion of partly-cloudy pixels. Data are excluded from statistics if the retrieved cloud top height is greater than 2.5 km, in order to include only low warm clouds. These variables only include the Level-2 pixel population that is identified as liquid phase, overcast, and that has successful cloud optical property retrievals, allowing classification as liquid clouds. As such, CF$_{warm}$ may be smaller than the actual warm cloud fraction, depending on the rate of cloud optical property retrieval failure (see, e.g., Cho et al., 2015) and the prevalence of broken clouds and cloud edges in a retrieval pixel. For the selected comparison transects – and for this region in general – the fraction of mid-level and high clouds is low. For example, in 2016 warm, low clouds comprise, on average, 93% or more of the clouds in the Diagonal and Meridional1 transect gridboxes and the four eastern-most Zonal transect gridboxes. In the seven western-most Zonal gridboxes >99% of the clouds are warm clouds. An exception is the gridboxes closer to the African coastline, where mid-level clouds in particular can be more frequent. This is consistent with the fact that most mid-level and high clouds in the region originate over the continent (Adebiyi et al., 2020), a phenomenon we observed directly during the field campaigns.

3.2.2 MODIS-ACAERO cloud products

Retrievals of cloud properties from satellite imager-based observations can be affected by the presence of aerosol above the clouds, particularly when that aerosol is light-absorbing (Haywood et al., 2004; Coddington et al., 2010; Meyer et al., 2013).

While retrieved CF is not significantly impacted, the retrieved COT will be. If not accounted for, the attenuation of cloud-reflected solar radiation due to aerosol absorption can be interpreted by satellite imager cloud retrieval algorithms as higher effective radii and as a lower COT. Therefore, in addition to the MODIS-Standard cloud retrievals we calculate cloud statistics using the L2 (1 km resolution) MOD06/MYD06ACAERO retrievals from MODIS that use the Meyer et al. (2015) approach, which accounts for the effects of the absorbing aerosol layer above low clouds and has been shown to produce COT values that compare better to aircraft-based observations than the MODIS-Standard product (Chang et al., 2021). These retrievals, referred to here as MODIS-ACAERO, simultaneously retrieve the above-cloud aerosol optical properties and the unbiased cloud optical properties, and are used as the reference for observed COT_{warm}. (Specifically, the Cloud_Optical_Thickness_ModAbsAero parameter is used). The MODIS-ACAERO retrieved CF_{warm} is also included, which differs from the MODIS-Standard definition in its use of cloud-top height (CTH) as an additional filter (specifically, CTH < 4km, thus excluding mid-level clouds). Otherwise, as with the MODIS-Standard retrievals, these are averages from the MODIS instruments on the Terra and Aqua satellites.

3.2.3 SEVIRI-LaRC cloud products

Warm clouds over the SE Atlantic have a significant diurnal cycle, particularly in cloud fraction (Rozendaal et al, 1995; Wood et al., 2002; Painemal et al., 2015). A question is whether the MODIS retrievals, which make observations only twice daily, are representative of the daytime averages. The Spinning Enhanced Visible and Infrared Imager (SEVIRI) on the geostationary satellite Meteosat-10 views the SE Atlantic region at all times of day. We use the cloud fraction retrieved from SEVIRI for three purposes: First, we calculate the average daytime CF_{warm} in each comparison gridbox, for testing the modeled average daytime CF_{warm}. Second, we calculate the difference in the average daytime CF_{warm} and the average of CF_{warm} at 10:30UTC and 13:30UTC only, as an estimate for how different CF_{warm} from the MODIS Terra and Aqua retrievals might be from an actually full daytime average of CF_{warm}. Third, as described below, we use the diurnal cycle in CF_{warm} to infer the diurnal cycle in COT_{warm}, and therefore the representativeness of the MODIS-ACAERO Terra+Aqua COT_{warm} to the daytime average.

Here, the SEVIRI retrievals described by Minnis et al. (2008; 2011a; 2011b) and Painemal et al. (2015) are used and are referred to as the SEVIRI-NASA Langley Research Center (LaRC) retrievals. Warm cloud fractions are derived at 0.25° grid resolution from pixel-level (3 km) retrievals by counting pixels with "liquid" cloud phase and the effective cloud top temperature $T_{cldtop} > 273.2K$. Retrievals are provided every 30 minutes. We limit our analysis to daytime samples with solar zenith angles (SZA) of less than 75˚ to minimize retrieval uncertainties in the day-night transition.

In this region, cloud cover tends to be at a maximum in early morning, then either decreases throughout the day or decreases until mid- to late afternoon and then again increases (**Figure S.2**; Painemal et al., 2015). The average of CF_{warm} at 10:30+13:30 is generally lower than but within 5% of the daytime average (**Table S.2**). The exception is at the north end of

13

the Meridional1 and Meridional2 transects, when the 10:30+13:30 average is up to 14% below the daytime average. While the 10:30+13:30 average CF_{warm} is lower than the daytime average, it does represent well CF_{warm} mid-day, when solar flux (and therefore radiative forcing) is at a maximum.

390

An additional question is whether the COT_{warm} values from the 10:30+13:30 MODIS-ACAERO retrievals are representative of the daytime average. The SEVIRI-LaRC retrievals don't simultaneously provide aerosol optical depth and cloud products, and inferred COT_{warm} could be biased if there is a high-AOD layer above the clouds. To approximate the diurnal cycle in COT_{warm} an empirical fit to COT_{warm} versus CF_{warm} from the MODIS-ACAERO dataset from all three field campaign years

395 and comparison transects was used to approximate the difference between the 10:30+13:30 average COT_{warm} and the average of COT_{warm} across the full daytime. The resulting fit (**Figure S.3**) is

$$COT_{warm,fit} = 1.663 \times e^{1.982*CF_{warm}} \tag{1}$$

COT_{warm}, like CF_{warm}, is slightly lower –typically by less than 0.5 – for the 10:30+13:30 average than for the full daytime average, when calculated using the approximation in Eqn. [1] (**Table S.3**). At the northern end of the 2016 Meridional1 and

400 2017 Meridional2 transects the difference is closer to 1.0. For a solar zenith angle of 30°, a decrease in COT_{warm} from 10.0, which is typical of clouds in this region (see Section 4.4), to 9.0 reduces cloud albedo by only 0.02, from 0.46 to 0.44 (see Section 5). The influence on scene albedo, which is the variable of interest for DARE, will be even smaller any time CF_{warm} is less than 1.0. As such, the COT_{warm} values from MODIS appear to represent very well the daytime average, within the context of their role in determining aerosol direct radiative effects.

405 **3.3 Modeled aerosol and cloud fields**

Data for all three ORACLES years are available for the WRF-CAM5 and GEOS models; UM-UKCA and ALADIN provided comparison data for the 2016 and 2017 ORACLES field campaign periods only. Statistic for all variables listed in Section 2.1 are provided for the WRF-CAM5 model. Statistics are not provided for RH from GEOS; for CO from UM-UKCA; and for CO, RH and AAE for ALADIN.

410

All models report aerosol optical properties at ambient RH, in contrast to the observed optical properties which are at low RH. The UM-UKCA model also reports dry aerosol optical properties. In addition, all models report extinction and SSA at 550nm, whereas the observed values are at 530nm. Finally, the modeled AAE and SAE are calculated from 400 to 600nm, whereas the observed AAE is calculated using σ_{ap} at the three wavelengths of 470, 530 and 660nm, and the SAE using σ_{sp} at

415 450, 550 and 700nm.

The reported model CF_{warm} values are the mean of the gridbox 2D warm, low cloud fractions, i.e. the fraction of the gridbox covered by cloud as viewed from above, not the fraction of the 3D gridbox filled by cloud. Modeled CF_{warm} values exclude mid- and high-altitude clouds, and includes all low-lying warm clouds. This 2D CF is roughly equivalent to what would be

420 observed via satellite and is the relevant quantity when interested in short-wave radiative forcing. For all models, 3-D cloud fractions are converted to 2-D warm, low cloud fractions (CF_{warm}) by assuming maximum horizontal overlap in clouds at different altitudes within the same model column. As with the observed mean COT_{warm} values, the model mean COT_{warm} for each gridbox is the geometric-mean (Section 3.2) with one exception: for the ALADIN model, the geometric mean COT_{warm} statistic was not calculated, so the median COT_{warm} is used instead.

425

Details on each model are given in Section 9.2 of Shinozuka et al. (2020), with brief descriptions given here. WRF-CAM5 is the regional Weather Research & Forecasting model with chemistry (WRF-Chem) coupled with the Community Atmosphere Model v.5 (CAM5) physics (Ma et al., 2014) with updated aerosol activation parameterizations (Zhang et al., 2015a,b). Here, the model is run at 36 km horizontal resolution and with 74 vertical layers varying in resolution from 10 m to 500 m,

430 with higher resolution at lower altitudes. Aerosol mass and number are tracked, and aerosol optical properties calculated with Mie code assuming an internally mixed aerosol with three aerosol modes (Aitken, accumulation and coarse). Cloud formation is driven by the shallow convection scheme of Bretherton and Park (2009) and deep convection by the Zhang and McFarlane (1995) scheme, with interactive aerosols. Smoke emissions are initialized daily from the Quick Fire Emissions Data set version 2 (QFED2) (Darmenov and Da Silva, 2015) which provides emissions on a daily basis. Smoke is emitted

435 directly into the boundary layer without using any plume injection parameterization. The model is initialized every five days using the NCEP Final Operational Global Analysis (FNL) and CAMS reanalysis and runs for 7 days, with the first two days of the run used for spin-up. Data are output at three-hour time resolution and aggregated for statistics.

The GEOS (Goddard Earth Observing System v. 5) global model (Molod et al., 2015; Rienecker et al., 2008), often

440 referenced as GEOS-FP (GEOS Forward Processing), is the forecast system of NASA's Global Modeling and Assimilation Office. It is run in near real time at approx. 25 km horizontal resolution (0.25° in latitude, 0.3125° in longitude) and 72 vertical layers (of which 25 layers are between the surface and 400 hPa). The model is initialized every 12 hours, with aerosol fields saved every three hours and cloud fields hourly. The model is initialized using the MERRA-2 reanalysis product, so it includes assimilation of observed aerosol optical depth (AOD) data. This 'nudging' towards observed AOD

445 should improve this model's simulated σ_{ep} values relative to a free-running model. Like WRF-CAM5, GEOS also uses QFED2 biomass burning emissions and injects the emissions at the surface. It prognostically predicts CO, aerosol component masses and ambient-RH aerosol optical properties using GOCART (Goddard Chemistry Aerosol Radiation and Transport; Chin et al., 2002; Colarco et al., 2010). It assumes that aerosols are externally mixed in modes of fixed mean diameter and standard deviation. Optical properties are computed for each aerosol species included in GOCART and as a

450 function of RH (Randles et al., 2017; Colarco et al., 2014). GEOS assimilates AOD observations from remote sensing every three hours (Albayrak et al., 2013). Organic aerosol (OA) concentration is not provided explicitly by GEOS, but organic carbon (OC) is. The ratio OA/OC=1.4 is used to obtain the reported OA concentrations. Both hydrophilic and hydrophobic

BC and OC are simulated; masses reported here are from the sum of the hydrophilic and hydrophobic components. Clouds are simulated by the convective parameterization.

455

The Unified Model coupled to the United Kingdom Chemistry and Aerosol model (UM-UKCA) is a global model that forecasts aerosols and clouds and is run here with a configuration modified from that used in Gordon et al. (2018), which also focused on the SE Atlantic. The model resolution varies with latitude (N216 resolution), with approximately 60 x 90 km resolution at the equator. It has 70 vertical levels between the surface and 80 km altitude, with a decreasing vertical
460 resolution such that the grid spacing at 1.5 km altitude is approximately 200 m. It is nudged to horizontal wind fields (not to temperature) from ERA-interim reanalyses, with nudging starting at 1700 m above the surface and ramping up to its full strength at 2150 m altitude. The reanalysis files are read in every six hours, which is also the relaxation time for the nudging. The model is run continuously forward from the initialization used by Gordon et al. (2018). In contrast to WRF-CAM5 and GEOS, biomass burning emissions are updated daily using the FEER inventory (Ichoku and Ellison, 2014). Smoke aerosol is
465 emitted into and distributed through the boundary layer, such that concentrations are highest at the surface, then taper down to zero at 3 km above the surface (Gordon et al., 2018). The emitted smoke has an initial log-normal size distribution with a mode centered on 120 nm diameter. Sea-salt emissions are based on winds, no dust emissions are included, and all other emissions are from the CMIP5 inventories. Aerosols in the model are represented in five size modes of internally-mixed aerosol. Both dry and ambient-RH aerosol properties are tracked, with hygroscopicity based on Petters and Kreidenweis
470 (2007). Convection is represented using the pc2 sub-grid cloud scheme of Wilson et al. (2008) or is parametrized where it cannot be resolved.

The ALADIN model is a regional climate model developed at Météo-France/CNRM. The v.6 version used here has a more detailed treatment specifically of biomass burning aerosols than previous versions (Mallet et al., 2019, 2020). The model has
475 12 km horizontal resolution and 91 vertical levels with 28 located between the surface and 6 km altitude. Lateral boundary conditions and the initial state for the modeled region come from the ERA-Interim reanalysis (Dee et al. 2011). The model includes TACTIC (Tropospheric Aerosol Scheme for Climate In CNRM; Nabat et al. 2020) which includes sea salt, desert dust, sulfates, black and organic carbon separated in 12 aerosol size bins. All emissions come from the CMIP6 emissions inventory (van Marle et al. 2017), which uses the GFED database for biomass burning emissions. This inventory has realistic
480 biomass burning emissions only through 2014, so these runs were done using constant year 2014 emissions. Further, while the BC emissions from GFED are used, ALADIN uses a fixed particulate organic matter (POM) to organic carbon (OC) ratio based on Formenti et al. (2003), so secondary organic aerosol formation is not accounted for. The radiative properties of liquid clouds are calculated in the shortwave using the Slingo and Schrecker (1982) parametrizations. The atmospheric physics has recently been revisited, as described in detail in Roehrig et al. (2020). For the model runs used here, the first
485 indirect effect was not simulated, and cloud droplet effective radius was held fixed at 10μm.

4 Results

The representativeness of the sampled aerosol properties to that of the entire field campaign period within each deployment year are discussed in Section 4.1. Biases in modeled extensive properties (CO, BC, and OA concentrations and σ_{ep}) are then discussed in Section 4.2, in aerosol intensive properties (SSA, SAE, and AAE) in Section 4.3, and in clouds (CF$_{warm}$ and COT$_{warm}$) in Section 4.4.

4.1 Representativeness of observations

As discussed above, a goal of flying along the Routine track was to acquire data representative of the observation period rather than, e.g., targeting high-concentrations plumes. With limited flight hours, and in-situ sampling from the P-3 at specific altitudes on each flight track, the number of minutes spent in many of the gridboxes and altitude bins was on the order of 1-2 hours in total over the approximately month-long campaign in each year; for some gridboxes and altitudes it was <20 min (**Figure 2**). The amount of data collected is particularly limited at the far reach of the comparison transects, i.e. the northwestern-most and northern-most gridboxes in the 2016 Diagonal and Meridional1 transects, and the southern-most gridboxes in the 2017 and 2018 Meridonal2 transect. For the Zonal transect, in-situ sampling was extremely limited, with significant sampling only in 2017 in the western-most Zonal gridboxes 1 and 2 (from the "suitcase" flights to Ascension Island; Redemann et al., 2020) and in gridbox 11, which intersects with the Meridional2 Routine track.

Figures 3 and **4** shows the ratios of the average of σ_{ep} in the model for those times when the aircraft was present for sampling (in-situ for the P-3 and of the full column below the aircraft for the HSRL-2 on the ER-2 aircraft; i.e. "sampled") to the daytime average for the full duration of the field deployment that year ("climatology"). Shinozuka et al. (2020) tested the representativeness of the observed column properties to the full month of the 2016 campaign period using as a metric the mean bias (MB) and the root mean squared deviation (RMSD) of CO and aerosol properties, along with their ratio (%) to the monthly mean. They calculated MB and RMSD across gridboxes for data within broad altitude ranges, including for 3-6km. Here we test for representativeness through ratio of the means in 1km deep altitude bins for each gridbox (colored dots in **Figures 3** and **4**). This metric is the same as MB(%)/100+1. This selection was made because the RMSD gives greater weight to individual large deviations, and the focus of this paper is on the average bias in observed values, which will most directly scale with a mean bias in DARE. In addition to calculating the mean bias for each gridbox, the transect-mean bias is calculated across all gridboxes in a given comparison transect and altitude bin (open circles in **Figures 3** and **4**).

Both WRF-CAM5 and GEOS indicate that σ_{ep} at plume altitudes (2-5 km) along the 2016 Diagonal transect is, on average, somewhat higher during the times sampled by the P-3 than it is for the monthly average (**Figure 3a,b**), consistent with the findings of Shinozuka et al. (2020) in their AOD comparisons. The transect-mean ratio is up to a factor of 1.5 depending on the altitude and model, with WRF-CAM5 showing larger and less variable differences than GEOS. Values of σ_{ep} at the times

17

measured by the HSRL-2 from the ER-2 better represented the month-long average (**Figure 3c,d**), with mostly moderate differences (ratios of 0.8-1.2) according to GEOS. In WRF-CAM5, the ratio of sampled σ_{ep} to the monthly-long "climatology" increases with altitude from 2 km to 6 km, indicating that the sampled plume may have been centered at higher altitudes than was typical for that month.

The 2016 Meridional1 transect is not a Routine flight track, so sampling was on flights targeting the smoke plume and/or specific cloud fields and includes fewer observations than the Diagonal transect (**Figure 2**). As such, it was not expected to be as representative of the monthly average. Despite this, in the heart of the plume (2-4km altitude), sampled values of σ_{ep} were generally with 0.9-1.2 of the month-long climatology in the both models (**Figure 3e,f**). Both models also indicate that smoke concentrations sampled by the P-3 at higher altitudes (4-6km) are much higher than was typical. Values of σ_{ep} from times when the HSRL-2 could make observations from the ER-2 are more consistently representative of the month-long average, with transect-mean ratios in most altitude bins above 2 km between 0.8 and 1.2 (**Figure 3g,h**). As for the 2016 Diagonal transect, the WRF-CAM5 simulations indicate the sampled plumes were centered at a higher altitude than is typical for this month.

The two models give very different results regarding the representativeness of both the in-situ and HSRL-2 values of σ_{ep} to the month-long climatologies along the Meridional2 transect in both 2017 and 2018. The WRF-CAM5 model indicates that σ_{ep} in the 2-6km altitude range for both in-situ and HSRL-2 sampling was generally 0.8-1.2 times that of the month-long climatology, and was almost always within a factor of 2 for individual gridboxes in the 2-5km altitude range (**Figure 4a,c,e,g**). GEOS simulations, however, show significantly higher values of σ_{ep} in the P-3 sampling average than in the month-long climatology for almost all gridboxes and altitudes. It also shows much greater variability across the different gridboxes in the sampling bias. As noted in Section 2.2 σ_{ep} in GEOS had a higher relative variability than observed along the 2017 Meridional2 transect, whereas WRF-CAM5 had similar variability to that observed and therefore may present a better test of the representativeness of the observations.

Overall, the values of HSRL-2 σ_{ep} sampled by the HSRL-2 are more representative of the climatology than the in-situ values, likely because there simply were more samples gathered by the HSRL-2. Typically, the HSRL-2 retrievals are available in full "curtains" from just below the aircraft flight level to either the surface or cloud top from the south-bound. In 2016, the HSRL-2 was on the ER-2, which always flew fully above the plume, so it captured the full vertical extent of the plume. In 2017 and 2018, when it was on board the P-3, the HSRL-2 generally could capture most of the plume vertical extent during the out-bound leg of Routine flights along the Meridional2 transect, since they were flown at high altitude. A combination of in-situ measurements and HSRL-2 measurements would then be collected on the return, north-bound leg, which was flown at a variety of altitudes. As such, there are more data from the HSRL-2 than from the in-situ measurements to contribute to comparison statistics.
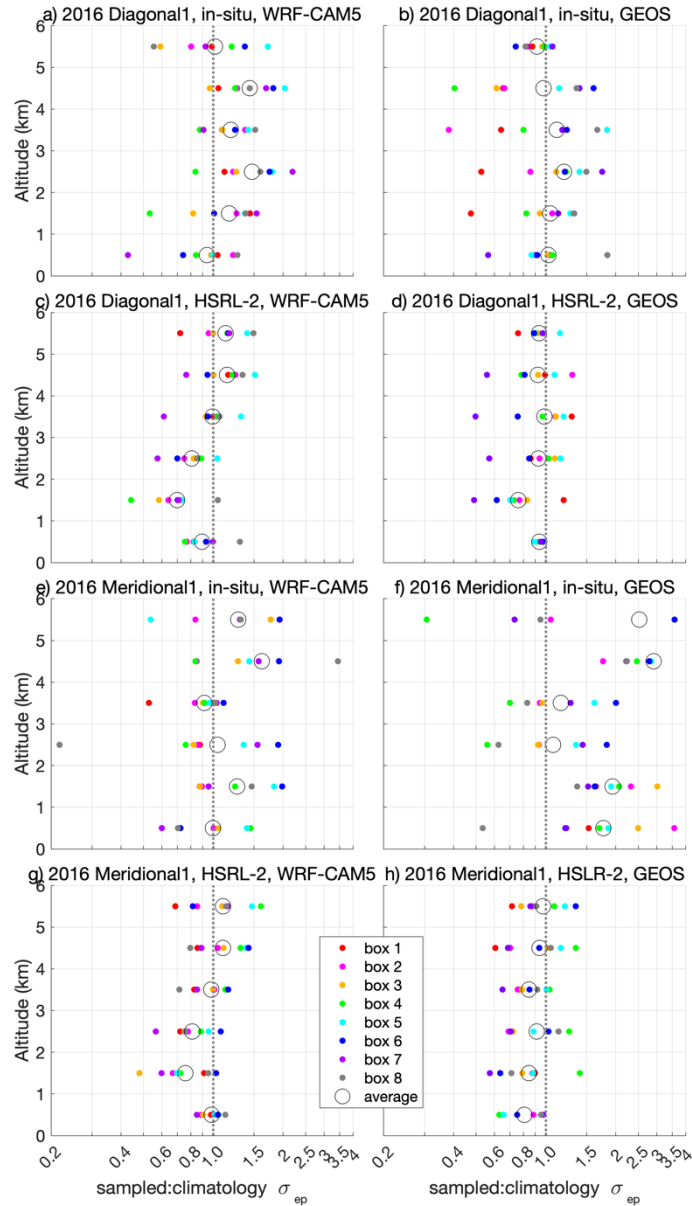
Figure 3. The ratio in mean of σ_{ep} modeled by WRF-CAM5 (left column) and GEOS (right column) for only those times when observed values are available ("sampled") to the mean of σ_{ep} across the entire field campaign time period ("climatology") in the (a-d) Diagonal transect in Sept. 2016 and (e-h) Meridional1 transect in Sept. 2016. The representativeness of both the in-situ (a, b & e, f) and HSRL-2 (c, d & g, h) observations of σ_{ep} are shown. The color dots show the means within individual comparison gridboxes; open circles are the mean across all gridboxes in that transect. Note that in panel f) there is a single gridbox datapoint that is off-scale (sampled:climatology σ_{ep} >4).

19
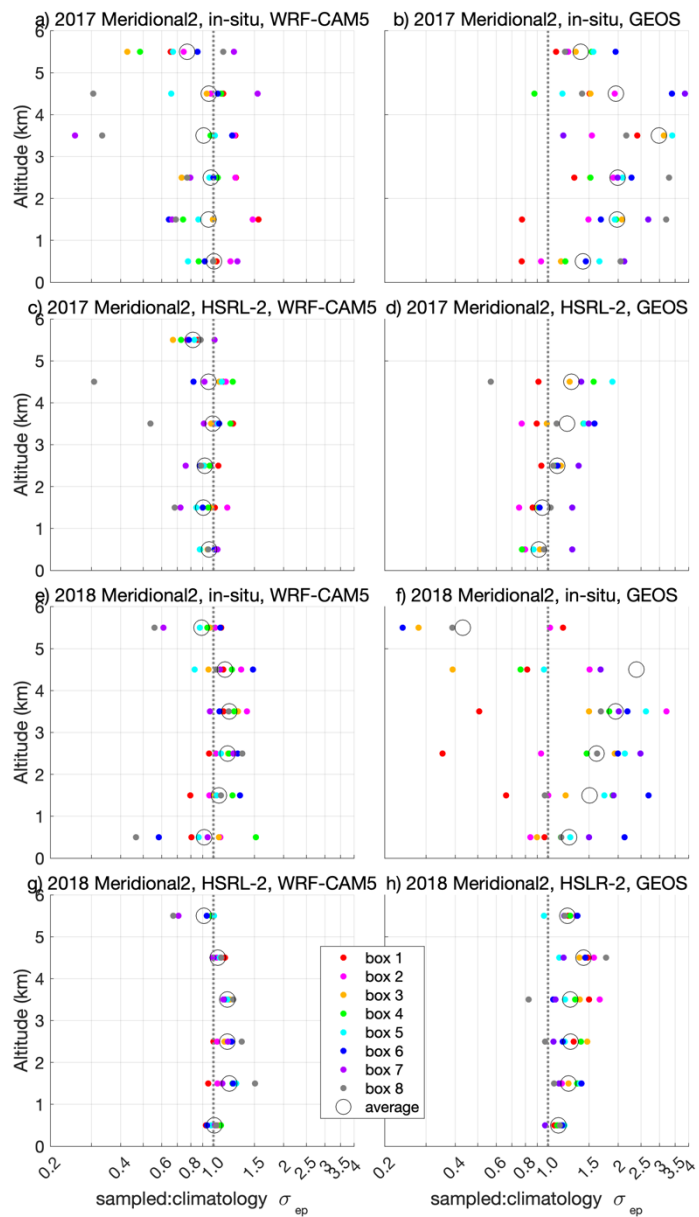
Figure 4. As in Figure 3, but showing the representativeness of sampled σ_{ep} values to the month-long average of σ_{ep} across
565 the 2017 Meridional2 and 2018 Meridional2 transects.
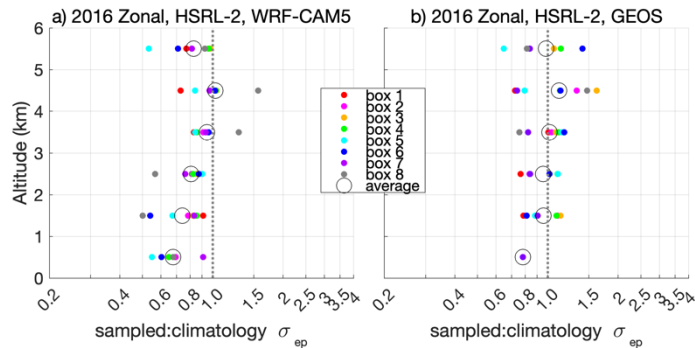
Figure 5. As in Figure 3, but for the 2016 Zonal transect, and for the HSRL-2 retrievals of σ_{ep} only.

570

In 2016, the ER-2 flew along the Zonal transect on several flights (**Figure 1**). WRF-CAM5 and GEOS both simulate average σ_{ep} from HSRL-2 sampling times that are on average within 0.8-1.2 of the month-long average in the 2-5 km altitude range (**Figure 5**). This ratio is both more positive and more variable across gridboxes for 4-5km than for 2-4km or 5-6km. This likely reflects the sampling coincidence with individual elevated plumes during the ER-2 flights.

575

In 2017, σ_{ep} from both the in-situ and HSRL-2 sampling times poorly represent the August average for most gridboxes and altitudes (**Figure S.4**), and in 2018 the P-3 did not fly along the Zonal transect. For this reason, comparisons are not made of modeled and measured aerosols along the Zonal transect. Clouds (CF$_{warm}$ and COT$_{warm}$) were measured by satellite on all field campaign days, so comparisons of these fields along the Zonal transect are included for all three years.

580

Tests of the representativeness of σ_{ep} measured from the aircraft addresses sampling biases in the concentration of the aerosol. In the context of DARE calculations, an additional question is whether the optical properties of the sampled aerosol are representative. Aerosol SSA in particular is a strong controlling factor for the sign and magnitude of DARE. In the WRF-CAM5 model SSA of the aerosol in the 2-6 km altitude range at the times when there are in-situ measurements from the P-3
585 are generally within 0.01 of the month-long average for that campaign year (not shown). SSA deviations from the average were a bit larger in the GEOS model in some gridboxes at these altitudes. In particular, in the Meridional2 transect the aerosol measured in the two southern-most gridboxes in 2017 has an anomalously low SSA (by about 0.03-0.04) and in 2018 the SSA for 4-5km is similarly anomalously high. These two gridboxes were the most under-sampled in the Meridional2 transect, since they were the farthest from the deployment base. As will be seen below the observed SSA varied more than
590 the WRF-CAM5 modeled SSA, but less than the GEOS modeled SSA, so the apparent representativeness of the sampled aerosol SSA may be a reflection of an inherent invariance in SSA in the models rather than an indication of the actual representativeness of the sampled aerosol optical properties.

21

4.2 Biases in plume extensive properties

Biomass burning smoke from the African continent is advected over the SE Atlantic largely in the free troposphere, and this is reflected in the observed profiles of σ_{ep} across the comparison transects (**Figures 6-9**). This continental airmass carries with it water vapor (Pistone et al., 2021), though RH in the plume is still generally less than 60% in September 2016 and August 2017 and less than 70% in October 2018, except in the two northern-most gridboxes of the Meridional2 transect in 2018 (**Figures 10** and **11**). The impact of humidification on σ_{ep} and on this comparison is discussed in Section 4.2.3.

Analogous figures showing profiles of the other extensive variables can be found in Supplemental **Figures S.5** (CO), **S.6** (BC), and **S.7** (OA). In the sections below, the modeled-to-observed ratios of these parameters are discussed; these should be viewed in the context of the smoke plume distribution (**Figures 6-9**) since large biases in the core of the smoke plume have much greater impact than large biases where concentrations are low.

4.2.1 Carbon Monoxide (CO)

Carbon monoxide does not lead to climate forcing, but it is an excellent and relatively inert tracer of biomass burning emissions and so is discussed here. WRF-CAM5 modeled CO at plume altitudes (2-5 km) is typically around 70% to 80% of that observed, with a slightly greater low bias in 2018 (**Table 1** and **Figure S.5**). GEOS also has a low bias in CO at plume altitudes, but the biases are somewhat smaller and were more variable than for WRF-CAM5. In 2016 and 2017 the GEOS CO concentrations are increasingly biased low going from 2 km to 5 km altitude. In 2018, the GEOS biases are more consistent (0.6-0.8; **Table 1**) across almost all altitudes and gridboxes. The GEOS modeled plume extends to lower altitudes than observed (**Figure S.5**), so that for the 1-2 km altitude bin the overall low bias in modeled CO is effectively offset by the contribution of the lower part of the modeled plume. Near the surface (0-1 km), CO in both WRF-CAM5 and GEOS is biased low. CO was not reported for the UM-UKCA and ALADIN models.   The biases in WRF-CAM5 and GEOS suggest under-estimates in CO emissions or possibly in the efficiency of transport of the biomass burning plume over the SE Atlantic from the burning source regions, since CO is not affected by scavenging processes. An earlier evaluation by Das et al. (2017) of GEOS simulations of the SE Atlantic biomass burning plume compared to CALIOP lidar profiles indicated that, for that model, transport biases are the more likely explanation.
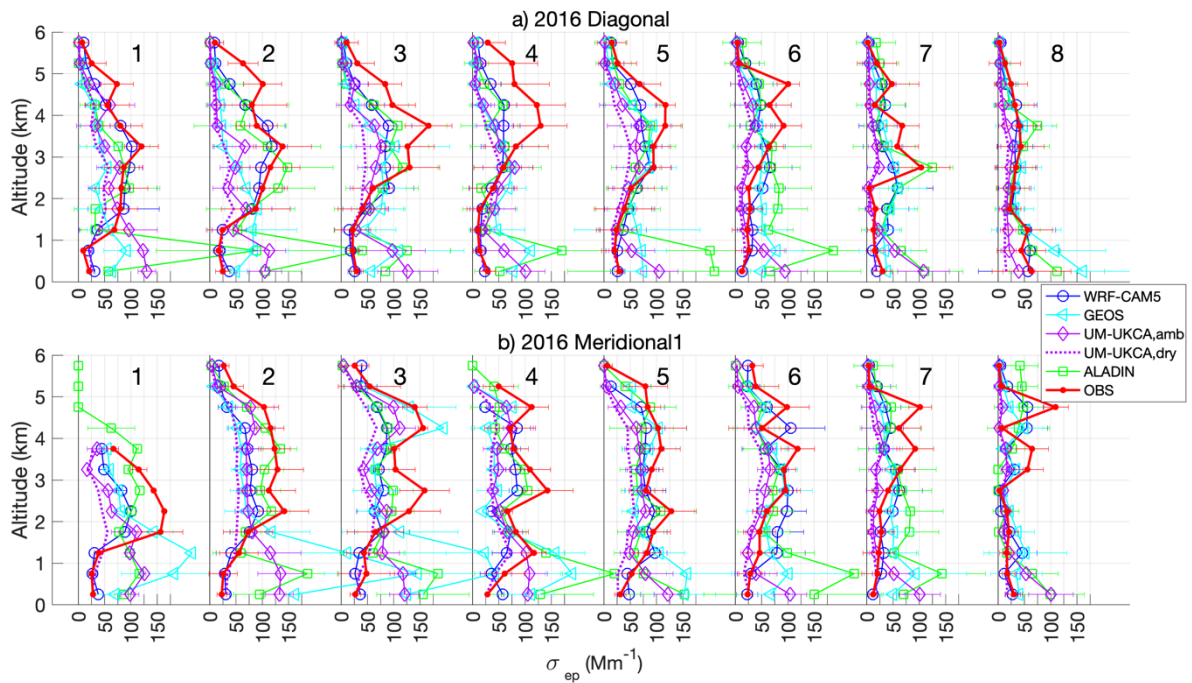
Figure 6. Profiles of σ_{ep} as observed in-situ from the P-3 aircraft (low-RH; 530nm) and modeled (ambient-RH and, for UM-UKCA only, dry; 550nm) for a) the 2016 Diagonal transect and b) 2016 Meridional1 transect. All values are means and standard deviations calculated across only those times and locations when in-situ measurements were made. Gridboxes are numbered as in Figure 1.
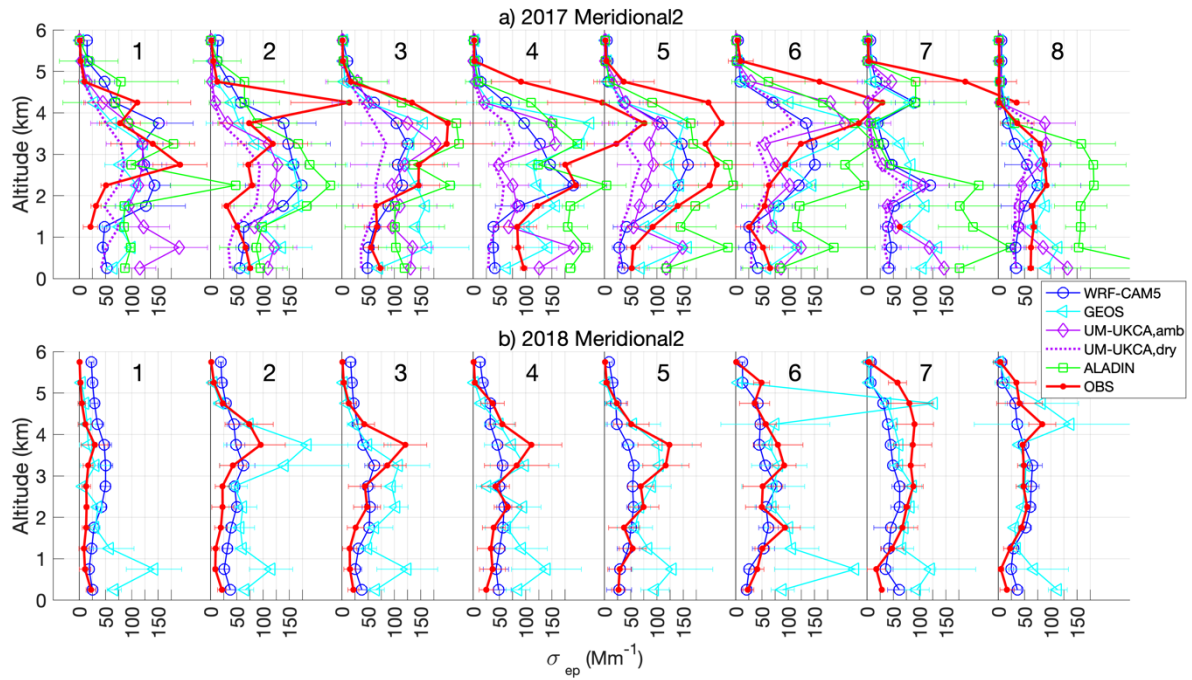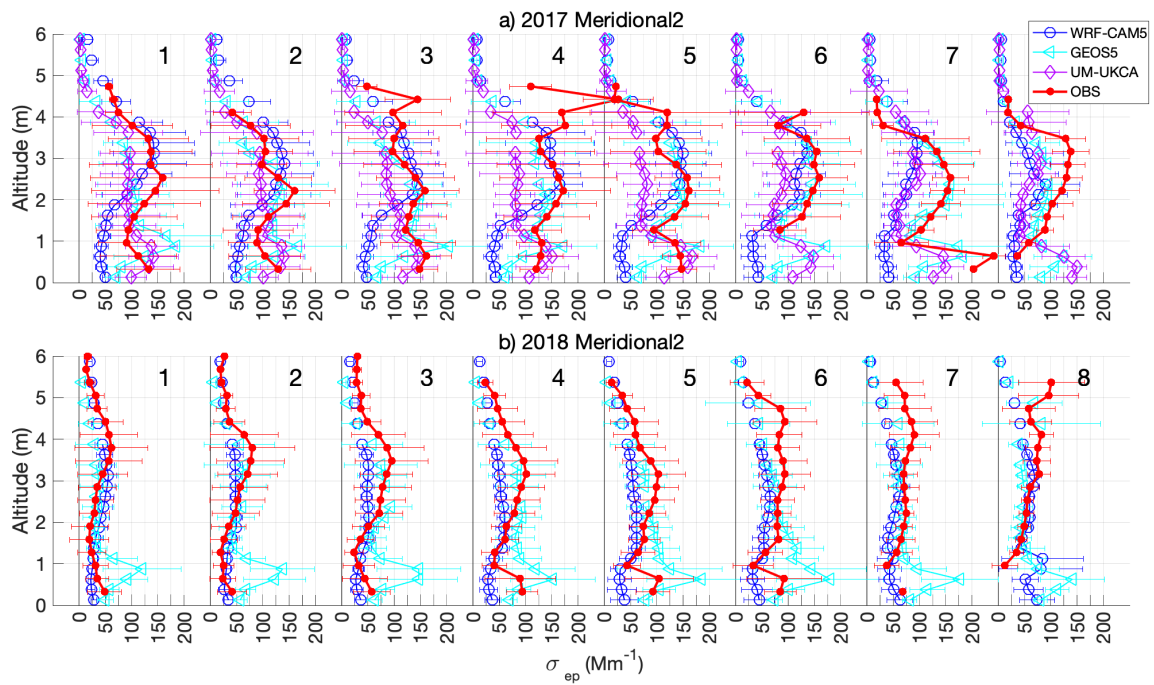

Figure 7. As in Figure 4, but for a) 2017 and b) 2018 Meridional2 transect.
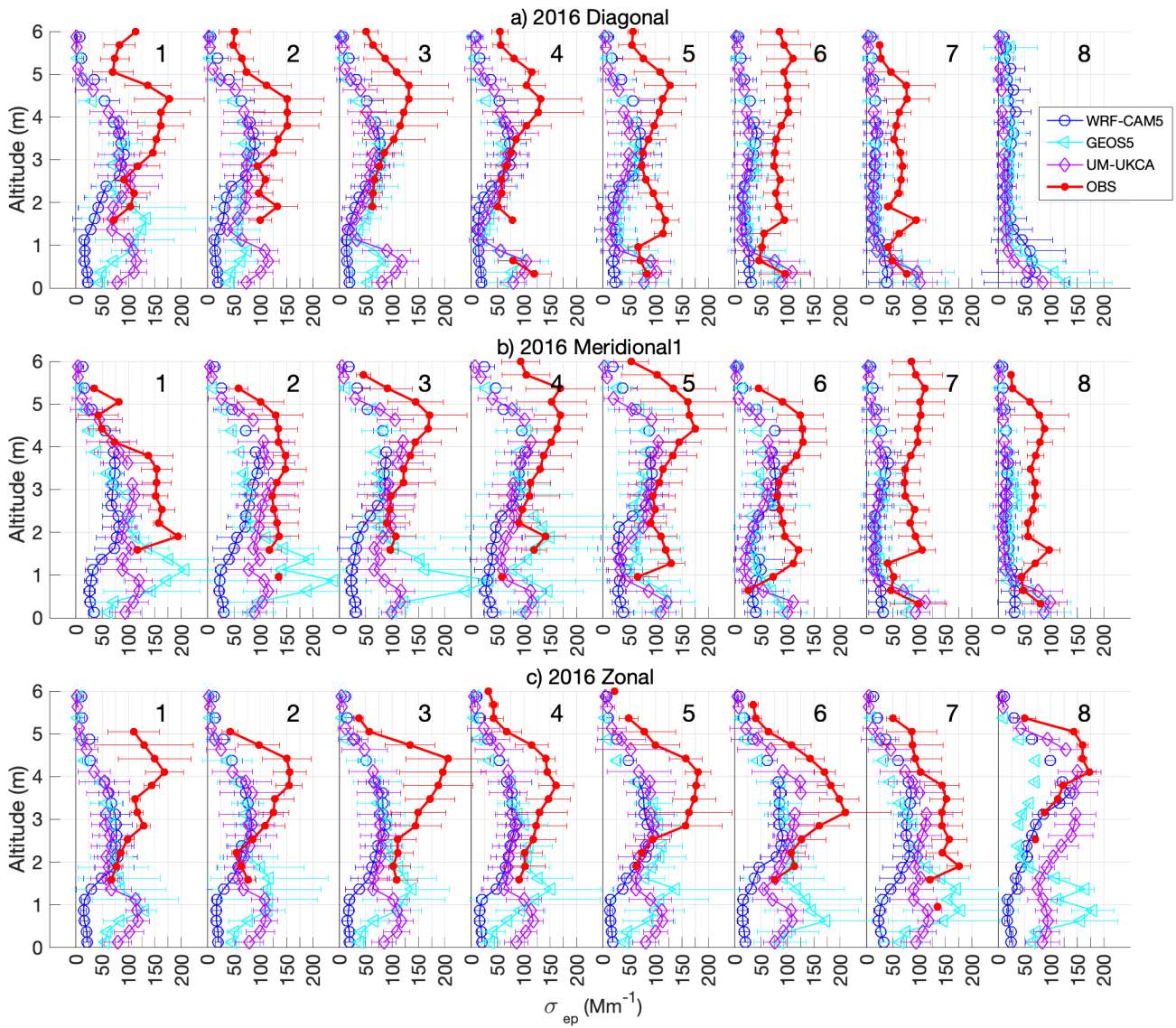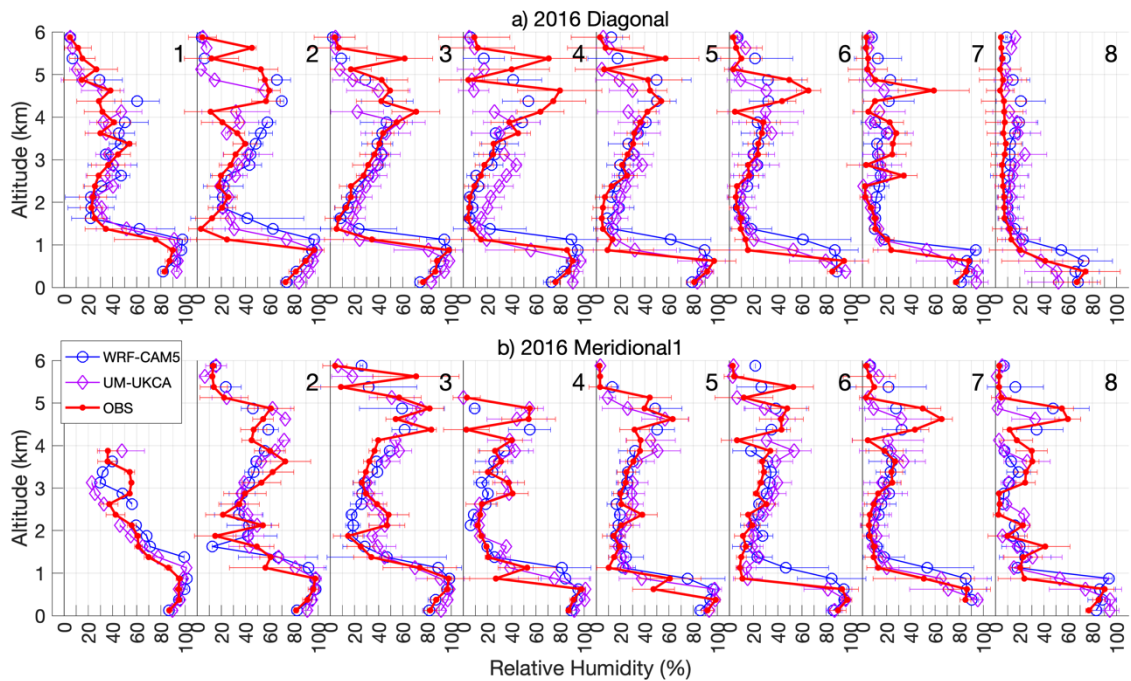
Figure 8. As in Figure 6, but for HSRL-2 retrievals of σ_{ep} from the ER2 aircraft in 2016. Here, all values are at ambient RH.
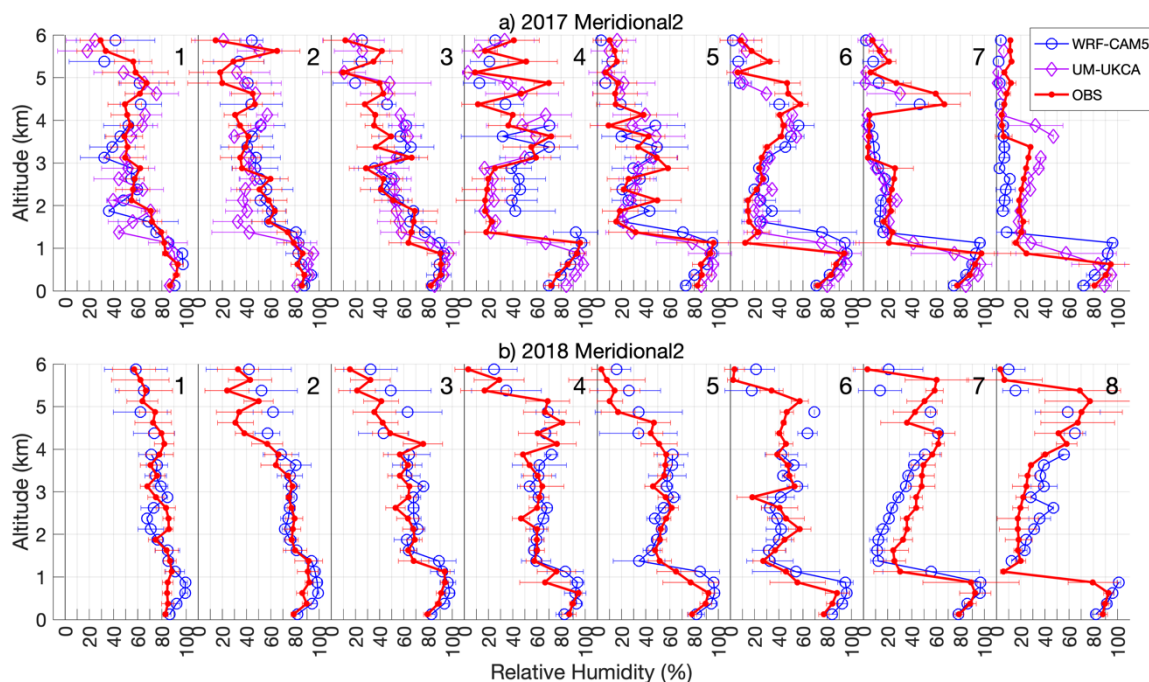
Figure 9. As in Figure 8, but for HSRL-2 retrievals of of σ_{ep} from the P-3 aircraft along the a) 2017 and b) 2018 Meridional2 transect.

635

Figure 10. As in Figure 6, but for RH, and at 250m vertical resolution rather than 500m vertical resolution.

Figure 11. As in Figure 10, but for RH along the a) 2017 and b) 2018 Meridional2 transect.

640

4.2.2 Aerosol BC and OA masses

During ORACLES, the aerosol components BC and OA were measured in-situ and were reported for the WRF-CAM5, GEOS and UM-UKCA models. In addition to emissions and transport processes, accurate simulation of aerosol concentrations requires simulating loss processes, including dry and wet deposition and any in-atmosphere production or

645 loss. During the biomass burning season (July-October), south of ~2-3S latitude in the SE Atlantic there are few clouds with tops above 2km, with small drop sizes further discouraging the wet scavenging of aerosols from the free troposphere (Adebiyi et al., 2020). For the 2016 Diagonal comparison gridboxes, and for all but the northern-most two to three Meridional2 gridboxes in 2017 and 2018 almost all wet scavenging occurs in moist convection over the central African continent (Ryoo et al., 2021). Once over the ocean, wet deposition likely plays essentially no role in driving aerosol

650 gradients in latitude and longitude above the marine boundary layer across our comparison transects, except possibly in Meridional2 gridboxes 1-3 (located between 0.5N and 5.5S). Fall speeds for accumulation mode aerosols are at most a few meters per week; given the biomass burning smoke is largely advected over the ocean at altitudes >2 km, dry scavenging rates also will be negligible. The vertical position of the plume and how it changes with transport is therefore dominated by overall atmospheric convection and subsidence.

Table 1. Median across each comparison transect of modeled-to-observed ratios for extensive parameters averaged within 1 km deep altitude bins. Shown are median biases for CO concentrations, BC mass, OA mass and σ_{ep} as measured in-situ from the P-3 aircraft. Observed values of σ_{ep} are at 530nm and for low-RH (<40%) aerosol, whereas modeled values are at 550nm and ambient RH, except for UM-UKCA which reports σ_{ep} for both the dry and ambient-RH aerosol.

| | WRF-CAM5 | | | | GEOS | | | | UM-UKCA | | | ALADIN | | |
	2016 Diag	2016 Mer1	2017 Mer2	2018 Mer2	2016 Diag	2016 Mer1	2017 Mer2	2018 Mer2	2016 Diag	2016 Mer1	2017 Mer2	2016 Diag	2016 Mer1	2017 Mer2
Carbon Monoxide (CO)														
5-6km	0.60	0.80	0.72	0.74	0.76	0.80	1.00	0.82						
4-5km	0.70	0.82	0.60	0.69	0.65	0.87	0.73	0.76						
3-4km	0.74	0.72	0.87	0.65	0.72	0.91	0.89	0.66						
2-3km	0.81	0.72	0.72	0.68	1.05	0.90	0.89	0.77						
1-2km	0.76	0.68	0.68	0.68	1.01	1.02	1.12	0.77						
0-1km	0.83	0.70	0.80	0.83	0.85	0.93	0.73	0.85						
Black Carbon (BC) mass														
5-6km	1.09	5.01	3.30	12.59	1.21	2.15	4.16	1.84	0.59	1.78	1.75			
4-5km	0.84	1.21	0.47	1.20	0.50	1.28	0.50	1.40	0.39	0.78	0.48			
3-4km	0.82	0.84	0.83	0.79	0.85	0.93	1.11	1.25	0.55	0.87	0.77			
2-3km	1.04	0.90	0.97	1.28	1.79	0.90	1.11	1.81	0.86	0.70	0.72			
1-2km	0.89	0.79	0.95	0.90	2.60	2.57	2.22	1.87	1.05	0.91	1.23			
0-1km	1.68	0.88	1.17	1.03	3.48	3.09	1.06	4.82	1.77	1.08	0.68			
Organic Aerosol (OA) mass														
5-6km	0.71	2.50	10.08	14.56	0.81	2.37	7.02	2.80	0.37	0.73	2.27			
4-5km	0.71	1.25	2.28	1.58	0.60	1.82	3.59	2.86	0.51	0.99	1.32			
3-4km	0.84	0.77	1.24	1.36	1.37	1.33	2.69	3.39	0.68	0.82	1.17			
2-3km	1.09	0.89	1.23	2.61	3.31	1.58	2.28	6.49	0.98	0.87	0.89			
1-2km	0.96	0.89	0.92	4.46	4.48	4.38	3.05	14.63	1.46	1.47	1.20			
0-1km	1.35	0.79	2.02	6.40	6.71	7.29	1.92	45.33	2.00	1.94	0.81			

| | Aerosol light extinction (σ_{ep}) | | | | | | | | | | | | | | | | |
									dry	amb	*dry*	amb	*dry*	amb			
5-6km	0.88	0.89	3.30	7.12	0.29	0.68	1.71	0.80	*0.09*	0.12	*0.18*	0.24	*0.57*	0.73	0.34	0.35	0.76
4-5km	0.64	0.70	0.49	0.83	0.32	0.69	0.28	0.87	*0.18*	0.27	*0.37*	0.57	*0.24*	0.41	0.52	0.65	0.90
3-4km	0.70	0.66	0.63	0.57	0.57	0.57	0.72	0.89	*0.31*	0.44	*0.40*	0.54	*0.40*	0.69	0.70	0.74	1.24
2-3km	1.08	0.77	0.90	1.16	1.11	0.59	0.92	1.25	*0.52*	0.69	*0.43*	0.56	*0.54*	0.73	1.09	0.80	2.00
1-2km	1.13	1.01	0.92	1.34	2.03	2.24	1.64	1.89	*0.72*	1.14	*0.69*	0.85	*0.74*	1.23	1.41	1.17	2.80
0-1km	1.10	1.18	0.59	1.63	3.46	4.16	1.62	5.34	*0.97*	4.22	*0.89*	3.34	*0.51*	1.81	6.81	4.66	2.32

BC and OA are the primary constituents of biomass burning aerosol, so their distribution is a direct measure of the smoke plume intensity and location. On average, the observed core of the plume is centered at higher altitudes moving towards the edges of the plume (i.e. the south end of the Meridional1 transect and southeast end of the Diagonal transect in 2016, and the north end of the Meridional2 transect in 2017 and 2018) and it covers a broader vertical extent towards the geographic center of the plume (**Figures 6-9, S.6** and **S.7**). In 2016 in particular this tendency is not captured by any of the models, which have a vertically broader plume across all gridboxes and, in the case of GEOS and UM-UKCA especially, place the plume core at too low an altitude, though the plume top height is nonetheless captured properly in some cases (Shinozuka et al., 2020).

This overly vertically diffuse plume in WRF-CAM5 is consistent with underestimates in BC concentrations in the core of the plume (3-4 km altitude in 2016 and 2018; 3.5-5km in 2017) (**Figures 12** and **13**), over-estimates above this, and smaller biases for the 2-3km altitude bin. The pattern of bias is similar for GEOS, except that it does a better job of reproducing BC concentrations aloft at the southern end of the 2016 Meridional1 transect (**Figure 12**) and has greater high biases at the bottom of the plume (2-3km altitude bin). UM-UKCA BC in the 2016 Diagonal transect in the 3-5km altitude range is about half that measured; in the 2016 Meridional1 and 2017 Meridional2 transects biases in modelled BC are smaller, generally 0.70-0.85 at plume altitudes (**Figures 12** and **13** and **Table 1**). In 2016, as with GEOS, the fact that the plume is too low in altitude results in large negative biases at the highest altitude, but a low bias below this that decreases from 5 km to 2 km altitude. Both GEOS and UM-UKCA over-estimate the amount of BC (i.e. biomass smoke) that mixes into the marine boundary layer, with consequences for derived forcing through aerosol-cloud interactions.

In several of the transects, above 5 km the observed BC and OA concentrations effectively go to zero (**Figures S.6** and **S.7**), whereas for all models aerosol concentrations taper off more slowly, possibly due to coarse vertical resolution at these heights (e.g., WRF-CAM5 resolution is ~500 m at 6 km). This produces very high modeled-to-observed ratios for the 5-6 km
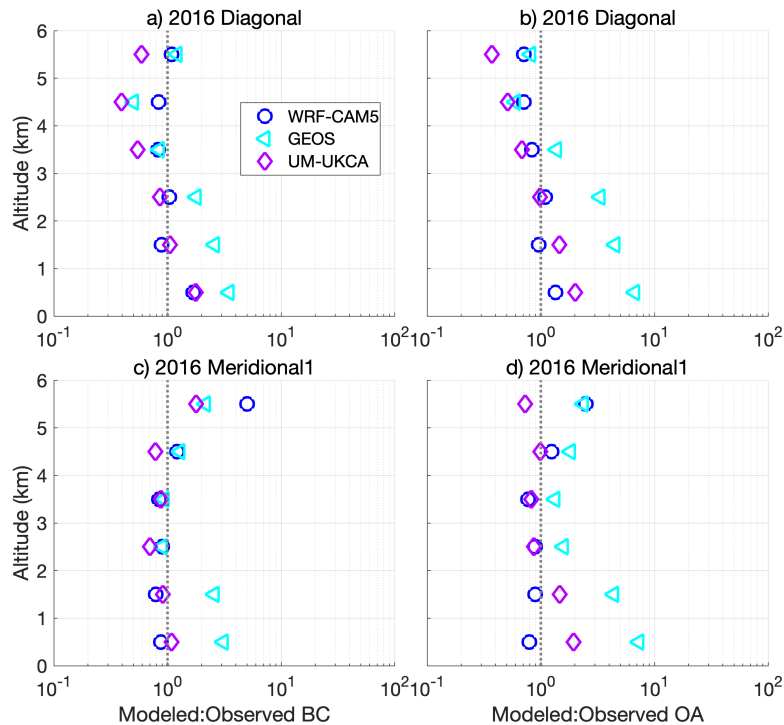
Figure 12. Mean ratio of modeled to observed BC mass (panels a, c) and OA mass (panels b, d) across all eight gridboxes along the 2016 Diagonal (a, b) and Meridional1 (c, d) comparison transects. The ratios for individual gridboxes, along with these means, can be seen in Supplemental Figure S.8 (for WRF-CAM5), Figures S.10 (for GEOS) and Figures S.12 (for UM-UKCA) .

altitude bin. However, this bias will have little effect on column aerosol mass, and therefore aerosol forcing, because concentrations are so low. More consequential is the high bias in modeled BC and OA in the 2-3 km altitude bin. This high bias is particular pronounced for GEOS for the 2016 comparison transects. The tendency of GEOS to place aerosol too low in altitude can also be seen in the large high bias in boundary layer (~0-2 km) BC and OA concentrations (**Figures 12** and **13**), as reported for the 2016 campaign by Shinozuka et al. (2016); as in UM-UKCA, this would lead to an overestimate in modeled forcing through aerosol-cloud interactions.

The marine environment can be a source of OA, but is only a small component of accumulation mode aerosol in the sub-tropics (Heald et al., 2008; Shank et al., 2012; Twohey et al., 2013), and in the models included here the ocean is not a source of OA. Additionally, there is no marine source for BC. Thus, the high bias in OA and BC concentrations below 2km in the UM-UKCA and GEOS simulations is a clear indication the model is mixing too much biomass burning smoke into the boundary layer, and therefore into low marine clouds.
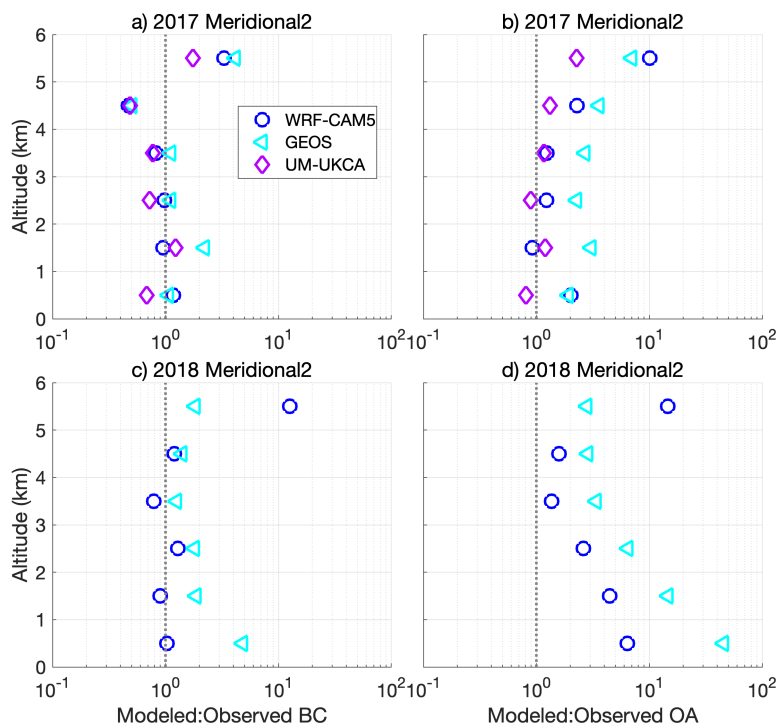
Figure 13. As in Figure 12, but for the 2017 and 2018 Meridional2 comparison transect. The ratios for individual gridboxes, along with these means, are given in Supplemental Figure S.9 (for WRF-CAM5), Figures S.11 (for GEOS) and Figures S.13 (for UM-UKCA) .

4.2.3 Light extinction

The comparison between modeled and observed σ_{ep} is complicated by the fact that σ_{ep} from the in-situ measurements is at low RH (typically <40%), whereas the models report σ_{ep} at ambient RH. An exception is the UM-UKCA model, which provides both dry and ambient-RH σ_{ep}. The disparity between low-RH and ambient-RH σ_{ep} is expected to be large in the boundary layer, where RH is generally above 75-80%. Sea salt can be a significant component of boundary-layer aerosol and, in addition to being very hygroscopic (Tang et al., 1997; Niedermeier et al., 2008), much of it is in the aerosol coarse mode, which would have been under-sampled by the P-3 aircraft aerosol inlet. Given these issues, the fact that the smoke resides largely above the boundary layer (e.g., Das et al., 2017), and that the focus of this analysis is on comparisons relevant to the direct aerosol radiative effect by biomass burning aerosol, our discussion will focus on the comparison of σ_{ep} at altitudes above 2km.

The effect of humidification on the biomass burning aerosol light scattering is estimated using in-situ measurements of low (<40%) and high (~85%) RH 530 nm light scattering made on the P-3 aircraft in 2016 and 2018. Instrumental problems in

30

725 2017 preclude estimates for that year. The growth of light scattering is parameterized by fitting an exponential function to the measured low- and high-RH values of σ_{sp} versus the RH of the measurements, using the exponent gamma (γ) as the metric for hygroscopicity (e.g.,Kasten, 1969; Burgos et al., 2019). Using all data within a given campaign year, γ in the plume averages 0.62±0.05 in 2016 and 0.68±0.05 in 2018. This is quite a bit higher than γ for biomass burning smoke from previous measurements (e.g., Kotchenruther and Hobbs, 1998; Titos et al., 2016). Evaluating the hygroscopicity

730 measurements is beyond the scope of this paper, but the estimates presented here should be viewed with this in mind. The derived values of γ are used directly to calculate the approximate scale factor, f(RH), to convert the low-RH measured values of σ_{sp} to ambient RH σ_{sp}. Values of f(RH) are calculated for the mean±1-sigma observed ambient RH in each comparison transect gridbox within 250m resolution altitude bins from 2km to 6km (**Figure S.14**). For 2017, the value of γ from 2018 (0.68) is used in this calculation since the comparisons in these two years both cover the same Meridional2 transect.

735

Shinozuka et al., (2020) estimated that, for September 2016, f(RH) was less than 1.2 for 90% of the free troposphere aerosol measurements across the campaign. Estimates for the comparison gridboxes included here are consistent with this (**Figure S.14**), but also show that f(RH) for the 2016 Diagonal gridboxes 3-6 in the 4-5.5 km altitude range were often higher, with means of 1.30±0.14, 1.46±0.19, 1.30±0.10 and 1.26±0.21 for gridboxes 3, 4, 5 and 6, respectively. Gridboxes farther north in

740 the 2016 Meridional1 transect also were more humid, with f(RH) for gridboxes 1, 2 and 3 of 1.36±0.14, 1.39±0.14 and 1.44±0.51, respectively, in the 2-5km altitude range. If γ is actually lower than derived here – e.g., closer to a value of ~0.3, as measured in the year 2000 SAFARI campaign in southwest Africa (Titos et al., 2016) – the f(RH) values applied here would be about 30% too large (~1.5 vs. ~1.2 for γ of 0.65 vs. 0.3, for an ambient RH of 60%).

745 In both 2016 and 2017 RH at plume altitudes was generally <60% (**Figures 10** and **11**). In 2017, RH in the plume tended to decrease from north (gridbox 1) to south (gridbox 8) across the Meridional2 transect. The humidification factor f(RH) is accordingly estimated to decrease from typical values of 1.3-1.5 towards the north end of the transect to 1.0-1.2 at the south end (**Figure S.14**). In 2017, f(RH) is again slightly higher at 4-5 km altitude, and the humidity and f(RH) more variable than in the lower part of the plume. This is consistent with the fact that mid-level clouds were intermittently observed within and

750 upwind of this transect.

In Oct. 2018, the RH in the plume was greater than in Sept. 2016 or Aug. 2017 (**Figure 11** vs. **Figure 10**), because convection was shifted further south and was carried over the SE Atlantic by the southern African easterly jet (Ryoo et al., 2021). It was still generally 60% or lower in Meridional2 gridboxes 6-8, with f(RH) usually <1.3. North of this, in gridboxes

755 3-5, RH at 2-4km was closer to 60% so f(RH) is more typically 1.3-1.5. In gridboxes 1 and 2 RH was closer to 80% in the free troposphere. For these gridboxes, f(RH) was almost always greater than 1.5 and could exceed a factor of 2 (**Figure S.14**).

This analysis estimates the effect of humidification on light scattering only, not on light absorption. Since scattering

760 dominates extinction, f(RH) for σ_{sp} nonetheless provides a good estimate of the impact of humidification on σ_{ep}. Based on this analysis, the in-situ, low-RH values of σ_{ep} are expected to typically be 20-50% lower than the modeled and HSRL-2 measured ambient-RH values of σ_{ep}, all else being equal. Instead, the modeled values of ambient-RH σ_{ep} in the plume are generally lower than both the dry in-situ values and the ambient-RH HSRL-2 values.

765 **4.2.3.1 WRF-CAM5**

As for OA and BC, the observed σ_{ep} profiles are at higher altitude and less vertically diffuse than in the models (**Figures 6-9**). This produces a similar pattern to the biases in BC, OA and σ_{ep}. In the in-situ measurements in particular σ_{ep} increases more rapidly with altitude at the bottom of the plume and decreases more rapidly with altitude at the top of the plume than does the WRF-CAM5 modeled extinction. This is most pronounced in the gridboxes with higher-concentration and/or, more

770 well-defined plumes (e.g., **Figure 6a**). In addition, the observed plume is centered at a higher altitude than in the models. This leads to under-estimates in modeled σ_{ep} in WRF-CAM5, relative to in-situ values, in the core of the plume (3-4 km altitude) of about 30-35% in 2016, 10% in 2017 and 15% in 2018 (**Table 1**; **Figures 14** and **15**). Below and above the core of the plume (the 2-3 km and 4-5 km bins), the modeled-to-in-situ-observed ratio in σ_{ep} is closer to 1.0. In 2017 and 2018, WRF-CAM5 modeled extinction at 5-6km is more than 4 times (2017) and 9 times (2018) greater than observed in-situ

775 (**Figure 15**), but this is because σ_{ep} is measured to be near zero above 5 km in most gridboxes.

Biases in the model when compared to σ_{ep} from HSRL-2 follow a similar but less consistent pattern (**Figures 14** and **15** and **Table 2**). Again, the measurements show a plume core that is centered at a higher altitude and is less vertically diffuse than in the models, especially in 2016 (**Figure 8**). The model mean low bias referenced to the HSRL-2 measurements is generally

780 greater than the mean low bias compared to in-situ observed σ_{ep} (compare **Tables 1** and **2**), consistent with the former being at ambient RH and the latter dry σ_{ep}. Except in the 2018 Meridional2 transect, WRF-CAM5 σ_{ep} is generally 30-40% lower than measured by HSRL-2 (**Table 2**).

Notable in comparing **Figures 6** and **8** is that in 2016, when the HSRL-2 was on board the ER2 and so had retrievals to

785 >6km altitude, the top of the plume extends to higher altitudes than covered by the in-situ measurements. In the latter, σ_{ep} drops to near zero above 6 km in most comparison gridboxes; in the HSRL-2 retrievals, σ_{ep} above 5.5 km is usually still >50Mm^{-1}. The in-situ and HSRL-2 measurements were not coincident, so this difference could simply reflect different sampling, but the consistency of this feature across multiple comparison transects makes this seem unlikely. Relative humidity often increased above about 4 km (**Figure 6**), with humidification often amplifying σ_{ep} by a factor of 1.5 or more

790 (**Figure S.14**). While this cannot fully account for the very large difference in σ_{ep} in the models versus that observed in-situ,

or all of the difference between the plume top behavior between the in-situ and HSRL-2 measurements, humidification differences could be contributing.

The net effect of these altitude-dependent biases in σ_{ep} is that WRF-CAM5 under-estimates plume AOD, with Shinozuka et al. (2020) calculating a low bias of 10-30% in AOD for the 2016 campaign. Here, the modeled ambient-RH σ_{ep} is typically 70-80% of the in-situ measured dry σ_{ep} (with considerable variability). Accounting for the difference in humidity of the in-situ measurements (i.e. scaling in-situ σ_{ep} by 1.2-1.5) would make the WRF-CAM5 σ_{ep} in the plume to only about 50-70% of the observed average. This is not far from the observed ratios of WRF-CAM5 to HSRL-2 observed ambient-RH σ_{ep} (**Table 2**).
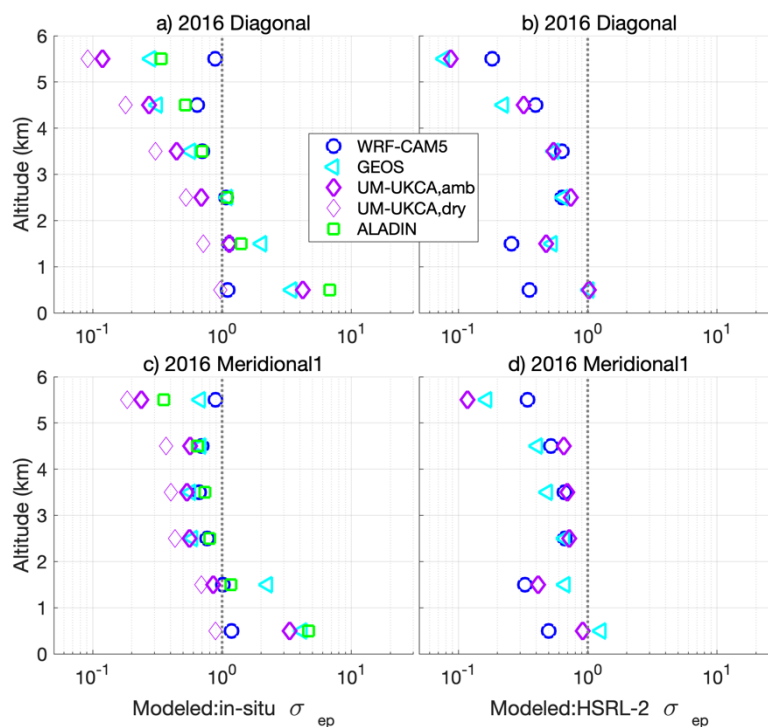
Figure 14. Mean ratio of modeled to in-situ low-RH (a, c) and HSRL-2 ambient-RH (b, d) mid-visible σ_{ep} across all gridboxes for the 2016 Diagonal (a, b) and Meridional1 (c, d) comparison transects. Comparisons to both dry and ambient-RH σ_{ep} are shown for the UM-UKCA model; for all other models, the comparison is to ambient-RH σ_{ep}. The ratios for individual gridboxes, along with these means, are given in Supplemental Figures S.15 (WRF-CAM5), S.17 (GEOS), S.19 (UM-UKCA) and S.21 (ALADIN).
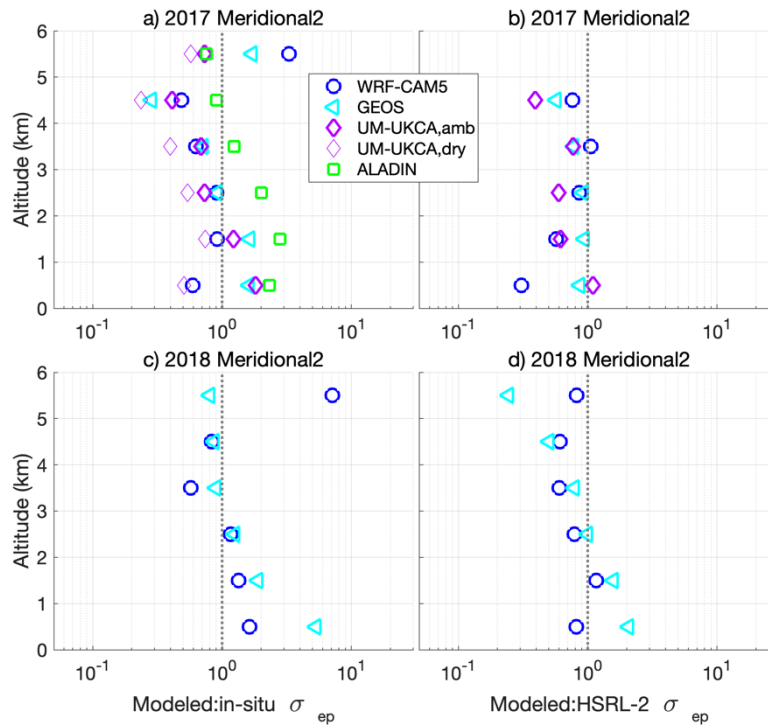
Figure 15. As in Figure 14, but for the (a, b) 2017 and (c, d) 2018 Meridional2 comparison transects. The ratios for individual gridboxes, along with these means, are given in Supplemental Figures S.16 (WRF-CAM5), S.18 (GEOS), S.20 (UM-UKCA) and S.21 (ALADIN).

Table 2. As in Table 1, but for retrieved values of σ_{ep} only from the HSRL-2 lidar on board the ER-2 aircraft in 2016 and the P-3 aircraft in 2017 and 2018. Both modeled and observed values are at ambient RH. The modeled values are 550nm and the HSRL-2 values are at 532nm.

	WRF-CAM5					GEOS					UM-UKCA			
	2016 Diag	2016 Mer1	2016 Zon	2017 Mer2	2018 Mer2	2016 Diag	2016 Mer1	2016 Zon	2017 Mer2	2018 Mer2	2016 Diag	2016 Mer1	2016 Zon	2017 Mer2
Aerosol light extinction (σ_{ep})														
5-6km	0.18	0.34	0.41	--	0.82	0.08	0.17	0.17	--	0.24	0.09	0.12	0.21	--
4-5km	0.40	0.52	0.34	0.76	0.61	0.22	0.41	0.25	0.57	0.50	0.32	0.65	0.45	0.39
3-4km	0.63	0.66	0.52	1.06	0.60	0.55	0.49	0.48	0.78	0.79	0.54	0.70	0.54	0.77
2-3km	0.64	0.66	0.71	0.86	0.79	0.65	0.67	0.79	0.93	1.00	0.74	0.72	0.76	0.60
1-2km	0.26	0.33	0.64	0.57	1.17	0.53	0.67	1.12	0.94	1.57	0.48	0.41	0.83	0.62
0-1km	0.35	0.50	0.19	0.31	0.82	1.03	1.27	1.33	0.87	2.07	1.02	0.92	0.85	1.10

34

4.2.3.2 GEOS

820 Biases in GEOS modeled σ_{ep} profiles have a strong vertical gradient in most comparison transects, with generally positive biases below about 2 km; above this the model has a low bias that becomes greater with altitude (**Figures 14** and **15** and **Table 1**). The low bias in GEOS σ_{ep} is smaller for August 2017 than for September 2016, and smaller again for October 2018. (**Tables 1** and **2**). In 2017 the bias also has a less consistent dependence on altitude (**Figure 15**). In 2018, the higher ambient RH (**Figure 11**) could be compensating for some of the low bias in dry aerosol σ_{ep}.

825

Overall, it is clear that GEOS underestimates σ_{ep} in the plume and centers the plume at too low an altitude (**Figures 6-9**), with a net impact of under-estimating the above-cloud AOD. This is consistent with the Shinozuka et al. finding of a greater low bias in AOD from GEOS (30-50%) than from WRF-CAM5 (10-30%). As for WRF-CAM5, accounting for humidification in the in-situ observations would increase the estimated bias in GEOS, to greater than a factor of two. This is

830 somewhat surprising, given that GEOS assimilates satellite-retrieved AOD every three hours (Albayrak et al., 2013).

4.2.3.3 ALADIN

Statistics from the ALADIN model are not available for comparison to the HSRL-2 retrieved σ_{ep}, so comparisons are made to in-situ σ_{ep} only. For both 2016 transects, ALADIN-modeled σ_{ep} is underestimated at the core of the plume and the

835 modeled plume is too vertically diffuse (**Figure 6**). Also apparent is that the model increasingly places the plume at too low an altitude (**Figures 14** and **15**), with the plume notably too low at the northwest end of the Diagonal1 transect (**Figure 6**), consistent with too much subsidence in the model with aerosol transport (Das et al., 2017). In the 2016 Diagonal transect this produces a low biases in modeled σ_{ep} that increases with altitude from 3km to 5 km, and high biases below 3 km (**Figure 14a**; **Table 1**), much as for the GEOS model.

840

In 2017, biases in ALADIN simulated σ_{ep} along the Meridional2 transect again have an altitude dependence indicating a plume that is displaced too low in altitude, but in this case producing high biases below 4 km altitude (**Figure 15a**). There is, in particular, a tendency for the model to over-estimate σ_{ep} at the north end of this transect and under-estimate it at the south end (**Figure S.21**), very possibly due to humidification amplifying σ_{ep} by about a factor of two for the northern gridboxes,

845 but only by a factor of ~1.1-1.4 at the southern end (**Figure S.14**).

Notably, the ALADIN simulations were run using fixed 2014 GFED emissions. Central and southern African biomass burning emissions in 2014 were not particularly different from the 2001-2013 climatological average (Kaiser and Van der Werf, 2015). While not a direct measure of emissions, AOD over the SE Atlantic was lower in both September 2016 and

850 August 2017 than the 2003-2018 average (Redemann et al., 2021), consistent with lower emissions in these months and

years than on average. If the ALADIN simulations had used the emissions for the observed months, modeled σ_{ep} may have been smaller, with greater low biases in 2016 and greater high biases (below 4km) in comparison to the observations.

4.2.3.4 UM-UKCA

855 For the UM-UKCA model, dry as well as ambient-RH σ_{ep} values were reported, allowing for a more robust comparison to the measured low-RH σ_{ep} and a rough comparison of observed versus modeled humidification factors. At all altitudes above 2 km, the model under-predicts dry aerosol σ_{ep} significantly across all comparison transects in 2016 and 2017 (**Figures 14 and 15** and **Table 1**). This low bias increases systematically with altitude from 2 km to 5 km. The gridbox-mean dry σ_{ep} is typically a factor of two to three lower in the model in the 3-4km and 4-5km altitude bins than observed in-situ. The altitude 860 dependence of the model biases again results from the modeled plume being too vertically diffuse, and the plume core too low in altitude.

Even with humidification added, the UM-UKCA modeled extinction is lower than the observed dry σ_{ep}, despite the fact that the model aerosol appears to be too hygroscopic. In 2016, modeled σ_{ep} in the 2-5km altitude range is a factor of 1.4 higher at 865 ambient RH than for the dry aerosol; for 2017 it's a factor of 1.5 higher. These humidification factors are somewhat higher than expected from our analysis from the in-situ observations, where f(RH) at these altitudes averaged 1.2 in both 2016 and 2017 (**Figure S.14**). The significant contribution of humidification to σ_{ep} also manifests in the fact that the modeled ambient-RH σ_{ep} is typically 0.55-0.75 that observed from the HSRL-2, and the simulated dry values of σ_{ep} are typically 0.2-0.5 that observed in-situ (**Figures 14** and **15** and **Tables 1** and **2**).

870

The UM-UKCA low biases in dry σ_{ep} are much greater than the model low biases in OA and BC, indicating that the model has a low bias in biomass burning aerosol mass extinction efficiency as well as mass. There could also be simply less total aerosol mass (e.g. of components other than OA and BC, such as sulfate) in the UM-UKCA model than in reality.

4.3 Biases in aerosol intensive optical properties

875 Model biases in aerosol constituent component masses (BC, OA) and σ_{ep} can arise from a combination of biases in the emissions, transport, deposition and (for OA) in-atmosphere production and loss from the aerosol phase of the biomass plume aerosol, which will clearly affect the magnitude of the calculated direct aerosol radiative effect. As noted earlier, the aerosol intensive optical properties, in particular the SSA, will also affect the sign of the aerosol DARE. The SAE connects the aerosol mass and extinction through the aerosol size, which is directly related to its aerosol mass scattering efficiency. 880 The SAE and AAE, combined with mid-visible σ_{ep}, give the wavelength-dependence of SSA (Russell et al., 2010).

4.3.1 Single scatter albedo (SSA)

Observed and modeled SSAs differ in two respects: in their absolute value and in their variation with altitude. In Sept. 2016 the observed SSA increases with altitude within the biomass burning plume along both the Diagonal and Meridonal1 transects (**Figure 16**), generally increasing from 0.82-0.84 at the bottom of the plume to 0.86-0.88 at the plume top. In August 2017 SSA spanned a similar range as in 2016 (**Figure 17**), but there is no significant gradient in SSA with altitude in the northern four Meridional2 gridboxes, and only a slight indication of an increase in SSA with altitude towards the southern half of the plume. There is also no vertical gradient in SSA in the northern-most three Meridional2 gridboxes in Oct. 2018, and SSA is overall higher than in September 2016 and August 2017. A vertical gradient is apparent in the southern five Meridional2 gridboxes in 2018, where SSA increases from 0.86-0.89 at plume bottom to 0.90-0.92 at plume top. Notably, gridboxes 4-7 are located well within the biomass plume, whereas the north end of this transect was often outside or on the edges of the plume. The vertical gradient in SSA has been associated with a gradient in aerosol composition (Redemann et al., 2021). Accounting for this gradient is important in determining the direct aerosol radiative effect because it is the extinction-weighted column SSA, combined with below-plume albedo, that dictates the sign of the direct forcing.

895
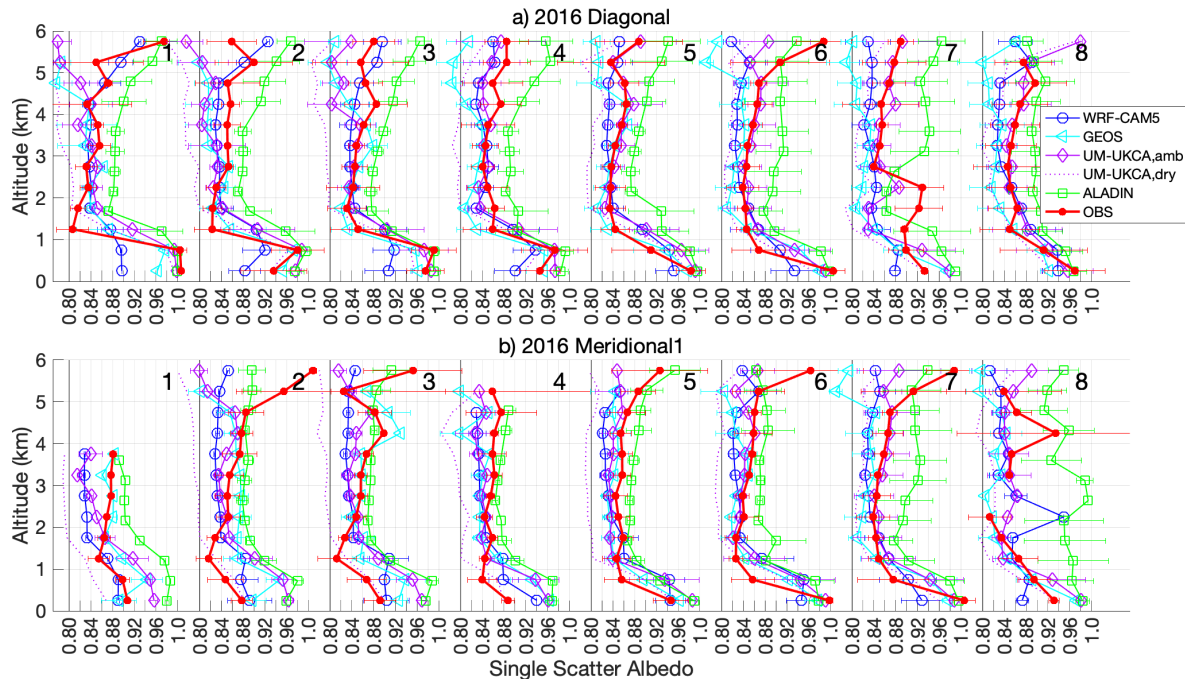
Figure 16. Profiles of SSA as observed (at low RH and 530nm) and modeled (at ambient RH and also, for UM-UKCA, dry, at 550nm) for the 2016 a) Diagonal and b) Meridional1 transects.
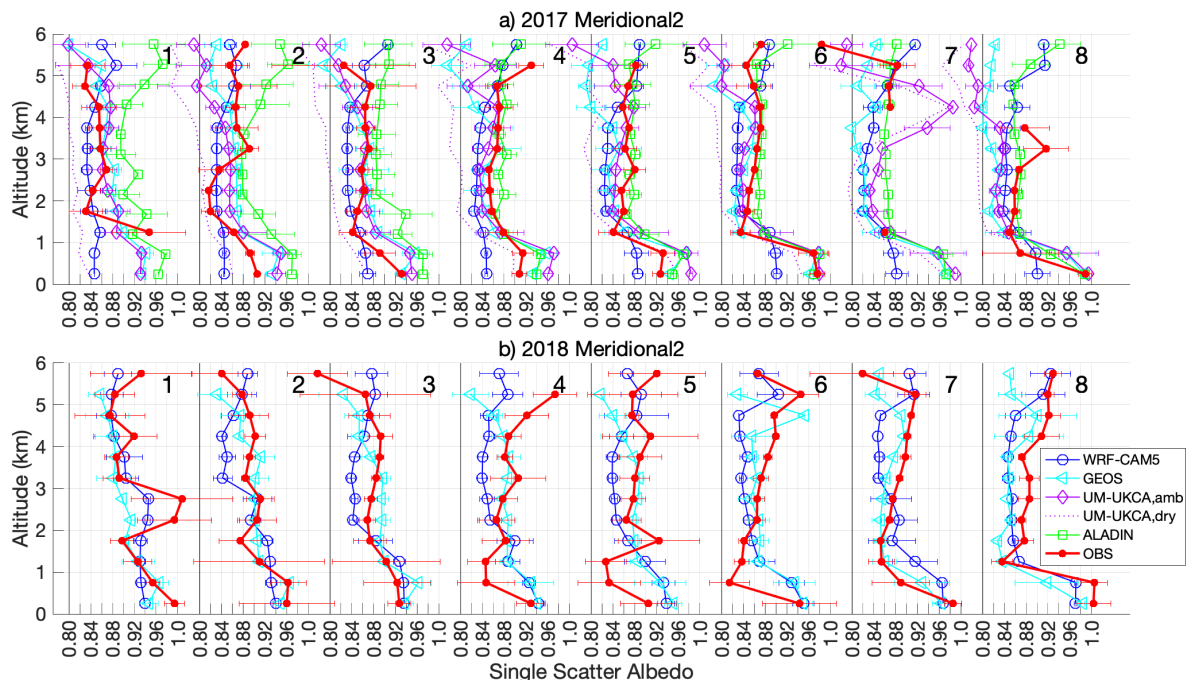
Figure 17. As in Figure 16, but for the a) 2017 and b) 2018 Meridional2 transects.

WRF-CAM5 produces little to no associated gradient in SSA with altitude (**Figures 16** and **17**), showing increases in SSA only at the very top of the plume in some comparison gridboxes. Within the plume, modeled SSA encompasses quite a small range, almost always being 0.82-0.84 in the Sept. 2016 transects and the Aug. 2017 transect (**Figure 15**). This difference in vertical gradient explains why Shinozuka et al. (2020) find greater low biases in the 3-6km altitude column SSA than in the lower free troposphere column SSA. As in the observations, in October 2018 the WRF-CAM5 SSA is slightly higher than in the other years, generally 0.84-0.86. WRF-CAM5 does not consider OA and BC aging and primary OA hygroscopicity is low (0.1), which is consistent with the small range in SSA.

GEOS similarly has little gradient in SSA with altitude within the plume, and where it does the tendency is for SSA to decrease with altitude, particularly towards the plume top. Here it diverges from the observed, increasing dry-aerosol SSA. Mean plume SSA values on average are similar in GEOS and WRF-CAM5, but SSA is about twice as variable in GEOS. This larger range in SSA doesn't show any apparent spatial pattern, other than somewhat higher SSA in the northern-most Meridional2 gridbox in both 2017 and 2018. This gridbox tended to be on the northern edge, or out of, the main biomass burning plume. Aging of OC in GEOS could be creating more hygroscopic aerosol with time, which in turn would increase the variability in ambient SSA through differences in water up-take.

In the UM-UKCA simulations SSA decreases significantly towards the top of the plume in some comparison gridboxes. In most cases this is true for both the dry and ambient-RH aerosol SSA, so this appears to be driven by a change in aerosol composition or size not by, e.g., a decrease in scattering due to a decrease in RH. The UM-UKCA ambient-RH SSA values are within 0.02 of the values measured in-situ at most altitudes in the plume (**Figure 14**), but the dry-aerosol SSA from UM-UKCA is significantly lower (typically 0.77-0.83) than both the modeled ambient-RH values (typically 0.84-0.88) and the dry in-situ values (**Figures 14** and **15**). This difference between the SSA of the dry and ambient-RH aerosol results from the significant increase in extinction with RH (Section 4.3.2).

ALADIN is the only model of the four where the SSA (which is at ambient RH) has a similar gradient with altitude in the plume to that observed. SSA in ALADIN includes a dependence on aerosol aging and RH (Mallet et al., 2019), and thus it is not clear if this altitude dependence in SSA is a response to higher RH towards the top of the plume or if it would still be present under dry conditions. ALADIN modeled SSA is also consistently higher than that observed.

The observed values of SSA are available only at low RH since σ_{ap} was measured only at low RH, and only the UM-UKCA model provided both dry and ambient-RH values of SSA. This makes it difficult to determine how much humidification differences are contributing to the differences between the observed and modelled SSA. The models include the effect of humidification on SSA by accounting for the impact of water on the aerosol indices of refraction (WRF-CAM5, GEOS, UM-UKCA) or by parameterizing the effect of RH on SSA (ALADIN; Mallet et al., 2017; 2019). In all four models, the result is an increase in SSA with humidification. In reality, it's likely that humidification affects both scattering and absorption. However, the former has been well-quantified observationally, whereas the latter has not and is therefore highly uncertain (e.g., Bond et al., 2013; Zhou et al., 2020).

The modeled ambient-RH SSA at plume altitudes is generally lower than the observed dry-aerosol SSA in both the WRF-CAM5 and GEOS models (**Figure 18**). Thus, the dry aerosol SSA in these models has even a greater low bias than indicated by **Figures 14-16**; whether it is as large as the low bias in the UM-UKCA dry SSA depends on the relative effects of humidity on scattering and absorption in the models. Humidity in the plume was somewhat higher in August, 2017, and, in particular, October 2018 than in September 2016 (**Figure 11** versus **Figure 10**), increasing modeled SSA and moving the modeled (ambient-RH) and observed (dry) SSA values in closer alignment on average. In contrast, for the two 2016 transects the ALADIN ambient-RH SSA is almost always higher than the observed dry SSA, with typical differences of 0.02-0.04. Adjustment of the ALADIN (ambient-RH) values to low RH (as in the observations) should bring the two into better agreement, though perhaps not for all transects: the differences are smaller in the 2017 Meridional2 transect, particularly towards the south, despite the higher ambient RH.
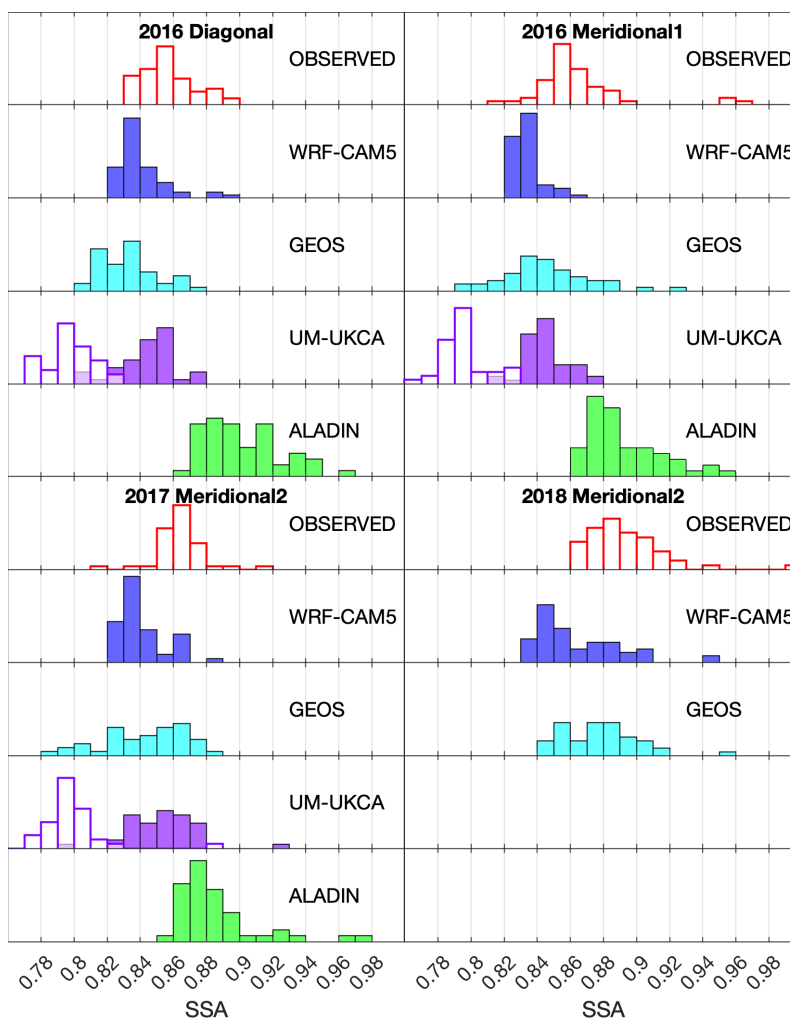
Figure 18. Histograms of SSA from the 2-5km altitude range only, as measured in-situ from the P-3 and as modeled using WRF-CAM5, GEOS-5, UM-UKCA and ALADIN for all samples along the comparison transects. For the UM-UKCA model, values are shown for both ambient-RH aerosol (filled bars) and dry aerosol (unfilled bars); the observed values are available only for the dry aerosol (unfilled bars).

Aerosol SSA is determined largely by aerosol composition, which for biomass burning aerosol is dominated by organic aerosol (e.g. see Figure 14 of Redemann et al., 2021). Black carbon is highly absorbing so the mass fraction of BC in particular drives SSA. As discussed below (Section 5.0), the relative biases in OA and BC indicate that the models have a higher OA:BC ratio than is observed. For given indices of refraction for these components, a higher OA:BC ratio would increase SSA in the models (since they don't include organic aerosol "brown" carbon absorption). Thus, the model OA:BC ratio does not explain the low bias in SSA in the WRF-CAM5 and GEOS models. Biases in model aerosol component indices of refraction, photochemical whitening (Carter et al., 2021), incorrect representation of the impacts of internal mixing

40

on indices of refraction, and the influence of aerosol components other than BC and OA could all be contributing to the
965 observed modeled biases in SSA.

An earlier study using data from the ORACLES 2016 field season compared SSA derived from the in-situ measurements used here and from three remote sensing instruments (Pistone et al., 2019): a spectral radiometer (SSFR) in combination with sun photometer derived AOD, a hyperspectral Sun photometer and sky radiometer (4STAR) in combination with SSFR
970 derived scene albedo, and an imaging polarimeter (AirMSPI). The SSFR and 4STAR instruments were deployed on the NASA P-3 aircraft along with the in-situ instruments; the AirMSPI instrument was mounted on the NASA ER-2 high-altitude aircraft, which overflew the P-3 at least once on coincident flight days (See Pistone et al, 2019 for more detail). The remote sensing instruments, like the models, all derive SSA at ambient RH. At 530nm, the average distribution of SSA from the in-situ instruments was higher than the 4STAR SSA by (on average) 0.01-0.02 (with 10-90 percentile ranges of 0.07 in
975 each), but was generally lower than the AirMSPI SSA, with differences of 0.03, with less variability overall (0.03 in 10-90 percentiles) compared with the P-3 instruments. The spread in differences was likely in part due to the full-campaign measurements not being coincident in either time or space, due to the varying measurement techniques. Direct comparison to the SSFR was made in one case study only, and for that case the SSFR 530nm SSA was <0.01 lower than the in-situ SSA (within the instrument uncertainty ranges). These results indicate it is unlikely that SSA from the in-situ instruments is
980 significantly biased high. It also supports the idea that humidification is not significantly influencing SSA over the SE Atlantic, since the in-situ values are at low RH and the remote sensing values are at ambient RH. They also imply that the impact of humidification on SSA in the UM-UKCA model (**Figure 18**) is too large (consistent with f(RH) being too large; Section 4.2.3.4), though it is difficult to make a robust conclusion based on this one observational comparison.

4.3.2 Scattering Ångström Exponent (SAE)

985 Whereas SSA varies primarily with aerosol composition, SAE varies primarily with aerosol size. For aerosol smaller than approximately 1000 nm dry diameter – i.e. as for aerosol in the SE Atlantic biomass burning plume (Shinozuka et al., 2020) – SAE gets smaller as aerosol size increases (Schuster et al., 2006). The observed SAE is quite consistently 1.7-1.9 within the plume, with very little vertical variation or difference across the two campaign years (2016 and 2017) where observations are available (**Figures 19** and **20**). WRF-CAM5 simulated SAE deviates the furthest from the observed values, with values
990 in the plume generally 0.9-1.3, consistent with the larger aerosol size in WRF-CAM5 than in reality (see Figure 4 in Shinozuka et al., 2020). GEOS and UM-UKCA both reproduce the observed SAE quite well, with the exception of a few gridboxes. The GEOS SAE values are typically 0.1-0.2 smaller than observed in the 2016 Meridional1 gridboxes 1-3, and above about 4 km at the north end of the 2017 Meridional2 transect. Both the dry and ambient-RH UM-UKCA values of SAE generally agree well with the observed SAE, consistent with the UM-UKCA aerosol being is only slightly larger than
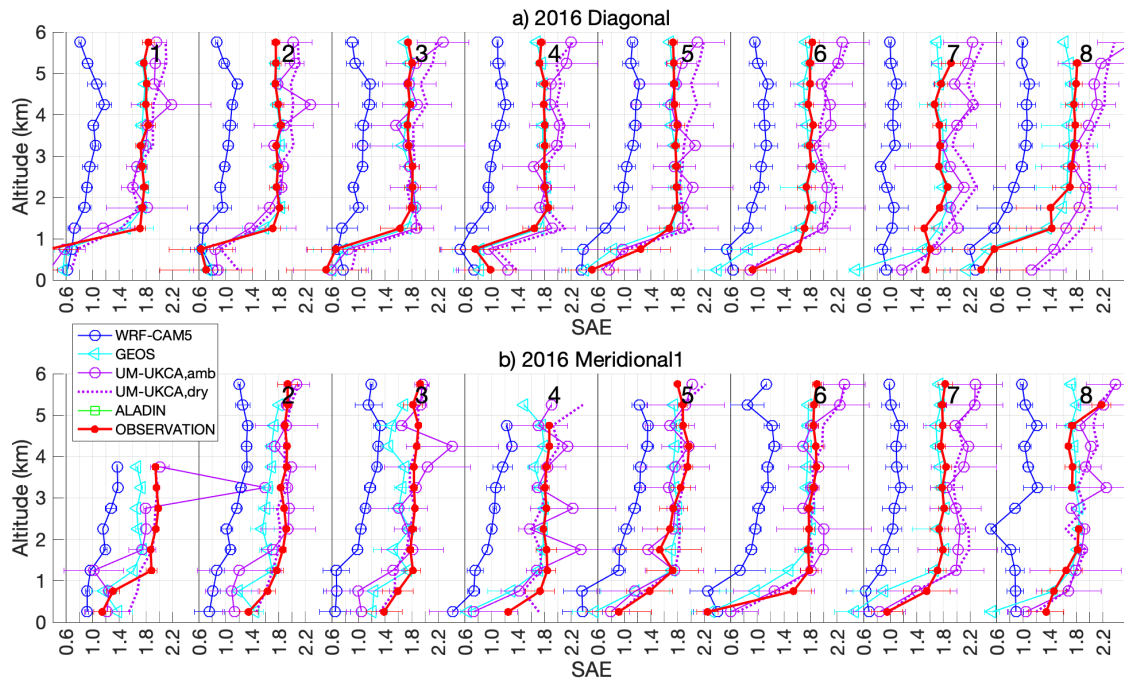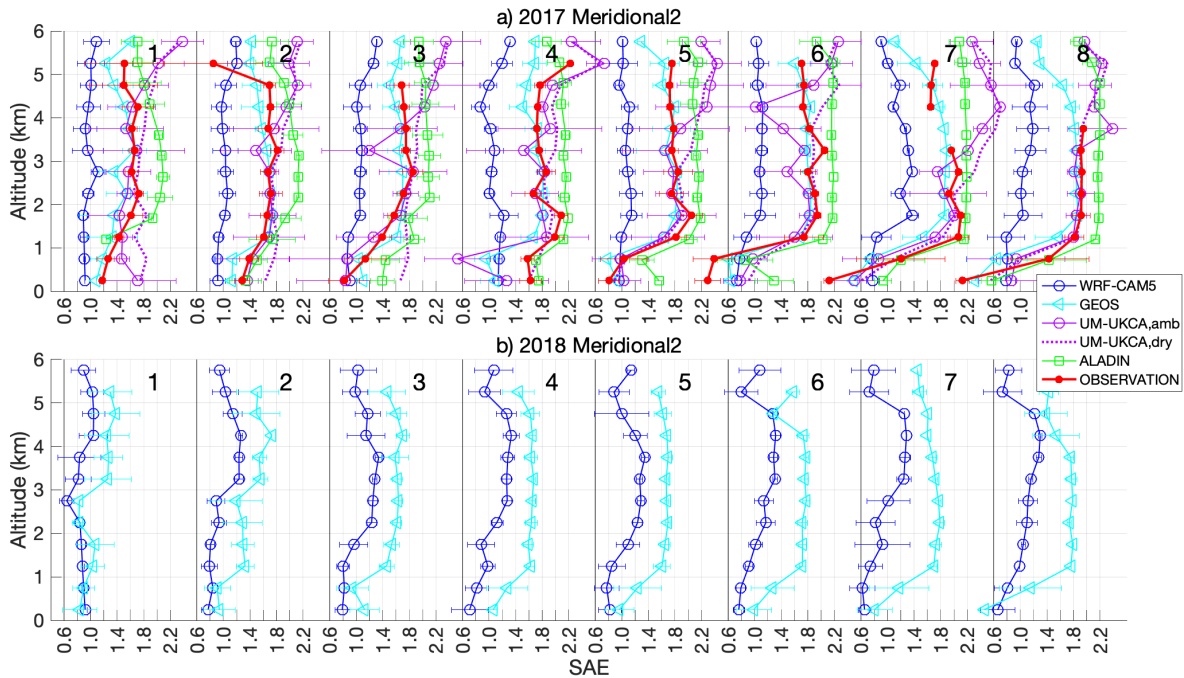995 observed.

Figure 19. As in Figure 16, but for the scattering Ångström exponent (SAE).

1000

Figure 20. As in Figure 17, but for the scattering Ångström exponent (SAE).

Both GEOS and UM-UKCA simulate vertical gradients – but of opposite sign – in SAE, and a gradient is not present in the observations. The ALADIN model also has a less-pronounced decrease in SAE towards the top of the plume and it simulates SAE values that are typically 0.02-0.04 higher than are observed in almost all gridboxes and plume altitudes. This is consistent with the aerosol in ALADIN being smaller than the observed aerosol, but the model uses a bulk-bin scheme so a mean aerosol size is not available for comparison. The GEOS and ALADIN models do include the effect of aging on aerosol hygroscopicity, possibly driving the modeled gradients in SAE.

The very small difference between the UM-UKCA simulated dry- and ambient-RH aerosol SAE values are surprising, given the large difference dry- and ambient-RH simulated σ_{ep} (Section 4.2.3.4) and SSA (**Figures 16-18**). The relative changes in σ_{ep} and SSA with humidification in this model are consistent with the change in SSA being driven by an increase in light scattering alone: e.g. an increase in σ_{sp} of a factor of 1.45 – which is the mean f(RH) for σ_{ep} in the UM-UKCA model in the 2016 transects (Section 4.2.3.4) – would produce a change in SSA from 0.80 to 0.85, which is consistent with the increase in SSA with humidification in the model (**Figure 18**). This implies significant aerosol growth with humidification, which should be reflected in the SAE. Resolving this apparent inconsistency would require work outside of the scope of this paper that considers more carefully the simulated size distribution and size-dependent composition of the aerosol.

4.3.3 Absorption Ångström Exponent (AAE)

As noted above, the in-situ PSAP measurements of σ_{ap} at 530, 460 and 660 nm are processed using two sets of correction factors, wavelength-averaged and wavelength-specific (Virkkula, 2010). The two are the nearly identical at 530nm but differ at 460 and 660nm and so produce quite different values of the absorption Ångström exponent, both versions of which are shown in **Figures 21** and **22**. In the 2-5.5 km altitude range the wavelength-independent correction factors yield AAE values of 1.2±0.1 in 2016 and 1.1±0.2 in 2017 and 2018. AAE at these same altitudes calculated with the wavelength-specific correction factors are about 0.3-0.4 higher, on average 1.5±0.1 in 2016 and 1.5±0.2 in 2017 and 2018.

The Pistone et al., (2019) comparison of spectral SSA across different instruments during ORACLES 2016 used SSA calculated from σ_{ap} using the wavelength-averaged correction factor. Using the wavelength-specific correction factors produces higher 470nm absorption, with the result that SSA is lower at both 470nm and 660nm than at 530nm (Pistone et al., 2019). In contrast, SSA derived from absorption using the wavelength-averaged correction factors decreases with wavelength. The latter agrees better with the shape of the spectral SSA from the remote sensing instruments, indicating the lower values of AAE (derived from σ_{ap} values using the wavelength-averaged correction) are more likely to be correct. Values of AAE close to 1 are consistent with the absorption being dominated by black carbon (Bergstrom et al., 2007; Bond et al., 2013), so if these lower values are correct there is likely little brown carbon absorption, as also indicated by other recent studies of biomass smoke in the SE Atlantic (Chylek et al., 2019; Denjean et al., 2020; Taylor et al., 2020). These four models simulate both black and organic carbon, but the organic carbon is not light-absorbing so AAE values are expected to

be near 1. They do include the impacts of the addition of water on the aerosol indices of refraction and aerosol size which can drive variations in AAE from black carbon alone (i.e. of about 0.8-1.4; Liu et al., 2018).

AAE from the WRF-CAM5 and GEOS models are significantly lower than the in-situ wavelength-specific values and slightly but not significantly lower than the wavelength-independent values (**Figures 21** and **22**). In both models AAE in the 2-5.5 km altitude range is 1.1 in 2016 and 2017 and 1.2 in 2018, with standard deviations of <0.05. The UM-UKCA AAE values vary from the observed values but on average are in good agreement with the in-situ AAE derived using the wavelength-specific correction factors.
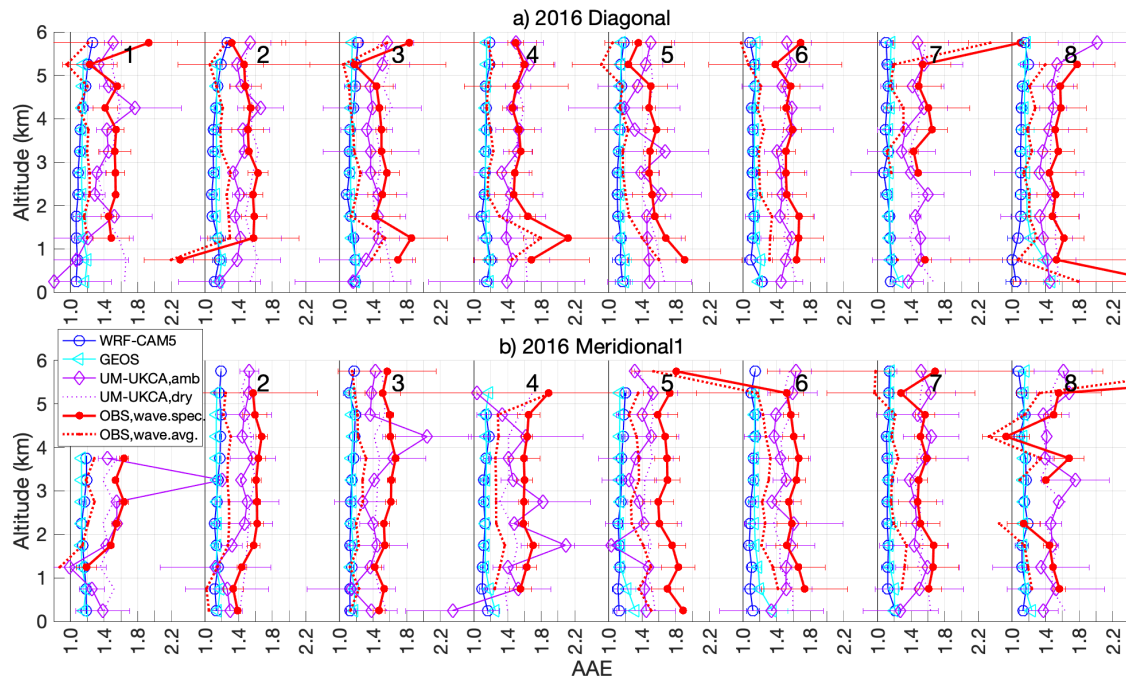
Figure 21. As in Figure 16, but for the absorption Ångström exponent (AAE). Observed values of AAE are given for both the wavelength-specific and wavelength-averaged correction factors.
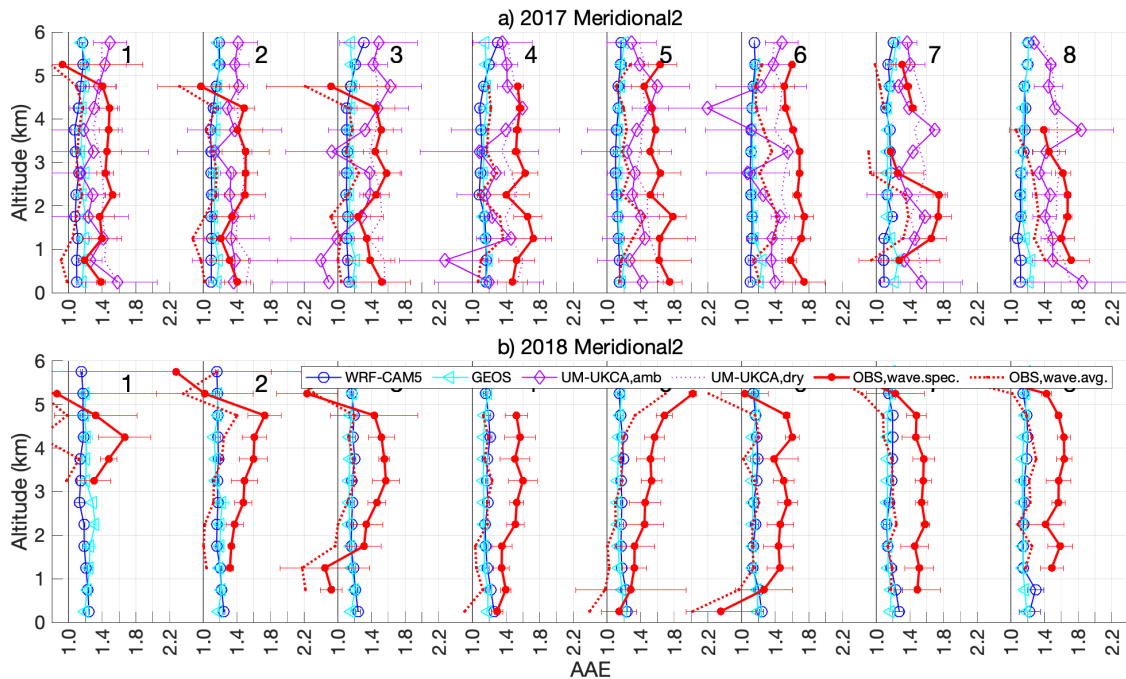
**Figure 22.** As in Figure 17, but for the absorption Ångström exponent (AAE).

4.4 Biases in cloud fraction and cloud optical thickness

Observed cloud properties are retrieved from satellite observations and so are available from every day of the three field campaign periods and for the Zonal transect as well as for the Diagonal, Meridonal1 and Meridional2 transects. Mean CF_{warm} and geometric mean COT_{warm} from the satellite retrievals are compared to model averages across all daytime hours (**Figures 23-25**). We treat the SEVIRI-LaRC retrievals as the benchmark for CF_{warm} since these measurements cover the daytime hours, and the MODIS-ACAERO retrievals as our benchmark for COT_{warm}, since it accounts for the effects of absorbing aerosol above the clouds, while acknowledging that any satellite retrievals of clouds may be subject to systematic biases. In cumulus cloud regions in particular 3-D radiative effects and sub-pixel clear-sky contamination may be biasing the retrieved values of COT_{warm} low (e.g., Marshak et al., 2006; Kato et al., 2006; Painemal et al., 2013) whereas the coarse pixel resolution relative to the cloud size could yield an overestimation of CF_{warm} (e.g., Zhao and Di Girolamo, 2006).

The observed CF_{warm} from all three satellite data products is quite high (>60-70%) across almost all comparison transects gridboxes, except at the southeast end of the Diagonal transect in 2016 (**Figure 23**). Differences in the observation times of the MODIS and SEVIRI instruments are expected, on average, to lead to CF_{warm} values that are about 1-10% lower for the two MODIS products (Section 3.2.3 and **Table S.2**), but in our statistics CF_{warm} from MODIS-Standard and MODIS-

45

ACAERO are not always lower than from SEVIRI-LaRC (**Figures 23-25**). Differences in the spatial resolution (3km for SEVIRI; 1km for MODIS), algorithms used for identifying warm clouds, and in the aggregation of statistics (e.g., the L2 datasets for MODIS-ACAERO versus the L3 dataset for MODIS-Standard) could also be producing differences in derived CF_{warm}. Notably, the uncertainty in the "true" CF_{warm} as expressed through the differences between the satellite products is much lower than the differences between CF_{warm} from the observational datasets and the models.

CF_{warm} in WRF-CAM5 is higher than in all three observational datasets (**Figures 23-25**). This is particularly the case in regions of low cloud fraction, so the gradients in cloud fraction across the transects follow the tendency of the observed gradients but are much smaller in magnitude. In contrast, the GEOS and ALADIN models both significantly underestimate CF_{warm} in all transects and almost all gridboxes. CF_{warm} gradients in the ALADIN model also track well the observed gradients, but at much lower cloud fraction. The GEOS model, in addition to significantly under-estimating CF_{warm}, fails to capture the correct gradient in cloud fraction. In particular, the latitudinal gradient in cloud fraction along the Meridional2
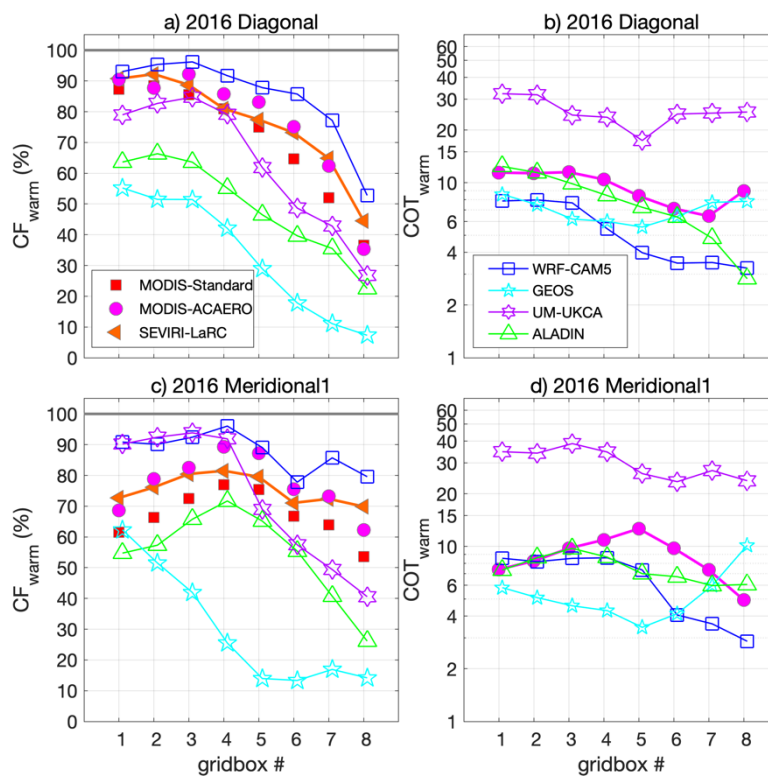

Figure 23. Average daytime mean CF_{warm} (a, c) and COT_{warm} (b, d) from satellite retrievals and from the models for the comparison gridboxes in the 2016 Diagonal (a, b) and Meridional1 (c, d) transect. COT_{warm} is the geometric mean, except for the ALADIN model which shows the median. The SEVIRI-LaRC dataset is used as the reference observed CF_{warm}, and the MODIS-ACAERO dataset is used as the reference observed COT_{warm} in the comparison to models.
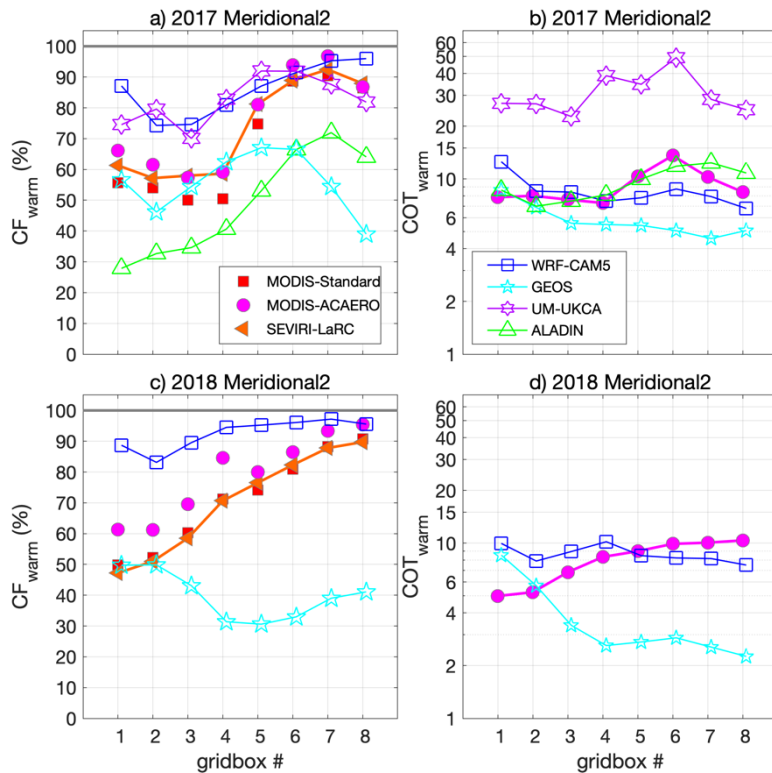
Figure 24. As in Figure 23, but for the 2017 (a, b) and 2018 (c, d) Meridional2 transects.

transect in both 2017 and 2018 is the inverse of that observed. The UM-UKCA model comes closest to the observed cloud fractions, with variable biases depending on the transect and gridbox. Like WRF-CAM5, UM-UKCA biases in cloud fraction are largest where it fails to capture spatial gradients in cloud fraction – e.g., along the Meridonal1 transect, at the north end of the Meridional2 transect, and at the east end of the Zonal transect.

In the SE Atlantic, the large-scale gradients in day-to-day cloud fraction are controlled by a number of different intertwined factors, including gradients in sea surface temperature (SST) from the Benguela current off the Namibian–Angolan coast and by lower tropospheric stability (Wood, 2012). Increases in CF_{warm} in the SE Atlantic have been shown to be correlated with increases in lower tropospheric stability (LTS), surface wind speed and RH at 950 hPa (Fuchs et al., 2018). Seasonally-dependent factors can also affect the SE Atlantic low cloud fields. In September, the intrusion of mid-latitude disturbances to lower latitudes can significant perturb the low clouds, reducing CF_{warm} (Zhang and Zuidema, 2021). Elevated humidity in the free troposphere in October, 2018 would also help reduce cloud-top entrainment drying. In the models, failure to capture these features and the dynamics that drive one or more of these variables could be the cause of incorrect gradients in CF_{warm}. Differences in the representation of small scale turbulent mixing processes and microphysics have been shown to hamper model skill in representing stratocumulus properties, even when large-scale forcings are fixed (Zhu et al., 2005; Wyant et al.,
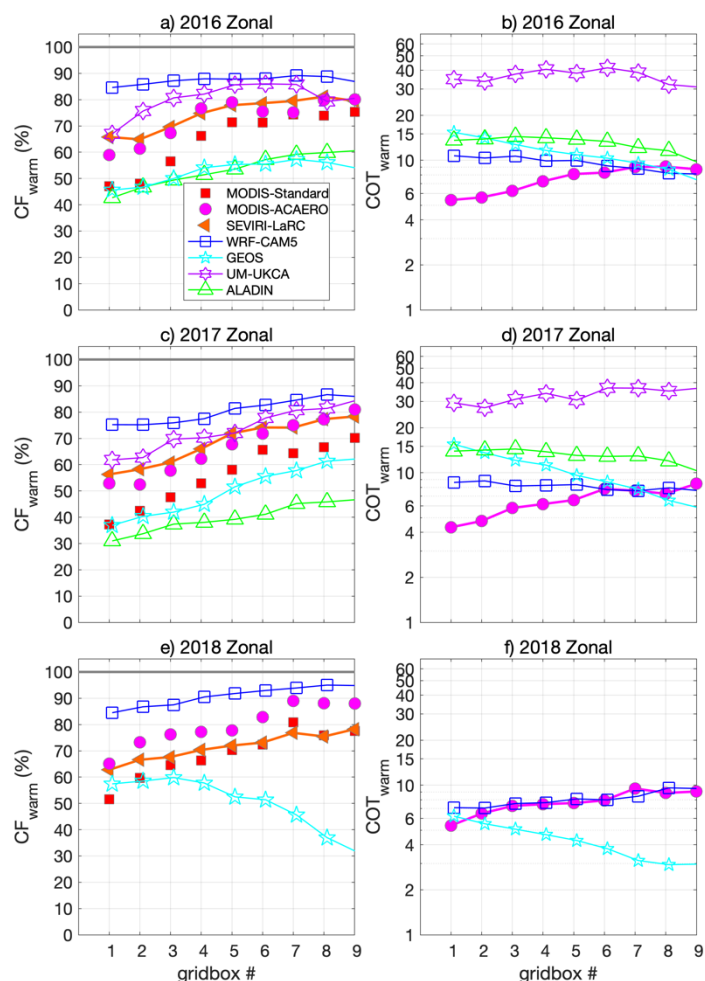
Figure 25. As in Figure 23, but for the Zonal transects in 2016 (a, b), 2017 (c, d) and 2018 (e, f).

1105

2007). Accurate prediction of cloud cover is complicated because the relative roles of different large-scale forcings varies across the region (Fuchs et al., 2018). During the three years of the ORACLES campaign, the SSTs were warmer than the climatological average, though this doesn't appear to have resulted in a significant impact on cloud fraction in the month-long averages (Ryoo et al., 2021).

1110

Disentangling the sources of model biases in COT_{warm} are even more difficult, especially since COT_{warm} may be affected not only by thermodynamic processes but is also very sensitive to cloud microphysical process representation (Wyant et al., 2007) and to aerosol-cloud interactions. As discussed above, the models tend to place the smoke plume at lower altitudes than observed, and therefore to mix more of the plume into the boundary layer and low clouds than is observed. This would

1115 lead to higher aerosol loadings in the boundary layer, higher cloud droplet number concentrations, and possibly higher COT_{warm}, (assuming cloud liquid water path is not significantly reduced in response; Twomey 1977). An exception is for the ALADIN model COT_{warm}, as aerosol microphysical effects on clouds were not simulated. Diagnosing the possible magnitude of this effect on COT_{warm} in the other models is beyond the scope of this paper.

1120 The observed (MODIS-ACAERO) geometric mean COT_{warm} covers a fairly small range, of 8.3±1.8 across all transects and years (**Figures 23-25**). WRF-CAM5 COT_{warm} values (8.1±1.9) are very similar to the observed values on average but deviate from the observed values by not capturing spatial gradients. The result is that WRF-CAM5 sometimes over-estimates and sometimes under-estimates COT_{warm}. ALADIN generally reproduces the observed COT_{warm} well, except at the western end of the Zonal transect, where COT_{warm} is about twice that observed. GEOS COT_{warm} is both too small and more spatially

1125 variable than observed (6.6±3.2); like CF_{warm}, the model also doesn't capture the correct spatial gradients in COT_{warm}. UM-UKCA, significantly overestimates COT_{warm} across all transects, averaging 32.6±6.4.

It has been noted that global models tend to have a "too few, too bright" bias for low-level marine clouds (Nam et al., 2012). Here, none of the four models fit this paradigm, including the two global models (GEOS and UM-UKCA). The regional

1130 WRF-CAM5 model has too many clouds, but the clouds are of about the right brightness; the regional ALADIN model has too few clouds that are generally not bright enough, but sometimes too bright; clouds in the global GEOS model are both too few and not bright enough; and the global UM-UKCA model has too many clouds that are much too bright.

In reality, it is expected that COT_{warm} will tend to increase with CF_{warm}, and this is seen in the MODIS-ACAERO retrievals

1135 (Eqn. [1] and **Figure S.3**). In contrast, the WRF-CAM5, GEOS and ALADIN simulations show no significant change in COT_{warm} with CF_{warm}, so as the cloud field develops to produce greater coverage the clouds are not becoming optically thicker. The range in CF_{warm} covered by the models across the comparison transects included here is smaller than in the observations; a question is whether COT_{warm} would remain largely invariant for CF_{warm} of 0-1.0 in the models. If so, COT_{warm} at lower cloud fractions would be too high in WRF-CAM5, and too low in GEOS and ALADIN. In contrast, in the UM-

1140 UKCA simulations COT_{warm} does increase with CF_{warm}, at approximately the same rate as in the MODIS-ACAERO observations, but COT_{warm} is systematically too high (**Figure S.3**).

5 Impact of aerosol and cloud biases in the Direct Aerosol Radiative Effect

In order to quantify the net effect of model biases on the direct aerosol radiative effect, a first-order DARE estimate is calculated using the gridbox-mean aerosol and cloud properties for five of the comparison gridboxes. The 2016 Diagonal

1145 gridbox 3 was selected for being closer to the center of the plume while (in contrast to gridboxes 1 and 2) having more robust sampling (**Figures 1** and **2**); 2016 Meridional1 gridbox 2 and 2017 and 2018 Meridional2 gridbox 5 for being located

closer to the center of the plume meridionally; and 2017 Meridional2 gridbox 2 in order to have one gridbox with lower cloud fraction (57%), since the other four selected gridboxes all have average CF$_{warm}$ of >75%.

Following Haywood and Shine (1995), DARE at the top of the atmosphere can be estimated as

$$DARE \approx -D \cdot S_o \cdot T_{at}^2 \cdot (1 - A_c) \cdot SSA \cdot \bar{\beta} \cdot AOD \cdot \left((1 - R_s)^2 - \frac{2\,R_s}{\bar{\beta}} \left(\frac{1}{SSA} - 1 \right) \right)$$ [2]

where D is the daylight fraction of the day; S_o is the solar constant; T_{at} is the atmospheric transmissivity (absent aerosol); A_c is cloud fraction; SSA is the single scatter albedo; R_s is the surface reflectance; $\bar{\beta}$ is the spectrally-weighted aerosol hemispheric backscatter fraction; and AOD is the aerosol optical depth. This formulation assumes zero forcing in the presence of clouds (since for A_c=1, $DARE$=0). The goal here is to calculate the forcing for an aerosol plume that, when clouds are present, is fully above the cloud layer and therefore has non-zero forcing. Equation [2] is therefore modified to:

$$DARE \approx -D \cdot S_o \cdot T_{at}^2 \cdot SSA \cdot \bar{\beta} \cdot AOD \cdot \left((1 - \alpha_s)^2 - \frac{2\,\alpha_s}{\bar{\beta}} \left(\frac{1}{SSA} - 1 \right) \right)$$ [3]

where α_s is the "scene" albedo below the aerosol plume and AOD is the above-cloud AOD. In this formulation, the impact of clouds on DARE is accounted for through their effect on α_s. This DARE estimate does not account for the fact that the cloud fields (and therefore α_s) might have been affected by rapid adjustments to the smoke plume direct forcing (the "semi-direct" effect). Depending on the amount and altitude of heating by aerosol absorption above the clouds, this could have increased or decreased α_s, thereby affecting the calculation of DARE using Eqn. [3].

DARE is non-linear with α_s (Eqn. [3] and Cochrane et al., 2021), so here DARE is calculated separately for clear ($DARE_{clear}$) and cloudy ($DARE_{cloudy}$) skies. The gridbox-average DARE ($DARE_{avg}$) is the sum of the two, weighted by their average fractional contributions in each gridbox:

$$DARE_{avg} = DARE_{clear}(1 - CF_{warm}) + DARE_{cloudy}CF_{warm}.$$ [4]

This assumes that the aerosol is not systematically different over clear skies than over cloudy skies, as demonstrated for this region by Kacenelenbogen et al. (2019). The observed values of CF$_{warm}$ used in Eqn. [4] are the gridbox means from the SEVIRI-LaRC retrievals.

For clear skies, α_s in Eqn. [3] is set to 0.07 (approximated from Li et al., 2006 for ocean reflectivity), and for cloudy skies, α_s is the gridbox-average cloud albedo. The two-stream approximation of Feingold et al. (2017) is used to calculate the visible cloud albedo α_c:

$$\alpha_c = \frac{\frac{(1-g)}{\cos\theta_o}\tau_c}{2 + \frac{(1-g)}{\cos\theta_o}\tau_c},$$ [5]

where the asymmetry factor, g, is set to 0.85 (Bohren, 1980), the solar zenith angle, θ_o, is fixed at 30°, and cloud optical thickness, τ_c, is set to the gridbox log-mean value of COT_{warm} from the MODIS-ACAERO retrievals.

In Eqn. [3], D is fixed at 0.5 (which is correct to within 0.02 for this latitude range in all three months), S_o is set to 1361 Wm^{-2} (Kratz et al., 2020), and T_{at} is set to 0.79 based on Figure 1 of Wild et al. (2019). The value $\bar{\beta}$ is calculated using Eqn. 11b of Reid et al. (1999), which parameterizes $\bar{\beta}$ as a function of σ_{ep} at 550nm and the extinction Ångström exponent (EAE) across 437-669nm (close to our wavelength-span of 470-660nm) for biomass burning smoke. For the gridboxes included in this analysis, modeled $\bar{\beta}$ values varied from a low of 0.094 (in WRF-CAM5) to a high of 0.159 (in ALADIN), with observed values in the range 0.11-0.13 (**Table 3**). EAE, used in deriving $\bar{\beta}$, is calculated as:

$$EAE = SSA \cdot SAE + (1 - SSA) \cdot AAE .\qquad\qquad [6]$$

The values of SSA, AAE and SAE used in Eqns. [3] and [6] are extinction-weighted column values and AOD the integral of σ_{ep}, all calculated across 1.5-5.5 km altitude, since this altitude range captures the vast majority of the above-cloud smoke plume in both the observations and the models.

AAE was not reported for the ALADIN model, so the observed value is used in the calculation of DARE (**Table 3**). In addition, in 2018 there were problems with the measurement of SAE, so the observed value in that year is set to 1.8, since SAE in 2016 and 2017 was typically 1.7-1.9 at plume altitudes across most comparison gridboxes. Aerosol properties for the UM-UKCA model are the ambient-RH values.

Equations [3] and [4] provide a valuable tool to represent the functional dependency of DARE on aerosol and cloud properties, as well as surface albedo. However, the resulting values (**Table 3**) are an approximation that does not fully account for all of the factors that influence DARE. For example, a fixed solar zenith angle (30°) is used in calculating cloud albedo, the aerosol backscatter (rather than up-scatter) fraction is used in the calculation, and this formulation doesn't account for the effects of sun angle on atmospheric gaseous transmission (T_a) and on aerosol scattering; spectral variations in aerosol and radiative properties are not included either. The amount of sunlight that interacts with the aerosol at a given altitude also depends on extinction by aerosol at higher altitudes, and this is not accounted for in using a fixed atmospheric transmission factor. In addition, the calculation uses month-long gridbox averages for aerosol and cloud properties. DARE does not scale linearly with SSA or the sub-plume albedo, and therefore with CF_{warm} and COT_{warm}, so the "mean" DARE values presented here will differ from a mean of instantaneous DARE values.

To explore the limitations of Eqn. [3], we perform full radiative transfer calculations for spectrally-resolved upward and downward broadband fluxes (100nm bandwidth in the visible, and 500nm beyond) for cloudy and clear skies, with and without aerosol, using libRadTran (Mayer and Kylling, 2005). From these fluxes, we calculate the instantaneous DARE in

Table 3. TOA DARE$_{avg}$ (in W m^{-2}) calculated using Eqn. [4], and the gridbox-mean observed and modeled aerosol and cloud properties used in the calculation, for select comparison gridboxes. Also given in square brackets after each modeled variable is the ratio of DARE$_{avg}$ calculated using that model's value for the given variable only and the observed values for all other variables, to DARE$_{avg}$ calculated using the observed variables. The values of $\bar{\beta}$, α_c and α_s are shown in italics because they are derived from the observed and modeled parameters (see text). In the table below, $\alpha_s = 0.07(1 - CF_{warm}) + \alpha_c CF_{warm}$ is given as a metric for the combined effect of CF$_{warm}$ and COT$_{warm}$ on DARE. As noted in the text, DARE is actually calculated separately for clear and cloudy skies using Eqn. [3], then DARE$_{avg}$ calculated using Eqn. [4].

	observed	WRF-CAM5	GEOS	UM-UKCA	ALADIN
			2016 Diagonal, gridbox 3		
AOD	0.360	0.254 [0.71]	0.226 [0.63]	0.181 [0.50]	0.276 [0.77]
SSA	0.855	0.841 [1.14]	0.851 [1.04]	0.842 [1.13]	0.892 [0.64]
SAE	1.77	1.05 [1.07]	1.75 [1.00]	1.73 [1.01]	2.08 [0.90]
AAE	1.48	1.12 [1.01]	1.13 [1.01]	1.38 [1.00]	{1.48} [N/A][1]
CF$_{warm}$	0.88	0.96 [1.16]	0.52 [0.30]	0.85 [0.94]	0.64 [0.53]
COT$_{warm}$	11.5	7.6 [0.63]	6.2 [0.44]	24.4 [1.61]	9.9 [0.86]
$\bar{\beta}$	*0.120*	*0.094*	*0.112*	*0.114*	*0.158*
α_c	*0.499*	*0.397*	*0.349*	*0.678*	*0.461*
α_s	*0.448*	*0.384*	*0.215*	*0.587*	*0.320*
DARE$_{avg}$:	**14.8**	**9.9**	**0.3**	**12.7**	**-0.1**
model/observed DARE:		**0.67**	**0.02**	**0.86**	**-0.01**
			2016 Meridional1, gridbox 2		
AOD	0.419	0.257 [0.62]	0.236 [0.56]	0.259 [0.62]	0.375 [0.90]
SSA	0.867	0.833 [1.73]	0.868 [0.98]	0.854 [1.28]	0.885 [0.62]
SAE	1.89	1.20 [1.42]	1.65 [1.24]	1.90 [0.99]	2.05 [0.75]
AAE	1.57	1.15 [1.08]	1.14 [1.08]	1.47 [1.02]	{1.57} [N/A][1]
CF$_{warm}$	0.76	0.90 [1.61]	0.52 [-0.04]	0.92 [1.70]	0.57 [0.17]
COT$_{warm}$	8.3	8.2 [0.99]	5.1 [0.01]	38.7 [3.77]	8.6 [1.10]
$\bar{\beta}$	*0.133*	*0.096*	*0.108*	*0.137*	*0.158*
α_c	*0.417*	*0.415*	*0.306*	*0.770*	*0.427*
α_s	*0.334*	*0.381*	*0.193*	*0.714*	*0.274*
DARE$_{avg}$:	**6.2**	**10.4**	**-1.1**	**21.4**	**-2.4**
model/observed DARE:		**1.68**	**-0.18**	**3.44**	**-0.39**
			2017 Meridional2, gridbox 2		
AOD	0.292	0.450 [1.54]	0.352 [1.21]	0.258 [0.88]	0.485 [1.66]
SSA	0.861	0.835 [1.91]	0.866 [0.82]	0.854 [1.25]	0.888 [0.05]
SAE	1.70	1.02 [1.56]	1.67 [1.05]	1.72 [0.96]	2.06 [-0.09]
AAE	1.44	1.1 [1.10]	1.14 [1.09]	1.34 [1.03]	{1.44} [N/A][1]
CF$_{warm}$	0.57	0.74 [2.46]	0.46 [0.07]	0.80 [2.91]	0.33 [-1.06]
COT$_{warm}$	8.0	8.5 [1.20]	6.9 [0.53]	26.8 [4.52]	7.0 [0.57]
$\bar{\beta}$	*0.114*	*0.094*	*0.109*	*0.113*	*0.160*
α_c	*0.410*	*0.425*	*0.374*	*0.699*	*0.377*
α_s	*0.264*	*0.333*	*0.210*	*0.571*	*0.170*
DARE$_{avg}$:	**2.1**	**14.0**	**-0.7**	**15.6**	**-12.9**
model/observed DARE:		**6.58**	**-0.35**	**7.35**	**-6.08**

52

	2017 Meridional2, gridbox 5				
AOD	0.591	0.370 [*0.62*]	0.389 [*0.65*]	0.252 [*0.42*]	0.562 [*0.94*]
SSA	0.868	0.830 [*1.50*]	0.837 [*1.40*]	0.852 [*1.20*]	0.874 [*0.91*]
SAE	1.80	1.10 [*1.14*]	1.77 [*1.00*]	1.77 [*1.00*]	2.14 [*0.74*]
AAE	1.55	1.11 [*1.02*]	1.14 [*1.02*]	1.30 [*1.01*]	{1.55} [*N/A*][1]
CF$_{warm}$	0.81	0.87 [*1.15*]	0.67 [*0.62*]	0.92 [*1.28*]	0.53 [*0.24*]
COT$_{warm}$	10.4	7.8 [*0.65*]	5.4 [*0.22*]	34.7 [*2.22*]	9.98 [*0.94*]
$\bar{\beta}$	*0.122*	*0.095*	*0.114*	*0.115*	*0.171*
α_c	*0.473*	*0.403*	*0.319*	*0.750*	*0.464*
α_s	*0.397*	*0.360*	*0.237*	*0.696*	*0.279*
DARE$_{avg}$:	**16.0**	**14.0**	**3.4**	**20.7**	**-3.1**
model/observed DARE:		**0.88**	**0.21**	**1.30**	**-0.22**
	2018 Meridional2, gridbox 5				
AOD	0.248	0.165 [*0.67*]	0.261 [*1.06*]	---	---
SSA	0.890	0.851 [*2.04*]	0.877 [*1.35*]	---	---
SAE	1.8[3]	1.22 [*1.36*]	1.68 [*1.13*]	---	---
AAE	1.45	1.18 [*1.05*]	1.13 [*1.05*]	---	---
CF$_{warm}$	0.77	0.95 [*1.87*]	0.31 [*-1.21*]	---	---
COT$_{warm}$	9.0	8.5 [*0.88*]	2.7 [*-1.42*]	---	---
$\bar{\beta}$	0.123	0.096	0.111	---	---
α_c	0.438	0.424	0.190	---	---
α_s	0.353	0.406	0.107	---	---
DARE$_{avg}$:	**3.1**	**6.4**	**-5.7**	---	---
model/observed DARE:		**2.09**	**-1.85**	---	---

cloudy and clear skies. Finally, DARE$_{avg}$ is calculated from the cloud fraction weighted DARE of both cloudy and clear skies, as in Eqn. [4]. To compare with the parameterized DARE$_{avg}$, the instantaneous DARE$_{avg}$ are integrated over 24 hours to obtain the diurnally-averaged DARE. Our simulations use a mid-latitude winter gas profile and correlated-k parameterization from Kato et al. (1999) for spectrally resolved results prior to spectral integration. The dark ocean in the simulation is treated as a Lambertian surface with prescribed wavelength-dependent albedo. A slab aerosol layer is assumed for 2-5 km altitude, and the cloud layer is located at 0.7-1 km. Spectral AOD and SSA are calculated using the EAE and AAE in **Table 3**.

The comparison of parameterized DARE$_{avg}$ with the full radiative transfer calculations are shown in Supplementary **Figure S.22**. We find a high correlation coefficient (R^2=0.95), with relatively few outliers, which are mostly confined to the DARE$_{avg}$ estimates for 2017 Meridional2 gridbox 2. We conclude that the parameterized DARE$_{avg}$ estimates in **Table 3** are useful for providing a first-order estimate of how biases in key aerosol and cloud properties translate to biases in DARE in this region, and we proceed by using the parameterized DARE$_{avg}$ expressions to assess the contribution of each of the variables in **Table 3** to a bias in derived DARE$_{avg}$. These contributions are indicated in square brackets following the mean value of that variable; they are the ratio of DARE$_{avg}$ calculated using that model's value for the given variable only and the

observed values for all other variables, to DARE$_{avg}$ calculated using the observed variables. For example, for the 2016 Diagonal gridbox 3, the WRF-CAM5 low bias in SSA alone drives a 14% high bias in DARE$_{avg}$.

1235   Notably, DARE$_{avg}$ is positive (>0) across all five gridboxes when calculated using the observed aerosol and cloud properties and the properties from the WRF-CAM5 and UM-UKCA models. In contrast, it is negative in all five gridboxes using the properties simulated with ALADIN and negative for three of the five gridboxes for GEOS (**Table 3**). The modeled ambient-RH 1.5-5.5 km AOD is lower than the observed, low-RH values for almost all gridboxes and models, but this does not translate directly to lower DARE. Even in those gridboxes where observed AOD is higher (see Meridional2 in both 2017 and

1240   2018 in **Table 3**) DARE$_{avg}$ calculated from the model properties can be either larger and more positive or smaller and of the opposite sign to DARE$_{avg}$ calculated from the observed properties. This is because biases in different variables often counteract each other.

This can be seen in the calculations for gridbox 2 in the 2017 Meridional2 transect. This example stands out in that the

1245   modeled AOD is larger than observed in three of the four models (WRF-CAM5, GEOS and ALADIN). CF$_{warm}$ in this gridbox is also lower than in the other four gridboxes (0.57 versus >0.75). In the WRF-CAM5 model this high AOD bias combines with, in particular, a high bias in modeled CF$_{warm,}$ and a low bias in SSA to produce DARE$_{avg}$ that is a factor of 6.6 larger than when calculated using the observed properties. In contrast, in ALADIN an AOD high bias of a similar magnitude combines with a significant low bias in CF$_{warm,}$ and a high bias in SSA to produce a DARE$_{avg}$ that is 6.1 times larger than that

1250   using observed properties – but of the opposite sign.

Across the five gridboxes, biases in σ_{ep} (AOD) and CF$_{warm}$ and COT$_{warm}$ (through their role in determining α_s) alternately make the largest contributions to biases in DARE$_{avg}$ in many of the models/gridboxes. Biases in SSA are usually the source of somewhat smaller DARE$_{avg}$ biases, but it is a still significant contributor across most models and gridboxes. Low biases in

1255   SAE in the WRF-CAM5 and GEOS-5 models and a high bias in SAE in the ALADIN model also can drive biases on the order of 30-40% through its role in determining $\bar{\beta}$ (see Eqn. [3]).

DARE$_{avg}$ derived from the WRF-CAM5 properties vary from being within about 30% of DARE$_{avg}$ calculated using the observed properties in two of the five gridboxes to having significant high biases in the other three (factors of 1.7, 6.6 and

1260   2.1). In these latter three cases, the consistent low bias in SSA and high bias in CF$_{warm}$ more than offsets a low bias in AOD in two of the gridboxes and adds to the high bias in AOD in the third. This is not the case in 2016 Diagonal gridbox 3, where SSA and CF$_{warm}$ are still biased low and high, respectively, but combined with a low bias in COT$_{warm}$, the resulting DARE$_{avg}$ is much close to DARE$_{avg}$ from the observed properties. The excellent agreement in 2017 Meridional 2 gridbox 5 in DARE using the observed and WRF-CAM5 properties also results from compensating biases: the simulated AOD and COT$_{warm}$ bias

1265   DARE$_{avg}$ low and simulated SSA and (to a lesser degree) SAE and CF$_{warm}$ bias DARE$_{avg}$ high, nearly exactly offsetting each

other. This shows how qualitatively consistent biases in a given model's representation of aerosol and cloud properties key to DARE can combine to produce a large range of biases in modeled DARE.

In GEOS, the extinction-weighted SSA in the plume introduces small (<20%) low biases in $DARE_{avg}$ in three of the
1270 gridboxes and 35-40% low biases in the other two. More significant for this model is larger low biases in AOD in three of the five gridboxes and systematic low biases in CF_{warm}, and COT_{warm}. These result in values of $DARE_{avg}$ that are too small and, for three of the five cases, produce negative rather than positive values. As in WRF-CAM5, biases in different variables can offset each other. For example, correcting for AOD alone would produce even larger negative values of forcing for three of the five gridboxes, increasing the difference between $DARE_{avg}$ from the modeled and observed properties.
1275

In the UM-UKCA model, a high bias in CF_{warm} and a large high bias in COT_{warm} make the sub-plume scene albedo on the order of a factor of two too high, driving large high biases in $DARE_{avg}$. This, combined with a small (~0.01-0.02) low bias in SSA, more than compensates for the low bias in AOD to produce values of $DARE_{avg}$ that are too large in three of the four gridboxes tested, and significantly so (by factors of 3.4 and 7.4) in two of the gridboxes. Correction to just the aerosol fields
1280 would produce universally too-high $DARE_{avg}$; correction to just the cloud fields, conversely, would produce universally too-low $DARE_{avg}$.

The ALADIN model consistently simulates too-small CF_{warm} and too-high SSA. These are sufficient to produce a negative direct aerosol radiative effect across all five gridboxes, in contrast with the positive $DARE_{avg}$ calculated from the observed
1285 values. In 2017 Meridional2 gridbox 2 the CF_{warm} bias alone is sufficient to produce negative DARE. Small low biases in AOD and COT_{warm} and a high bias in SAE also combine to produce values of $DARE_{avg}$ that are too small (AOD and SAE) and too negative (COT_{warm}).

These findings support that of earlier studies (e.g. Chand et al., 2009; Stier et al. 2013; Zuidema et al., 2016) that emphasize
1290 the importance of accurately simulating cloud fraction in order to get accurate estimates of direct forcing by biomass burning aerosol over the SE Atlantic. They also highlight the importance of quantifying the relative roles of the aerosol and cloud properties that control the direct aerosol radiative effect, since the magnitude, sign and source(s) of DARE biases can vary with the aerosol and cloud properties themselves. The limited analysis presented here makes it clear that models can have compensating biases, such that model improvements that make one key parameter more accurate could actually lead to less
1295 accurate simulated values of DARE. This first-order analysis provides a framework for a future study that employs full radiative transfer calculations that use, for example, the full 2-D profiles of observed and modeled cloud properties and account for diurnal effects, and that accounts for uncertainties and variability in observed and modeled fields.

6 Discussion and conclusions

The WRF-CAM5 and GEOS models were used to test for representativeness of the observations of the biomass burning plume along our comparison transects, using aerosol light extinction as the metric (Section 4.1). This approach assumes that the models accurately represent variability in σ_{ep}, even if there are biases in the mean values of σ_{ep}. A first-order test indicates this is a good assumption in 2016 but that the two models had different levels of variability from each other and from the observations in 2017 and 2018 (Section 2.2). This is reflected in the different results from the two models when testing for representativeness. The representativeness of a given set of samples within the models also varies between years, even for the same transect (Meridional2), indicating systematic differences between the models at interannual timescales and/or for different locations. In addition, model invariance in the biomass burning plume aerosol intensive properties (e.g., SSA) made the models not useful for testing the representativeness of sampled aerosol intensive optical properties.

With the exception of the WRF-CAM5 model in 2018, the models simulated either comparable or higher variability σ_{ep} within the comparison transects. As such, with that one exception they likely present a conservative estimate of the representativeness of the observations. Though there were some exceptions, sampled values of σ_{ep} in the 2-5km altitude range across the Diagonal (2016), Meridional1 (2016) and Meridional2 (2017 and 2018) transects were generally within 20% of the approx. month-long period of each years' campaign. This altitude range encompasses the core of the biomass burning plume in most comparison gridboxes and campaign years. The fact that the modelled plume concentrations (as measured by σ_{ep}) at the sampled times were this close to the month-long averages is surprising given that, even with about half the ORACLES flights dedicated to "Routine track" sampling, data was collected for, at most, only 1-2 hours of the full approximately month-long campaign period in each year for a given gridbox and 500m altitude bin (**Figure 2**).

Biases in the plume altitude and concentration were tested through comparisons to observed CO concentration, σ_{ep}, and BC and OA concentrations across three campaign years covering different months (September 2016, August 2017 and October 2018) and therefore different parts of the African biomass burning season. Biases in CO for the two models that reported it (WRF-CAM5 and GEOS) suggest under-estimates in emissions or possibly in the efficiency of transport of the biomass burning plume over the SE Atlantic from the burning source regions, since CO is not affected by scavenging processes. An earlier assessment of GEOS representation of the African biomass burning plume indicates that, for that model, transport biases are the more likely cause (Das et al., 2017). In both models, the low bias in CO was larger in October, 2018, which is towards the end of the biomass burning season, than in August, 2017 and September, 2016. Notably, both of these models use QFED2 emissions.

In the core of the plume, low biases in BC in WRF-CAM5 and GEOS were somewhat smaller than the CO low biases. In other words, the CO:BC ratio was somewhat lower in the models than the observations, particularly in the October 2018

Meridional2 transect, and more so in the GEOS model than in WRF-CAM5. The ratio of CO:BC in biomass burning primary emissions depends on the material being burned and the efficiency of burning (smoldering versus flaming) (e.g. Reid et al., 2005), but this is set within the QFED emissions and so cannot explain these inter-model differences. Differences in anthropogenic sources could also be contributing (e.g. WRF-CAM5 uses EDGAR-HTAP while GEOS uses AeroCom Phase

1335 II), as could differences in the "background" CO concentrations. In October 2018, when differences between the models and the observations were largest, the biomass burning plume was less intense, so for that month the background and anthropogenic emissions could be more strongly influencing the CO and BC concentrations. For the biomass burning aerosol itself, given the common emissions dataset used by the two models, differences in the CO:BC ratio between the models must be due to differences in-atmosphere chemistry and processing, combined with dynamics, leading to different aerosol

1340 scavenging rates. Notably, WRF-CAM5 has more sophisticated aerosol chemistry than GEOS. Greater scavenging losses in the first couple of days after emission, e.g., mostly over the land, in reality than in the models could also be contributing to the lower CO:BC ratio in models than in the observations.

Model biases in BC versus in OA, and how these biases evolve along the aerosol transport pathway, also give some insight

1345 to model processes. This is because BC is a refractory, primary aerosol; it is not produced or destroyed in the atmosphere (Bond et al., 2013). OA, on the other hand, is emitted directly as an aerosol as well as being formed in the atmosphere in secondary production from gas phase constituents, and it lost in the atmosphere through evaporation back to the gas phase, photo-chemical transformation and/or heterogenous oxidation (e.g. Hallquist et al., 2009; O'Brien and Kroll, 2019).

1350 In most gridboxes above the boundary layer there is a smaller low bias (or, in some locations a greater high bias) in OA than in BC, in the three models that report both parameters (WRF-CAM5, GEOS, and UM-UKCA). The higher OA:BC ratio in the models, as reflected in their respective relative biases, is more pronounced in 2017 and 2018 and in the GEOS model, and it tends to be lower at the core of the plume than at the plume edges. This could originate from a number of model biases: primary emissions having too high a ratio of OA:BC, too much secondary organic aerosol (SOA) production, and/or

1355 insufficient loss of organics with aerosol aging. Again, WRF-CAM5 and GEOS both use the GFED emissions, so should have the same OA:BC ratio in primary emissions. The UM-UKCA model, however, uses the FEER inventory which may have a different OA:BC ratio in emissions from these fires. For OA, in-atmosphere production and losses can be significant. Previous studies have shown that SOA can be produced rapidly – within minutes to hours – after emission (e.g., Jimenez et al., 2009; Bond et al., 2013). OA can also be produced and lost on time-scales of days to >1 week after emission (Capes et

1360 al., 2008; Wagstrom et al., 2009; Cubison et al., 2011; Jolleys et al., 2015; Hodzic et al., 2015; Collier et al., 2016; Konovalov et al., 2019; Hodshire et al., 2019; Cappa et al., 2020).

Model-based age estimates indicate that the aerosol we sampled during ORACLES was almost always at least two days old, so our observations only inform us how the OA:BC ratio evolved starting several days after emission. Observations from

57

1365 ORACLES-2016 may ultimately not be able to discriminate loss of OA through aging from differences in the OA mass in the source emissions. Regardless, processes that drive in-atmosphere OA losses on these longer (multi-day) timescales are not implemented in any of the models included here, and this could lead to higher model OA:BC ratios for aged aerosol. However, we cannot rule out too high ratio of OA:BC in emissions and too much secondary organic aerosol (SOA) production, although the latter is less likely as models tend to show low production of SOA compared to observations 1370 (Hodzic et al., 2016).

Biases in σ_{ep} stem from the combined biases in aerosol component (e.g., BC and OA) masses and in the mass extinction efficiency. The latter depends in part on aerosol water content, especially above ~40-50% RH. Here, the in-situ observed values of σ_{ep} were made at low (<40%) RH, whereas the HSRL-2 measured and the modeled values were at ambient RH. All 1375 four models significantly underestimate in σ_{ep}, with low biases in σ_{ep} greater than for BC or OA. Consistent with this, Shinozuka et al. (2020) calculated a proxy for the mass extinction efficiency, $\sigma_{ep}/(OA+BC)$, from the observations and models, and found it was lower in the models than the observations, including for the 3-6km altitude column. For spherical particles and mid-visible wavelengths, the mass scattering efficiency increases with aerosol diameter between about 100nm and 450nm diameter, then decreases above about 600nm (e.g., Saide et al., 2020). The SAE provides a proxy for aerosol 1380 size; assuming a mono-modal size distribution, typical SAE values indicate an aerosol effective diameter of approx. 380-400nm for ALADIN (SAE of 2.0-2.2), 420nm for the observations and GEOS (SAE of 1.8), 400-420nm for UM-UKCA (SAE of 1.8-2.0), and 700nm for WRF-CAM5 (SAE of 1.0) (Schuster et al., 2006). Because the mass extinction efficiency peaks at about 500nm, aerosol size alone would drive it higher for the observations, GEOS and UM-UKCA models than for ALADIN – but it should be comparable for the observations and WRF-CAM5 despite the SAE differences (see Figure 10a 1385 of Saide et al., 2020). In this case, a more likely source of the apparent low bias in model mass extinction efficiency are the real indices of refraction used in the models for aerosol components, as the OA real refractive index used in WRF-CAM5 is 1.45 while literature values for biomass burning are more often in the range 1.52-1.55 range (Aldhaif et al., 2018).

The CO, BC, OA, and σ_{ep} comparisons all indicate that the models simulated plumes that are too vertically diffuse. Too 1390 much vertical diffusion in the models maybe responsible for, in particular, the plume top terminating at lower altitude in the in-situ observations than in some of the simulations, often leading to low biases in modeled CO, BC, OA, and σ_{ep} in the 2-5km altitude range and significant relative (but small absolute) high biases in the 5-6km range in the comparisons. It isn't fully clear, however, whether this is a robust result, given that the HSRL-2, like the models, measured extinction extending to higher altitudes than did the in-situ observations (Section 4.2.3).

1395

In the GEOS, UM-UKCA and ALADIN models it also appears that either the smoke is not lofted sufficiently high over the continent or that subsidence is too strong in the models, particularly in 2016, but also in 2018 (for GEOS). In the WRF-CAM5 model all biomass burning emissions are injected into the surface-most model layer; this smoke is lifted and mixes in

the continental boundary layer, which grows to a depth of typically about 3.5-4.0 km (Labonne et al., 2007) but can reach 4.5-5.5 km (Ryoo et al., 2021). In the UM-UKCA model, emissions are added to the boundary layer such that concentrations taper from higher values at the surface to zero at 3 km above the surface. Burning progresses southward through the biomass burning season, with the land surface elevation where burning is occurring shifting from <500m in the Congo-Zaire basin to >1500m in the Namibia-Kalahari dryland. This increase in elevation assists the lofting of the smoke (Ryoo et al., 2021). Notably, the models under-estimate the smoke plume height during the later months of the burning season, when fires are sourced at higher elevations, indicating possible issues with the model representation of boundary layer development over land. It is also possible that lifting of the plume driven by sub-gridscale processes (Freitas et al., 2006) and/or by aerosol "self-lifting" through absorption and heating (Boers et al., 2010; de Laat et al., 2012) that is not fully accounted for in the models.

The tendency for the models to have too-diffuse a bottom edge of the plume and a plume that is too low in altitude will lead to greater mixing of the aerosol into clouds, and therefore aerosol-cloud interactions. The vertical distance between cloud top and the biomass burning plume could also affect semi-direct forcing in this region (Adebiyi and Zuidema, 2018). Based on the altitude-dependence to the model bias in aerosol concentrations, the impact of these biases is more pronounced in September 2016 and August 2017 than in October 2018.

While the magnitude of aerosol scattering and absorption over this region is largely controlled by above-cloud AOD, or vertically-integrated σ_{ep}, the sign of the direct effect is controlled by the aerosol SSA in the plume and by sub-plume albedo (here, largely controlled by CF_{warm}). In the observations, SSA increases with altitude in the plume in September, 2016 and October, 2018 but not in August, 2017. These vertical variations were not captured by any of the models (**Figure 14**). Both WRF-CAM5 and GEOS do, however, have overall higher SSA in August (2018) than in September and October (2016 and 2018), as do the observations.

Co-albedo (1-SSA) differences, weighted by σ_{ep}, translate directly to differences in absorbed energy. Ambient-RH SSA is lower (and co-albedo higher) than the observed dry SSA in the WRF-CAM5, GEOS and UM-UKCA models; in ALADIN, the SSA is both higher and more variable than observed. These biases vary with altitude, with some of the largest differences in modeled and observed SSA towards the top of the plume. Large SSA biases at altitudes with very little light extinction will, however, have little impact on DARE. At altitudes where the plume is largely concentrated (2.5-5km), on average the co-albedo in the model is biased high by ~5-10% in UM-UKCA, ~15% in GEOS-5, and 15-20% in WRF-CAM5, relative to the dry observed values. ALADIN co-albedo is biased low by about 10-35% on average. These biases combine with biases in σ_{ep} to affect the atmospheric absorption and therefore, in addition to DARE, the marine low cloud responses to atmospheric absorption above the clouds.

All of the values above are for mid-visible (530 or 550nm) SSA, but of course DARE operates over the full solar spectrum. Spectral SSA is, in turn, directly related to SAE and AAE. Thus, uncertainty in AAE translates into uncertainty in spectral SSA and, in the context of DARE, the amount of sunlight absorbed in the atmosphere. The observed values of σ_{ap} are well-constrained at 530nm, but they are very uncertain at shorter and longer wavelengths (470 and 660nm), where the PSAP measurements have not been as robustly calibrated. For the ORACLES biomass aerosol, the two different Virkkula (2010) calibrations yield AAE values of about 1.2 (wavelength-averaged correction) and 1.5 (wavelength-specific correction), whereas the modeled values average 1.1-1.2, with little difference across the three field campaign years. Notably, the lower values agree well with AAE values measured near Ascension Island during the UK CLARIFY 2017 campaign using a photoacoustic spectrometer to measure absorption (Taylor et al., 2020).

A question is whether this uncertainty in AAE leads to significant uncertainty in DARE. By definition, the AAE parameterization of absorption change versus wavelength is linear in log-space, so for higher AAE the increase in absorption at shorter wavelengths is stronger than the decrease towards longer wavelengths. However, the downwelling solar spectrum in the troposphere peaks at ~450nm and drops off more rapidly at shorter wavelengths than longer wavelengths. The impact on atmospheric absorption, and therefore DARE, of differing values of AAE results from the convolution of these spectral dependencies of aerosol absorption and downwelling solar radiation.

To quantify this effect, we calculated the 300-750nm integrated atmospheric absorption for aerosol with AAE of 1.0, 1.2 and 1.5, using a fixed 550nm SSA of 0.86, a value of SAE=1.8, and a clear-sky spectral downwelling solar radiation typical of mid-latitude fall. We find that integrated absorption for AAE=1.5 is only 3% greater than for AAE=1.2 and only 4% greater than for AAE=1.0. The offsetting effects of the spectral dependencies of AAE and solar flux allow DARE to be fairly insensitive to uncertainties in AAE. Therefore the observed model biases in AAE – relative to either of the possible observed AAE values – will not contribute significantly to biases in modeled DARE, consistent with the findings of de Graaf et al. (2014).

In the ORACLES study region, the sub-plume albedo is a function of CF$_{warm}$, cloud albedo (α_c), and the ocean surface albedo. Because of the large difference between cloud albedo and ocean surface albedo, CF$_{warm}$ is a strong controller of sub-plume albedo, with higher CF$_{warm}$ driving more positive DARE. Across our comparison transects, WRF-CAM5 tended to over-estimate CF$_{warm}$, and GEOS and ALADIN to under-estimate CF$_{warm}$, with the UM-UKCA coming closest to reproducing the observations but still tending to be biased high (**Figure 18**). GEOS and ALADIN in particular also had different gradients in CF$_{warm}$ with latitude (Meridional transects) and longitude (Zonal transect) than was observed; the 2016 Diagonal transect is the only comparison transect where all models largely captured the CF$_{warm}$ gradient. The large difference in COT$_{warm}$ between the observations, WRF-CAM5, GEOS and ALADIN (range: 8-11) versus in UM-UKCA (range: 24-39) translates to a significant high bias in α_c in the UM-UKCA model, ranging from 40% (2016 Diagonal1 gridbox 3) to 85%

(2016 Meridional gridbox 2) (Section 5.0 and **Table 3**). This will combine with any high biases in CF_{warm} in the UM-UKCA model to produce too-positive (warming) direct aerosol radiative effects and is sufficient to more than compensate for any small low biases in CF_{warm}.

1470

First-order calculations of DARE for select gridboxes in the comparison transects demonstrate how these translate into biases in aerosol radiative effects for the above-cloud aerosol (Section 5). Earlier studies have shown that different models simulate everything from large negative to large positive direct aerosol radiative forcing by the biomass burning aerosol over the SE Atlantic (Zuidema et al., 2016 and Stier et al., 2013). Consistent with this, DARE calculated using simulated aerosol
1475 and cloud properties for five of our comparison gridboxes spanned -12 Wm^{-2} to 20 Wm^{-2} across the four models. In contrast, DARE calculated from the observed properties were all positive, ranging from 2 to 16 Wm^{-2}. Using this simplified calculation we showed that, across these five gridboxes, biases in σ_{ep} (and therefore AOD) and in CF_{warm} and COT_{warm} (through their role in determining the albedo below the aerosol plume) alternately make the largest contributions to biases in DARE in many of the models/gridboxes. SSA is a source of smaller but still significant biases in some cases as is, in one
1480 case, the simulated SAE, through its impact on the aerosol hemispheric backscatter fraction.

Calculations of how DARE is affected by biases in each of the observed aerosol and cloud properties included in this comparison study reveal that biases in different properties often produce offsetting biases in DARE. As a result, improving model representation of just one field (e.g. AOD for GEOS or just the cloud fields for UM-UKCA) would actually increase
1485 the bias in simulated DARE. This highlights the importance of testing for and correcting biases in all simulated properties that affect DARE, which in this region includes the representation of low marine clouds. It also provides motivation for a more thorough assessment of direct aerosol radiative forcing over the SE Atlantic that accounts for the model biases identified herein.

Data availability

1490 The P-3 and ER-2 observational data are available as follows:
ORACLES Science Team: Suite of Aerosol, Cloud, and Related Data Acquired Aboard P3 During ORACLES 2016, Version 3, NASA Ames Earth Science Project Office, Accessed at doi: 10.5067/Suborbital/ORACLES/P3/2016_V3, 2020
ORACLES Science Team: Suite of Aerosol, Cloud, and Related Data Acquired Aboard ER2 During ORACLES 2016, Version 3, NASA Ames Earth Science Project Office, Accessed at doi: 10.5067/Suborbital/ORACLES/ER2/2016_V3, 2021
1495 ORACLES Science Team: Suite of Aerosol, Cloud, and Related Data Acquired Aboard P3 During ORACLES 2017, Version 3, NASA Ames Earth Science Project Office, Accessed at doi: 10.5067/Suborbital/ORACLES/P3/2017_V3, 2020
ORACLES Science Team: Suite of Aerosol, Cloud, and Related Data Acquired Aboard P3 During ORACLES 2018, Version 3, NASA Ames Earth Science Project Office, Accessed at doi: 10.5067/Suborbital/ORACLES/P3/2018_V3, 2020

1500 The aggregated model and aerosol observational products are available at:

https://espo.nasa.gov/sites/default/files/box_P3ER2Models_2016mmdd_R8.nc

Author contributions

SPB, RF, AD, SF, SGH, JRP, operated instruments during the ORACLES intensive observation periods. PES, CH, GAF, HG, MM, PN, GRC, AdS, delivered model products. KM and DP provided and assisted with analysis of satellite cloud
1505 products for the ORACLES intensive observation periods. PES, SJD, JR, RW and PZ formulated the model-observation comparison. SD processed all observational data and applied statistical techniques. SJD wrote most of the first draft. JR, IC and LG provided the full radiative transfer calculations for testing the parameterized DARE and wrote the associated text. SD, PES, PZ, GAF, HG, MM, KM, DM, SPB, RF, KP, RW and JR edited the manuscript. JR, RW and PZ led the efforts to acquire funding for the ORACLES mission.

1510 **Competing Interests**

The authors declare that they have no conflict of interest.

Acknowledgements

References

Adebiyi, A. A. and Zuidema, P.: The Role of the Southern African Easterly Jet in Modifying the Southeast Atlantic Aerosol and Cloud Environments, Q. J. Royal Met. Soc., 142 (697), 1574–89, https://doi.org/10.1002/qj.2765, 2016.

1535 Adebiyi, A. and Zuidema, P.: Low cloud sensitivity to biomass-burning aerosols and meteorology over the southeast Atlantic, J. Climate, 31, p. 4329-4346, https://doi.org/10.1175/JCLI-D-17-0406.1, 2018.

Adebiyi, A. A., Zuidema, P., Chang, I., Burton, S. P., and Cairns, B.: Mid-level clouds are frequent above the southeast Atlantic stratocumulus clouds, Atmos. Chem. Phys., 20, 11025-11043, https://doi.org/10.5194/acp-20-11025-2020, 2020.

1540 Albayrak, A., Wei, J., Petrenko, M., Lynnes, C. S., and Levy, R. C.: Global bias adjustment for MODIS aerosol optical thickness using neural network, J. Appl. Remote Sens., 7(1), 073514, https://doi.org/10.1117/1.JRS.7.073514, 2013.

Aldhaif, A. M., Stahl, C., Braun, R. A., Moghaddam, M. A., Shingler, T., Crosbie, E., Sawamura, P., Dadashazar, H., Ziemba, L., Jimenez, J. L., Campuzano-Jost, P., and Sorooshian, A.: Characterization of the Real Part of Dry Aerosol Refractive Index Over North America From the Surface to 12 km, J. Geophys. Res. Atmos., 123, 8283-8300,
1545 https://doi.org/10.1029/2018jd028504, 2018.

Anderson, T. L. and Ogren, J. A.: Determining aerosol radiative properties using the TSI 3563 integrating nephelometer, Aerosol Sci. Technol., 29, 57–69, 1998.

Bergstrom, R. W., Pilewskie, P., Russell, P. B., Redemann, J., Bond, T. C., Quinn, P. K., and Sierau, B.: Spectral absorption properties of atmospheric aerosols, Atmos. Chem. Phys., 7, 5937–5943, https://doi.org/10.5194/acp-7-5937-2007, 2007.

1550 Boers, R., deLaat, A. T., Stein Zweers, D. C. and Dirksen, R. J.: Lifting potential of solar-heated aerosol layers, Geophys. Res. Lett., 37, L24802, https://doi.org/10.1029/2010GL045171, 2010.

Bohren, C. F.: Multiple scattering of light and some of its observable consequence, Am. J. Phys., 55, 524–533, 1980.

Bond, T. C., T. L. Anderson, and Campbell, D.: Calibration and intercomparison of filter-based measurements of visible light absorption by aerosols, Aerosol Sci. Tech., 30, 582-600, 1999.

1555   Bond, T. C., Doherty, S. J., Fahey, D. W., Forster, P. M., Berntsen, T., DeAngelo, B. J., Flanner, M. G., Ghan, S., Kärcher, B., Koch, D., Kinne, S., Kondo, Y., Quinn, P. K., Sarofim, M. C., Schultz, M. G., Schulz, M., Venkataraman, C., Zhang, H., Zhang, S., Bellouin, N., Guttikunda, S. K., Hopke, P. K., Jacobson, M. Z., Kaiser, J. W., Klimont, Z., Lohmann, U., Schwarz, J. P., Shindell, D., Storelvmo, T., Warren, S. G., and Zender, C. S.: Bounding the role of black carbon in the climate system: A scientific assessment, J. Geophys. Res.-Atmos., 118, 5380–5552, https://doi.org/10.1002/jgrd.50171,
1560   2013.

Bretherton, C. S. and Park, S.: A New Moist Turbulence Parameterization in the Community Atmosphere Model, J. Clim., 22(12), 3422–3448, 2009.

Brown, H., Liu, X., Pokhrel, R., Murphy, S., Mielonen, T., Kokkola, H., Bergman, T., Myhre, G., Watson-Paris, D., Stier, P., Johnson, B., Bellouin, N., Vakkari, V., Beukes, J. P., van Zyl, P. G., Liu, S., and Chand, D.: Biomass burning
1565   aerosols in most climate models are too absorbing, Nat. Comm., 12 (277), https://doi.org/10.1038/s41467-020-20482-9, 2021.

Burgos, M.A., Andrews, E., Titos, G., Alados-Arboledas, L., Baltensperger, U., Day, D., Jefferson, A., Kalivitis, N., Mihalopoulos, N., Sherman, J., Sun, J., Weingartner, E., and Zieger, P.: A global view on the effect of water uptake on aerosol particle light scattering, Scientific Data, 6(157), https://doi.org/10.1038/s41597-019-0158-7, 2019.

1570   Burton, S. P., Hostetler, C. A., Cook, A. L., Hair, J. W., Seaman, S. T., Scola, S., Harper, D. B., Smith, J. A., Fenn, M. A., Ferrare, R. A., Saide, P. E., Chemyakin, E. V., and Müller, D.: Calibration of a high spectral resolution lidar using a Michelson interferometer, with data examples from ORACLES, Appl. Optics, 57, 6061-6075, https://doi.org/10.1364/AO.57.006061, 2018.

Capes, G., Johnson, B., McFiggans, G., Williams, P. I., Haywood, J., Coe, H.: Aging of biomass burning aerosols over West
1575   Africa: Aircraft measurements of chemical composition, microphysical properties, and emission ratios, J. Geophys. Res.,113, https://doi.org/10.1029/2008jd009845, 2008.

Cappa, C. D., Lim, C. Y., Hagan, D. H., Coggon, M., Koss, A., Sekimoto, K., de Gouw, J., Onasch, T. B., Warneke, C., and Kroll, J. H.: Biomass-burning-derived particles from a wide variety of fuels – Part 2: Effects of photochemical aging on particle optical and chemical properties. Atmos. Chem. Phys., 20, 8511-8532, https://doi.org/10.5194/acp-20-8511-
1580   2020, 2020.

Carter, T. S., Heald, C. L., Cappa, C. D., Kroll, J. H., Campos, T. L., Coe, H., Cotterell, M. I. Davies, N. W., Farmer, D. K., Fox, C., Garofalo, L. A., Hu, L., Langridge, J. M., Levin, E. J. T., Murphy, S. M., Pokhrel, R. P., Shen, Y., Szpek, K, Taylor, J. W., Wu, H.: Investigating carbonaceous aerosol and its absorption properties from fires in the western United States (WE-CAN) and southern Africa (ORACLES and CLARIFY), J. Geophys. Res. Atmos., 126 (15),
1585   e2021JD034984, https://doi.org/10.1029/2021JD034984.

Chand, D., Wood, R., Anderson, T. L., Satheesh, S. K. and Charlson, R. J.: Satellite-derived direct radiative effect of aerosols dependent on cloud cover, Nat. Geosci., 2, 181-184, https://doi.org/10.1038/NGEO437, 2009.

Chang, I., Gao, L., Burton, S. P., Chen, H., Diamond, M. S., Ferrare, R. A., Flynn, C. J., Kacenelenbogen, M., LeBlanc, S. E., Meyer, K. G., Pistone, K., Schmidt, S., Segal-Rozenhaimer, M., Shinozuka, Y., Wood, R., Zuidema, P., Redemann, J., and Christopher, S. A.: Spatiotemporal heterogeneity of aerosol and cloud properties over the southeast Atlantic: An observational analysis, Geophys. Res. Lett., https://doi.org/10.1029/2020GL091469, 2021.

Chin, M., Ginoux, P., Kinne, S., Torres, O., Holben, B. N., Duncan, B. N., Martin, R. V., Logan, J. A., Higurashi, A. and Nakajima, T.: Tropospheric Aerosol Optical Thickness from the GOCART Model and Comparisons with Satellite and Sun Photometer Measurements, J. Atmos. Sci., 59(3), 461–483, 2002.

Cho, H.-M., Zhang, Z., Meyer, K., Lebsock, M., Platnick, S., Ackerman, A. S., Di Girolamo L., C.-Labonnote, L., Cornet, C., Riedi, J., and Holz, R. E.: Frequency and causes of failed MODIS cloud property retrievals for liquid phase clouds over global oceans, J. Geophys. Res. Atmos., 120(9), 4132–4154, http://doi.org/10.1002/2015JD023161, 2015.

Chylek, P., Lee, J. E., Romonosky, D. E., Gallo, F., Lou, S., Shrivastava, M., Carrico, C. M., Aiken, A. C., and Dubey, M. K.: Mie scattering captures observed optical properties of ambient biomass burning plumes assuming uniform black, brown, and organic carbon mixtures, J. Geophys. Res., 124, 11406-11427, https://doi.org/10.1029/2019jd031224, 2019.

Cochrane, S. P., Schmidt, K. S., Chen, H., Pilewskie, P., Kittelman, S., Redemann, J., LeBlanc, S., Pistone, K., Kacenelenbogen, M., Segal Rozenhaimer, M., Shinozuka, Y., Flynn, C., Dobracki, A., Zuidema, P., Howell, S., Freitag, S. and Doherty, S.: Empirically derived parameterizations of the direct aerosol radiative effect based on ORACLES aircraft observations. Atmos. Meas. Tech., 14(1), 567–593. https://doi.org/10.5194/amt-14-567-2021, 2021.

Coddington, O. M., Pilewskie, P., Redemann, J., Platnick, S., Russell, P. B., Schmidt, K. S., Gore, W. J., Livingston, J., Wind, G., and Vukicevic, T.: Examining the impact of overlying aerosols on the retrieval of cloud optical properties from passive remote sensing, J. Geophys. Res., 115, D10211, doi:10.1029/2009JD012829, 2010.

Colarco, P., da Silva, A., Chin, M. and Diehl, T.: Online simulations of global aerosol distributions in the NASA GEOS-4 model and comparisons to satellite and ground-based aerosol optical depth, J. Geophys. Res., 115(D14), doi:10.1029/2009jd012820, 2010.

Colarco, P. R., Nowottnick, E. P., Randles, C. A., Yi, B., Yang, P., Kim, K.-M., Smith, J. A., Bardeen, C. G.: Impact of radiatively interactive dust aerosols in the NASA GEOS-5 climate model: Sensitivity to dust particle shape and refractive index, J. Geophys. Res. Atmos., 119 (2), https://doi.org/10.1002/2013JD020046, 2014.

Collier, S., Zhou, S., Onasch, T. B., Jaffe, D. A., Kleinma, L., Sedlacek, A. J., Briggs, N. L., Hee, J., Fortner, E., Shilling, J. E., Worsnop, D., Yokelson, R. J., Parworth, C., Ge, X., Xu, J., Butterfield, Z., Chand, D., Dubey, M. K., Pekour, M. S., Springston, S., and Zhang, Q.: Regional Influence of Aerosol Emissions from Wildfires Driven by Combustion Efficiency: Insights from the BBOP Campaign. Environ Sci Technol 50, 8613-8622, https://doi.org/10.1021/acs.est.6b01617, 2016.

Cubison, M. J., Ortega, A. M., Hayes, P. L., Farmer, D. K., Day, D., Lechner, M. J., Brune, W. H., Apel, E., Diskin, G. S., Fisher, J. A., Fuelberg, H. E., Hecobian, A., Knapp, D. J., Mikoviny, T., Riemer, D., Sachse, G. W., Sessions, W., Weber, R. J., Weinheimer, A. J., Wisthaler, A., and Jimenez, J. L.: Effects of aging on organic aerosol from open

biomass burning smoke in aircraft and laboratory studies, Atmos. Chem. Phys., 11, 12049-12064, https://doi.org/10.5194/acp-11-12049-2011, 2011.

Darmenov, A. S. and da Silva, A. M.: The Quick Fire Emissions Dataset (QFED): Documentation of Versions 2.1, 2.2 and
1625   2.4. Volume 38; Technical Report Series on Global Modeling and Data Assimilation, [online] Available from: https://ntrs.nasa.gov/search.jsp?R=20180005253 (Accessed 9 May 25 2019), 2015.

Das, S., Harshvardhan, H., Bian, H., Chin, M., Curci, G., Protonotariou, A. P., Mielonen, T., Zhang, K., Wang, H., and Liu, X.:, Biomass burning aerosol transport and vertical distribution over the South African-Atlantic region, J. Geophys. Res. Atmos., 122, 6391–6415, https://doi.org/10.1002/2016JD026421, 2017.

1630 Dee, D. P., Uppala, S. M., Simmons, A. J., Berrisford, P., Poli, P., Kobayashi, S., Andrae, U., Balmaseda, M. A., Balsamo, G., Bauer, P., Bechtold, P., Beljaars, A. C. M., van de Berg, L., Bidlot, J., Bormann, N., Delsol, C., Dragani, R., Fuentes, M., Geer, A. J., Haimbergere, L., Healy, S. B., Hersbach, H., Hólm, E. V., Isaksen, L., Kallberg, P., Köhler, M., Matricardi, M., McNally, A. P., Monge-Sanzf, B. M., Morcrette, J.-J., Park, B.-K., Peubey, C., de Rosnaya, P., Tavolato, C., Thépaut, J.-N., and Vitart, F.: The ERA-Interim reanalysis: configuration and performance of the data
1635   assimilation system, Q. J. Royal Met. Soc., 137, 553–597, https://doi.org/10.1002/qj.828, 2011.

de Graaf, M., Bellouin, N., Tilstra, L. G., Haywood, J. and Stammes, P.: Aerosol direct radiative effect of smoke over clouds over the southeast Atlantic Ocean from 2006 to 2009, Geophys. Res. Lett., 41, 7723–7730, https://doi.org/10.1002/2014GL061103, 2014.

de Laat, A. T. J., Stein Zweers, D. C., Boers, R., and Tuinder, O. N. E.: A solar escalator: Observational evidence of the self-
1640   lifting of smoke and aerosols by absorption of solar radiation in the February 2009 Australian Black Saturday plume, J. Geophys. Res. Atmos., 117, D04204, https://doi.org/10.1029/2011JD017016, 2012.

Denjean, C., Brito, J., Libois, Q., Mallet, M., Bourrianne, T., Burnet, F., Dupuy, R., Flamant, C., and Knippertz, P.: Unexpected biomass burning aerosol absorption enhancement explained by black carbon mixing state, Geophys. Res. Lett, 47, https://doi.org/10.1029/2020gl089055, 2020.

1645 Dey, S., Di Girolamo, L., & Zhao, G.: Scale effect on statistics of the macrophysical properties of trade wind cumuli over the tropical western Atlantic during RICO. J. Geophys. Res., 113(D24), D24214. http://doi.org/10.1029/2008JD010295, 2008.

Diamond, M. S., Dobracki, A., Freitag, S., Small Griswold, J. D., Heikkila, A., Howell, S. G., Kacarab, M. E., Podolske, J. R., Saide, P. E. and Wood, R.: Time-dependent entrainment of smoke presents an observational challenge for assessing
1650   aerosol–cloud interactions over the southeast Atlantic Ocean. Atmospheric Chemistry and Physics. 18(19), 14623-14636, https://doi.org/10.5194/acp-18-14623-2018, 2018.

Feingold, G., Balsells, J., Glassmeier, F., Yamaguchi, T., Kazil, J., and McComiskey, A.: Analysis of albedo versus cloud fraction relationships in liquid water clouds using heuristic models and large eddy simulation, J. Geophys. Res. Atmos., 122, 7086–7102, https://doi.org/10.1002/ 2017JD026467, 2017.

1655 Formenti, P., Elbert, W., Maenhaut, W., Haywood, J., Osborne, S. and Andreae, M. O.: Inorganic and carbonaceous aerosols during the Southern African Regional Science Initiative (SAFARI 2000) experiment: Chemical characteristics, physical properties, and emission data for smoke from African biomass burning, J. Geophys. Res. D: Atmos., 108(D13) [online] Available from: https://onlinelibrary.wiley.com/doi/abs/10.1029/2002JD002408, 2003.

Formenti, P., et al.: The Aerosols, Radiation and Clouds in Southern Africa Field Campaign in Namibia: Overview,
1660 illustrative observations, and way forward. Bull. Amer. Meteor. Soc., 100, 1277–1298, 1380, https://doi.org/10.1175/BAMS-D-17-0278.1, 2019.

Forster, P., Storelvmo, T., Armour, K., Collins, W., Dufresne, J. L., Frame, D. Lunt, D. J., Mauritsen, T., Palmer, M. D., Watanabe, M., Wild, M., Zhang, H.: The Earth's Energy Budget, Climate Feedbacks, and Climate Sensitivity. In: Climate Change 2021: The Physical Science Basis. Contribution of Working Group I to the Sixth Assessment Report of
1665 the Intergovernmental Panel on Climate Change [Masson-Delmotte, V., P. Zhai, A. Pirani, S. L. Connors, C. Péan, S. Berger, N. Caud, Y. Chen, L. Goldfarb, M. I. Gomis, M. Huang, K. Leitzell, E. Lonnoy, J.B.R. Matthews, T. K. Maycock, T. Waterfield, O. Yelekçi, R. Yu and B. Zhou (eds.)]. Cambridge University Press, In Press, 2021.

Freitas, S. R., Longo, K. M. and Andrea, M. O.: Impact of including the plume rise of vegetation fires in numerical simulations of associated atmospheric pollutants, Geophys. Res. Lett., 33, L17808,
1670 https://doi.org/10.1029/2006GL026608, 2006.

Fuchs, J. Cermak, J. and Andersen, H.: Building a cloud in the southeast Atlantic: understanding low-cloud controls based on satellite observations with machine learning, Atmos. Chem. Phys., 18, 16537–16552, https://doi.org/10.5194/acp-18-16537-2018, 2018.

Gordon, H., Field, P. R., Abel, S. J., Dalvi, M., Grosvenor, D. P., Hill, A. A., Johnson, B. T., Miltenberger, A. K., Yoshioka,
1675 M. and Carslaw, K. S.: Large simulated radiative effects of smoke in the south-east Atlantic, Atmos. Chem. Phys., 18(20), 15261–15289, 2018.

Gupta, S., McFarquhar, G. M., O'Brien, J. R., Delene, D. J., Poellot, M. R., Dobracki, A., Podolske, J. R., Redemann, J., LeBlanc, S. E., Segal-Rozenhaimer, M., and Pistone, K.: Impact of the variability in vertical separation between biomass-burning aerosols and marine stratocumulus on cloud microphysical properties over the Southeast Atlantic,
1680 Atmos. Chem. Phys., 21, 4615–4635, https://doi.org/10.5194/acp-21-4615-2021, 2021.

Hair, J. W., Hostetler, C. A., Cook, A. L., Harper, D. B., Ferrare, R. A., Mack, T. L., Welch, W., Izquierdo, L. R. and Hovis, F. E.: Airborne High Spectral Resolution Lidar for profiling aerosol optical properties, Appl. Opt. 47, 6734-6752, https://doi.org/10.1364/AO.47.006734, 2008.

Hallquist, M., Wenger, J. C., Baltensperger, U., Rudich, Y., Simpson, D., Claeys, M., Dommen, J., Donahue, N. M., George,
1685 C., Goldstein, A. H., Hamilton, J. F., Herrmann, H., Hoffmann, T., Iinuma, Y., Jang, M., Jenkin, M. E., Jimenez, J. L., Kiendler-Scharr, A., Maenhaut, W., McFiggans, G., Mentel, Th. F., Monod, A., Prévôt, A. S. H., Seinfeld, J. H., Surratt, J. D., Szmigielski, R. and Wildt, J.: The formation, properties and impact of secondary organic aerosol: current and emerging issue. Atmos. Chem. Phys., 9, 5155–5236, https://doi.org/10.5194/acp-9-5155-2009, 2009.

Haywood, J. M. and Shine, K. P.: The effect of anthropogenic sulfate and soot aerosol on the clear sky planetary radiation budget, Geophys. Res. Lett., 22 (5), 603-606, 1995.

Haywood, J. M., Osborne, S. R., and Abel, S. J.: The effect of overlying absorbing aerosol layers on remote sensing retrievals of cloud effective radius and cloud optical depth, Q. J. Roy. Meteorol. Soc., 130, 779–800, 2004.

Haywood, J. M., Abel, S. J., Barrett, P. A., Bellouin, N., Blyth, A., Bower, K. N., Brooks, M., Carslaw, K., Che, H., Coe, H., Cotterell, M. I., Crawford, I., Cui, Z., Davies, N., Dingley, B., Field, P., Formenti, P., Gordon, H., de Graaf, M., Herbert, R., Johnson, B., Jones, A. C., Langridge, J. M., Malavelle, F., Partridge, D. G., Peers, F., Redemann, J., Stier, P., Szpek, K., Taylor, J. W., Watson-Parris, D., Wood, R., Wu, H., and Zuidema, P.: Overview: The Cloud-Aerosol-Radiation Interaction and Forcing: Year-2017 (CLARIFY-2017) measurement campaign, Atmos. Chem. Phys., 21, 1049–1084, 2021 https://doi.org/10.5194/acp-21-1049-2021, 2021.

Heald, C. L., Goldstein, A. H., Allan, J. D., Aiken, A. C., Apel, E., Atlas, E. et al.: Total observed organic carbon (TOOC) in the atmosphere: a synthesis of North American observations, Atmos. Chem. Phys., 8, 2007–2025, https://doi.org/10.5194/acp-8-2007-2008, 2008.

Herbert, R. J., Bellouin, N., Highwood, E. J., and Hill, A. A.: Diurnal cycle of the semi-direct effect from a persistent absorbing aerosol layer over marine stratocumulus in large-eddy simulations, Atmos. Chem. Phys., 20, 1317–1340, https://doi.org/10.5194/acp-20-1317-2020, 2020.

Hodzic, A., Madronich, S., Kasibhatla, P. S., Tyndall, G., Aumont, B., Jimenez, J. L., Lee-Taylor, J., and Orlando, J.: Organic photolysis reactions in tropospheric aerosols: effect on secondary organic aerosol formation and lifetime, Atmos. Chem. Phys., 15, 9253-9269, https://doi.org/10.5194/acp-15-9253-2015, 2015.

Hodzic, A., Kasibhatla, P. S., Jo, D. S., Cappa, C. D., Jimenez, J. L., Madronich, S., and Park, R. J.: Rethinking the global secondary organic aerosol (SOA) budget: stronger production, faster removal, shorter lifetime, Atmos. Chem. Phys., 16, 7917–7941, https://doi.org/10.5194/acp-16-7917-2016, 2016.

Ichoku, C. and Ellison, L.: Global top-down smoke-aerosol emissions estimation using satellite fire radiative power measurements, Atmos. Chem. Phys., 14(13), 6643–6667, 2014.

Jimenez, J. L., Canagaratna, M. R., Donahue, N. M., Prevot, A. S. H., Zhang, Q., Kroll, J. H., DeCarlo, P. F., Allan, J. D., Coe, H., Ng, N. L., Aiken, A. C., Docherty, K. S., M. Ulbrich, I. M., Grieshop, A. P., Robinson, A. L., Duplissy, J., Smith, J. D., Wilson, K. R., Lanz, V. A., Hueglin, C., Sun, Y. L., Tian, J., Laaksonen, A., Raatikainen, T., Rautiainen, J., Vaattovaara, P., Ehn, M., Kulmala, M., Tomlinson, J. M., Collins, D. R., Cubison, M. J. Dunlea, E. J., Huffman, J. A., Onasch, T. B., Alfarra, M. R., Williams, P. I., Bower, K., Kondo, Y., Schneider, J., Drewnick, F., Borrmann, S., Weimer, S., Demerjian, K., Salcedo, D., Cottrell, L., Griffin, R., Takami, A., Miyoshi, T., Hatakeyama, S., Shimono, A., Sun, J. Y., Zhang, Y. M., Dzepina, K., Kimmel, J. R., Sueper, D., Jayne, J. T., Herndon, S. C., Trimborn, A. M., Williams, L. R., Wood, E. C., Middlebrook, A. M., Kolb, C. E., Baltensperger, U., Worsnop, D. R.: Evolution of organic aerosols in the atmosphere, Science, 326, 1525-1529, Science, https://doi.org/10.1126/science.1180353, 2009.

68

Johnson, B. T., Shine, K. P., and Forster, P. M.: The semi-direct aerosol effect: Impact of absorbing aerosols on marine stratocumulus, Q. J. Royal Met. Soc., 130 (599), 1407-1422, https://doi.org/10.1256/qj.03.61, 2004.

Jolleys, M. D., Coe, H., McFiggans, G., Taylor, J. W., O'Shea1, S. J., Le Breton, M., Bauguitte, S. J.-B., Moller, S., Di Carlo, P., Aruffo, E., Palmer, P. I., Lee, J. D., Percival, C. J., and Gallagher, M. W.: Properties and evolution of biomass burning organic aerosol from Canadian boreal forest fires, Atmos. Chem. Phys., 15, 3077-3095, https://doi.org/10.5194/acp-15-3077-2015, 2015.

Kacarab, M., Thornhill, K. L., Dobracki, A., Howell, S. G., O'Brien, J. R., Freitag, S., Poellot, M. R., Wood, R., Zuidema, P., Redemann, J., and Nenes, A.: Biomass burning aerosol as a modulator of the droplet number in the southeast Atlantic region, Atmos. Chem. Phys., 20, 3029–3040, https://doi.org/10.5194/acp-20-3029-2020, 2020.

Kacenelenbogen, M. S., Vaughan, M. A., Redemann, J., Young, S. A., Liu, Z., Hu, Y., Omar, A. H., LeBlanc, S., Shinozuka, Y., Livingston, J., Zhang, Q., and Powell, K. A.: Estimations of global shortwave direct aerosol radiative effects above opaque water clouds using a combination of A-Train satellite sensors, Atmos. Chem. Phys., 19, 4933- 4962, https://doi.org/10.5194/acp-19-4933-2019, 2019.

Kaiser, J. W. and Van der Werf, G. R.: [Land surface properties] Biomass burning [in "State of Climate in 2014"]. Bulletin of the American Meteorological Society (BAMS), 96 (7), S56-57, 2015.

Kasten, F.: Visibility forecast in the phase of pre-condensation, Tellus, 21, 631–635, 1969.

Kato, S., Ackerman, T. P., Mather, J. H., and Clothiaux, E.: The k–distribution method and correlated–k approximation for a shortwave radiative transfer model, J. Quant. Spectrosc. Radiat. Transfer, 62, 109–121, 1999.

Kato, S., Hinkelman, L. M., and Cheng, A.: Estimate of satellite-derived cloud optical thickness and effective radius errors and their effect on computed domain-averaged irradiances, J. Geophys. Res., 111, D17201, doi:10.1029/2005JD006668, 2006.

Kawai, H. and Shige, S.: Marine low clouds and their parameterization in climate models, J. Met. Soc. Japan, 98 (6), 1097-1127, https:doi.org/10.2151/jmsj.2020-059, 2020.

Koch, D., and Del Genio, A. D.: Black carbon semi-direct effects on cloud cover: Review and synthesis. Atmos. Chem. Phys., 10(16), 7685–7696. https://doi.org/10.5194/acp-10-7685-2010, 2010.

Konovalov, I. B., Beekmann, M., Golovushkin, N. A., ans Andreae, M. O.: Nonlinear behavior of organic aerosol in biomass burning plumes: a microphysical model analysis, Atmos. Chem. Phys. 19, 12091-12119, https://doi.org/10.5194/acp-19-12091-2019, 2019.

Koren, I., Dagan, G., and Altaratz, O.: From aerosol-limited to invigoration of warm convective clouds, Science, 344, 1143-1146, 10.1126/science.1252595, 2014.

Kotchenruther, R. A., and Hobbs, P. V.: Humidification factors of aerosols from biomass burning in Brazil, J. Geophys. Res. Atmos., 103, D24, 32-081-32,089, https://doi.org/10.1029/98JD00340, 1998.

Kratz, D. P., Gupta, S. K., Wilber, A. C., and Sothcott, V. E.: Validation of the CERES Edition-4A Surface-Only Flux Algorithms, Journal of Applied Meteorology and Climatology, 59(2), 281-295, https://doi.org/10.1175/JAMC-D-19-0068.1, 2020.

Mathieu Labonne, M., Bréon, F. M., and Chevallier, F.: Injection height of biomass burning aerosols as seen from a spaceborne lidar, Geophys. Res. Lett., 34, L11806, https://doi.org/10.1029/2007GL029311, 2007.

LeBlanc, S. E., Redemann, J., Flynn, C., Pistone, K., Kacenelenbogen, M., Segal-Rosenheimer, M., Shinozuka, Y., Dunagan, S., Dahlgren, R. P., Meyer, K., Podolske, J., Howell, S. G., Freitag, S., Small-Griswold, J., Holben, B., Diamond, M., Formenti, P., Piketh, S., Maggs-Kölling, G., Gerber, M. and Namwoonde, A.: Above Cloud Aerosol Optical Depth from airborne observations in the South-East Atlantic, Atmos. Chem. Phys., 20(3), 1565-1590, https://doi.org/10.5194/acp-2019-43, 2019.

Li, J., Scinocca, Lazare, M., McFarelane, N., Von Salzen, K., and Soldheim, L.: Ocean Surface Albedo and Its Impact on Radiation Balance in Climate Models, 19, 6314-6333, https://doi.org/10.1175/JCLI3973.1, 2006.

Liu, X., Huey, L. G., Yokelson, R. J., Selimovic, V., Simpson, I. J., Müller, M., Jimenez, J. L., Campuzano-Jost, P., Beyersdorf, A. J., Blake, D. R., Butterfield, Z., Choi, Y., Crounse, J. D., Day, D. A., Diskin, G. S., Dubey, M. K., Fortner, E., Hanisco, T. F., Hu, W., King, L. E., Kleinman, L., Meinardi, S., Mikoviny, T., Onasch, T. B., Palm, B. B., Peischl, J., Pollack, I. B., Ryerson, T. B., Sachse, G. W., Sedlacek, A. J., Shilling, J. E., Springston, S., St. Clair, J. M., Tanner, D. J., Teng, A. P., Wennberg, P. O., Wisthaler, A. and Wolfe, G. M.: Airborne measurements of western U.S. wildfire emissions: Comparison with prescribed burning and air quality implications, J. Geophys. Res. D: Atmos., 122(11), 6108–6129, 2017.

Liu. C., Chung, C. E., Yin, Y and Schnaiter, M.: The absorption Ångström exponents of black carbon: from numerical aspects, Atmos. Chem. Phys., 18, 6259–6273, https://doi.org/10.5194/acp-18-6259-2018, 2018.

Ma, P.-L., Rasch, P. J., Fast, J. D., Easter, R. C., Gustafson, W. I., Jr., Liu, X., Ghan, S. J. and Singh, B.: Assessing the CAM5 physics suite in the WRF-Chem model: implementation, resolution sensitivity, and a first evaluation for a regional case study, Geoscientific Model Development, 7(3), 755–778, 2014.

Mallet, M., Solmon, F., Roblou, L., Peers, F., Turquety, S., Wa- quet, F., Jethva, H., and Torres, O.: Simulation of Optical Properties and Direct and Indirect Radiative Effects of Smoke Aerosols Over Marine Stratocumulus Clouds During Summer 2008 in California With the Regional Climate Model RegCM, J. Geophys. Res.-Atmos., 122, 10288–10313, https://doi.org/10.1002/2017JD026905, 2017.

Mallet, M., Nabat, P., Zuidema, P., Redemann, J., Sayer, A. M., Stengel, M., Schmidt, S., Cochrane, S., Burton, S., Ferrare, R., Meyer, K., Saide, P., Jethva, H., Torres, O., Wood, R., Saint Martin, D., Roehrig, R., Hsu, C. and Formenti, P.: Simulation of the transport, vertical distribution, optical properties and radiative impact of smoke aerosols with the ALADIN regional climate model during the ORACLES-2016 and LASIC experiments, Atmos. Chem. Phys., 19(7), 4963–4990, 2019.

Mallet, M., Solmon, F., Nabat, P., Elguindi, N., Waquet, F., Bouniol, D., Sayer, A.M., Meyer, K., Roehrig, R., Michou, M., Zuidema, P., Flamant, C.m, Redemann, J. and Formenti, P.: Direct and semi-direct radiative forcing of biomass burning aerosols over the Southeast Atlantic (SEA) and its sensitivity to absorbing properties : a regional climate modeling study., Atmos. Chem. Phys., 20, 13191–13216, https://doi.org/10.5194/acp-20-13191-2020, 2020.

Marshak, A., Platnick, S., Várnai, T., Wen, G., and Cahalan, R. F.: Impact of three-dimensional radiative effects on satellite retrievals of cloud droplet sizes, J. Geophys. Res., 111, D09207, doi:10.1029/2005JD006686, 2006.

Matus, A. V., L'Ecuyer, T. S., Kay, J. E., Hannay, C. and Lamarque, J.-F.: The role of clouds in modulating global aerosol direct radiative effects in spaceborne active observations and the Community Earth System Model, J. Climate, 28(8), 2986- 3003, https://doi.org/10.1175/JCLI-D-14-00426.1, 2015.

Mayer, B. and Kylling, A.: Technical note: The libRadtran software package for radiative transfer calculations – description and examples of use, Atmos. Chem. Phys., 5, 1855–1877, 2005.

McFiggans, G., Artaxo, P., Baltensperger, U., Coe, H., Facchini, M. C., Feingold, G., Fuzzi, S., Gysel, M., Laaksonen, A., Lohmann, U., Mentel, T. F., Murphy, D. M., O'Dowd, C. D., Snider, J. R., and Weingartner, E.: The effect of physical and chemical aerosol properties on warm cloud droplet activation, Atmos. Chem. Phys., 6, 2593–2649, https://doi.org/10.5194/acp-6-2593-2006, 2006.

McNaughton, C. S., Clarke, A. D., Howell, S. G., Pinkerton, M., Anderson, B., Thornhill, L., Hudgins, C., Winstead, E., Dibb, J. E., Scheuer, E. and Maring, H.: Results from the DC-8 Inlet Characterization Experiment (DICE): Airborne Versus Surface Sampling of Mineral Dust and Sea Salt Aerosols, Aerosol Science and Technology, 41:2, 136-159, https://doi.org/10.1080/02786820601118406, 2007.

Meyer, K. G., Platnick, S. E., Oreopoulos, L. and Lee, D.: Estimating the direct radiative effect of absorbing aerosols overlying marine boundary layer clouds in the southeast Atlantic using MODIS and CALIOP, J. Geophys. Res. Atmos., 118 (10): 4801-4815, https://doi.org/10.1002/jgrd.50449, 2013.

Meyer, K., Platnick, S. and Zhang, Z.: Simultaneously inferring above-cloud absorbing aerosol optical thickness andunderlying liquid phase cloud optical and microphysical properties using MODIS, J. Geophys. Res. Atmos., 120, 5524–5547, https://doi.org/10.1002/2015JD023128, 2015.

Minnis, P., Nguyen, L., Palikonda, R., Heck, P. W., Spangenberg, D. A., Doelling, D. R., Ayers, J. K., Smith, W. L., Khaiyer, M. M., Trepte, Q. Z., Avey, L. A., Chang, F.-L., Yost, C. R., Cheer, T. L. and Szedung, S.-M.: Near-real time cloud retrievals from operational and research meteorological satellites. Remote Sensing of Clouds and the Atmosphere XIII, R. H. Picard et al., Eds., International Society for Optical Engineering (SPIE Proceedings, Vol. 7107), https://doi.org/10.1117/12.800344, 2008.

Minnis P., Sun-Mack, S., Young, D. F., Heck, P. W., Garber, D. P., Chen, Y., Spangenberg, D. A., Arduini, R. F., Trepte, Q. Z., Smith, W. L., Ayers, J. K., Gibson, S. C., Miller, W. F., Hong, G., Chakrapani, V., Takano, Y., Liou, K.-N., Xie, Y. and Yang, P., 2011a, CERES Edition-2 cloud property retrievals using TRMM VIRS and Terra and Aqua MODIS

1820   data—Part   I: Algorithms.   IEEE   Trans.   Geosci.   Remote   Sens.,   49,   4374–4400, doi:10.1109/TGRS.2011.2144601,https://ieeexplore.ieee.org/document/5783916/, 2011a.

Minnis., P., Sun-Mack, S., Chen, Y., Yi, Y., Ayers, J. K., Brown, R. R., Dong, X., Gibson, S. C., Heck, P. W., Lin, B., Nordeen, M. L., Nguyen, L., Palikonda, R., Smith, W. L., Spangenberg, D. A.. Trepte, Q. Z. and Xi, B.: CERES Edition-2 cloud property retrievals using TRMM VIRS and Terra and Aqua MODIS data—Part II: Examples of average
1825   results   and   comparisons   with   other   data.   IEEE   Trans.   Geosci.   Remote   Sens.,   49,   4401-4430,   doi: 10.1109/TGRS.2011.2144602, https://ieeexplore.ieee.org/document/5783917/, 2011b.

Molod, A., Takacs, L., Suarez, M. and Bacmeister, J.: Development of the GEOS-5 atmospheric general circulation model: evolution from MERRA to MERRA2, Geoscientific Model Development, 8(5), 1339–1356, 2015.

Nabat, P., Somot, S., Cassou, C., Mallet, M., Michou, M., Bouniol, D., Decharme, B., Drugé, T., Roehrig, R. and Saint-
1830   Martin, D.: Modulation of radiative aerosols effects by atmospheric circulation over the Euro-Mediterranean region, Atmos. Chem. Phys., 20, 8315–8349, https://doi.org/10.5194/acp-20-8315-2020, 2020.

Nam, C., Bony, S., Dufresne, J.-L., and Chepfer, H.: The 'too few, too bright' tropical low-cloud problem in CMIP5 models, Geophys. Res. Lett., 39, L21801, doi:10.1029/2012GL053421, 2012.

Niedermeier, D., Wex, H., Voigtländer, J., Stratmann, F., Brügge- mann, E., Kiselev, A., Henk, H., and Heintzenberg, J.:
1835   LACIS- measurements and parameterization of sea-salt particle hygro- scopic growth and activation, Atmos. Chem. Phys., 8, 579–590, https://doi.org/10.5194/acp-8-579-2008, 2008.

Noda, A. T., and Satoh, M.: Intermodel variances of subtropical stratocumulus environments simulated in CMIP5 models." Geophysical Research Letters 41(21): 7754-7761, doi:10.1002/2014GL061812, 2014.

O'Brien, R. E. and Kroll, J. H.: Photolytic Aging of Secondary Organic Aerosol: Evidence for a Substantial Photo-
1840   recalcitrant Fraction, J. Phys. Chem. Lett., 10, 4003-4009, https://doi.org/ 10.1021/acs.jpclett.9b014172019, 2019.

Painemal, D., Minnis, P., and Sun-Mack, S.: The impact of horizontal heterogeneities, cloud fraction, and liquid water path on warm cloud effective radii from CERES-like Aqua MODIS retrievals, Atmos. Chem. Phys., 13, 9997–10003, https://doi.org/10.5194/acp-13-9997-2013, 2013.

Painemal, D., Xu, K.-M., Cheng, A. and Palikonda, R.: Mean structure and diurnal cycle of Southeast Atlantic boundary
1845   layer clouds: Insights from satellite observations and multiscale modeling framework simulations, J. Climate, 28(1), 324-341, https://doi.org/10.1175/JCLI-D-14-00368.1, 2015.

Penner, J. E., Yang, S. Y. and Chuang, C. C.: Soot and smoke aerosol may not warm climate, J. Geophys. Res., 108, 4657, https://doi.org/10.1029/2003JD003409, 2003.

Petters, M. D. and Kreidenweis, S. M.: A single parameter representation of hygroscopic growth and cloud condensation
1850   nucleus activity, Atmos. Chem. Phys., 7(8), 1961–1971, 2007.

Pistone, K., Redemann, J., Doherty, S. , Zuidema, P., Burton, S., Cairns, B., Cochrane, S., Ferrare, R., Flynn, C., Freitag, S., Howell, S. G., Kacenelenbogen, M., LeBlanc, S., Liu, X., Schmidt, K. S., Sedlacek III, A. J., Segal-Rozenhaimer, M., Shinozuka, Y., Stamnes, S., van Diedenhoven, B., Van Harten, G and Xu, F.: Intercomparison of biomass burning

aerosol optical properties from in situ and remote-sensing instruments in ORACLES-2016, Atmos. Chem. Phys., 19, 9181-9208, https://doi.org/10.5194/acp-19-9181-2019, 2019.

Pistone, K., Zuidema, P., Wood, R., Diamond, M., da Silva, A. M., Ferrada, G., Saide, P., Ueyama, R., Ryoo, J.-M., Pfister, L., Podolske, J., Noone, D., Bennett, R., Stith, E., Carmichael, G., Redemann, J., Flynn, C., LeBlanc, S., Segal-Rozenhaimer, M., and Shinozuka, Y.: Exploring the elevated water vapor signal associated with the free-tropospheric biomass burning plume over the southeast Atlantic Ocean, Atmos. Chem. Phys., 21, 9643–9668, https://doi.org/10.5194/acp-21-9643-2021, 2021.

Platnick, S., King, M., and Hubanks, P.: MODIS Atmosphere L3 Daily Product. NASA MODIS Adaptive Processing System, Goddard Space Flight Center, doi:10.5067/MODIS/MOD08_D3.006 (Terra), doi:10.5067/MODIS/MYD08_D3.006 (Aqua), 2015a.

Platnick, S., Ackerman, S. A., King, M. D., Meyer, K., Menzel, W. P., Holz, R. E., Baum, B. A. and Yang, P.: MODIS atmosphere L2 cloud product (06_L2), NASA MODIS Adaptive Processing System, Goddard Space Flight Center, dx.doi.org/10.5067/MODIS/MOD06_L2.006 (Terra), dx.doi.org/10.5067/MODIS/MYD06_L2.006 (Aqua), 2015b.

Platnick, S., Meyer, K. G., King, M. D., Wind, G., Amarasinghe, N., Marchant, B., Arnold, G. R., Zhang, Z., Hubanks, P. A., Holz, R. E., Yang, P., Ridgway, W., and Riedi, J.: The MODIS Cloud Optical and Microphysical Products: Collection 6 Updates and Examples From Terra and Aqua. IEEE Transactions on Geoscience and Remote Sensing, 55(1), 502–525. http://doi.org/10.1109/TGRS.2016.2610522, 2017.

Provencal, R., Gupta, M., Owano, T. G., Baer, D. S., Ricci, K. N., O'Keefe, A. and Podolske, J. R.: Cavity-enhanced quantum-cascade laser-based instrument for carbon monoxide measurements, Appl. Opt., 44(31), 6712, 2005.

Randles, C. A., da Silva, A. M., Buchard, V., Colarco, P. R., Darmenov, A., Govindaraju, R., Smirnov, A., Holben, B., Ferrare, R., Hair, J., Shinozuka, Y., and Flynn, C. J.,: The MERRA-2 Aerosol Reanalysis, 1980 Onward. Part I: System Description and Data Assimilation Evaluation, J. Climate, 30(17), 6823–6850, https://doi.org/10.1175/JCLI-D-16-0609.1, 2017.

Redemann, J., Wood, R., Zuidema, P., Doherty, S. J., Luna, B., LeBlanc, S. E., Diamond, M. S., Shinozuka, Y., Chang, I. Y., Ueyama, R., Pfister, L., Ryoo, J.-M., Dobracki, A. N., da Silva, A. M., Longo, K. M., Kacenelenbogen, M. S., Flynn, C. J., Pistone, K., Knox, N. M., Piketh, S. J., Haywood, J. M., Formenti, P., Mallet, M., Stier, P., Ackerman, A. S., Bauer, S. E., Fridlind, A. M., Carmichael, G. R., Saide, P. E., Ferrada, G. A., Howell, S. G., Freitag, S., Cairns, B., Holben, B. N., Knobelspiesse, K. D., Tanelli, S., L'Ecuyer, T. S., Dzambo, A. M., Sy, O. O., McFarquhar, G. M., Poellot, M. R., Gupta, S., O'Brien, J. R., Nenes, A., Kacarab, M., Wong, J. P. S., Small-Griswold, J. D., Thornhill, K. L., Noone, D., Podolske, J. R., Schmidt, K. S., Pilewskie, P., Chen, H., Cochrane, S. P., Sedlacek, A. J., Lang, T. J., Stith, E., Segal-Rozenhaimer, M., Ferrare, R. A., Burton, S. P., Hostetler, C. A., Diner, D. J., Platnick, S. E., Myers, J. S., Meyer, K. G., Spangenberg, D. A., Maring, H. and Gao, L.: An overview of the ORACLES (ObseRvations of Aerosols above Clouds and their intEractionS) project: aerosol-cloud-radiation interactions in the Southeast Atlantic basin, 21, 1507–1563, https://doi.org/10.5194/acp-21-1507-2021, 2021.

Reid, J. S., Koppmann, R., and Eck, T. F.: A review of biomass burning emissios part II: intensive physical properties of biomass burning particles, Atmos. Chem. Phys, 5, 799-825, doi:10.5194/acp-5-799-2005, 2005.

1890 Rienecker, M. M., Suarez, M. J., Todling, R., Bacmeister, J., Takacs, L., -C. Liu, H., Gu, W., Sienkiewicz, M., Koster, R. D., Gelaro, R., Stajner, I. and Nielsen, J. E.: The GEOS-5 Data Assimilation System— Documentation of Versions 5.0.1, 5.1.0, and 5.2.0, [online] Available from: https://gmao.gsfc.nasa.gov/pubs/docs/Rienecker369.pdf, 2008.

Rozendaal, M. A., Leovy, C. B., and Klein, S. A. (1995): An Observational Study of Diurnal Variations of Marine Stratiform Cloud, J. Climate, 8(7), 1795–1809, https://doi.org/10.1175/1520-0442(1995)008<1795:AOSODV>2.0.CO;2, 1995.

1895 Russell, P. B., Bergstrom, R. W., Shinozuka, Y., Clarke, A. D., DeCarlo, P. F., Jimenez, J. L., Livingston, J. M., Redemann, J., Dubovik, O., and Strawa, A.: Absorption Angstrom Exponent in AERONET and related data as an indicator of aerosol composition, Atmos. Chem. Phys., 10, 1155–1169, https://doi.org/10.5194/acp-10-1155-2010, 2010.

Ryoo, J.-M., Pfister, L., Ueyama, R., Zuidema, P., Wood, R., Chang, I., and Redemann, J.: A meteorological overview of the ORACLES (ObseRvations of Aerosols above CLouds and their intEractionS) campaign over the southeast Atlantic
1900 during 2016–2018: Part 1 - Climatology, Atmos. Chem. Phys. Discuss. [preprint], https://doi.org/10.5194/acp-2021-274, accepted, 2021.

Saide, P. E., Gao, M., Lu, Z., Goldberg, D. L., Streets, D. G., Woo, J.-H., Beyersdorf, A., Corr, C. A., Thornhill, K. L., Anderson, B., Hair, J. W., Nehrir, A. R., Diskin, G. S., Jimenez, J. L., Nault, B. A., Campuzano-Jost, P., Dibb, J., Heim, E., Lamb, K. D., Schwarz, J. P., Perring, A. E., Kim, J., Choi, M., Holben, B., Pfister, G., Hodzic, A., Carmichael, G. R.,
1905 Emmons, L., and Crawford, J. H.: Understanding and improving model representation of aerosol optical properties for a Chinese haze event measured during KORUS-AQ, Atmos. Chem. Phys., 20, 6455–6478, https://doi.org/10.5194/acp-20-6455-2020, 2020.

Sakaeda, N., Wood, R. and Rasch, P. J.: Direct and semidirect aerosol effect of southern African biomass burning aerosol, J. Geophys. Res. Atmos., 116(D12205), doi:10.1029/2010JD015540, 2011.

1910 Samset, B. H., Myhre, G., Schulz, M., Balkanski, Y., Bauer, S., Berntsen, T. K., Bian, H., Bellouin, N., Diehl, T., Easter, R. C., Ghan, S. J., Iversen, T., Kinne, S., Kirkevåg, A., Lamarque, J.-F., Lin, G., Liu, X., Penner, J. E., Seland, Ø., Skeie, R. B., Stier, P., Takemura, T., Tsigaridis, K., and Zhang, K.: Black carbon vertical profiles strongly affect its radiative forcing uncertainty, Atmos. Chem. Phys., 12, 2423-2434, doi:10.5194/acp-13-2423-2013, 2013.

Sand, M., Samset, B. H., Myhre, G., Gliß, J., Bauer, S. E., Bian, H., Chin, M., Checa-Garcia, R., Ginoux, P., Kipling, Z.,
1915 Kirkevåg, A., Kokkola, H., Le Sager, P., Lund, M. T., Matsui, H., van Noije, T., Remy, S., Schulz, M., Stier, P., Stjern, C. W., Takemura, T., Tsigaridis, K., Tsyro, S. G., and Watson-Parris, D.: Aerosol absorption in global models from AeroCom Phase III, Atmos. Chem. Phys., 21, 15929–15947, https://doi.org/10.5194/acp-21-15929-2021, 2021.

Schuster, G. L., Dubovi, O., and Holben, B. N.: Angstrom exponent and bimodal aerosol size distributions, J. Geophys. Res., 111, D07207, doi:10.1029/2005JD006328, 2006.

1920 Schwarz, J. P., Gao, R. S., Fahey, D. W., Thomson, D. S., Watts, L. A., Wilson, J. C., Reeves, J. M., Darbeheshti, M., Baumgardner, D. G., Kok, G. L., Chung, S. H., Schulz, M., Hendricks, J., Lauer, A., Kärcher, B., Slowik, J. G.,

Rosenlof, K. H., Thompson, T. L., Langford, A. O., Loewenstein, M. and Aikin, K. C.: Single-particle measurements of midlatitude black carbon and light-scattering aerosols from the boundary layer to the lower stratosphere, J. Geophys. Res., 111(D16), D16207, doi:10.1029/2006JD007076, 2006.

1925 Shank, L. M., Howell, S., Clarke, A. D., Freitag, S., Brekhovskikh, V., Kapustin, V., McNaughton, C., Campos, T., and Wood, R.: Organic matter and non-refractory aerosol over the remote Southeast Pacific: oceanic and combustion sources. Atmos. Chem. Phys., 12, 557-576, https://doi.org/10.5194/acp-12-557-2012 , 2012.

Shinozuka, Y., Saide, P. E., Ferrada, G. A., Burton, S. P., Ferrare, R., Doherty, S. J, Gordon, H., Longo, K., Mallet, M., Feng, Y., Wang, Q., Cheng, Y., Dobracki, A., Freitag, S., Howell, S. G., LeBlanc, S., Flynn, C., Segal-Rosenhaimer,

1930 M., Pistone, K., Podolske, J. R., Stith, E. J., Bennett, J. R., Carmichael, G. R., da Silva, A., Govindaraju, R., Leung, R., Zhang, Y., Pfister, L., Ryoo, J.-M., Redemann, J., Wood, R. and Zuidema, P.: Modeling the smoky troposphere of the southeast Atlantic: a comparison to ORACLES airborne observations from September of 2016, Atmos. Chem. Phys., 20, 11491-11526, https://doi.org/10.5194/acp-20-11491-2020, 2020.

Shipley, S. T., Tracy, D. H., Eloranta, E. W., Trauger, J. T., Sroga, J. T., Roesler, F. L. and Weinman, J. A.: High spectral

1935 resolution lidar to measure optical scattering properties of atmospheric aerosols. 1: Theory and instrumentation, Appl. Opt., AO, 22(23), 3716–3724, 1983.

Slingo, A. and Schrecker, H. M.: On the shortwave radiative properties of stratiform water clouds, Q. J. Roy. Meteor. Soc., 108, 407–426, 1982.

Stephens, M., Turner, N. and Sandberg, J.: Particle Identification by Laser-Induced Incandescence in a Solid-State Laser

1940 Cavity, Appl. Opt., 42(19), 3726–3736, 2003.

Stevens, B., and Feingold, G.: Untangling aerosol effects on clouds and precipitation in a buffered system, Nature, 461, 607-613, 10.1038/nature08281, 2009.

Stier, P., Schutgens, N. A. J., Bellouin, N., Bian, H., Boucher, O., Chin, M., Ghan, S., Huneeus, N., Kinne, S., Lin, G., Ma, X., Myhre, G., Penner, J. E., Randles, C. A., Samset, B., Schulz, M., Takemura, T., Yu, F., Yu, H., and Zhou, C: Host

1945 model uncertainties in aerosol radiative forcing estimates: Results from the AeroCom Prescribed intercomparison study. Atmos. Chem. Phys., 13, 3245–3270, https://doi.org/10.5194/acp-13-3245-2013, 2013.

Tang, I. N., Tridico, A. C., and Fung, K. H.: Thermodynamic and optical properties of sea salt aerosols, J. Geophys. Res.-Atmos., 102, 23269–23275, https://doi.org/10.1029/97jd01806, 1997.

Taylor, J. W., Wu, H., Szpek, K., Bower, K., Crawford, I., Flynn, M. J., Williams, P. I., Dorsey, J., Langridge, J. M.,

1950 Cotterell, M. I., Fox, C., Davies, N. W., Haywood, J. M., and Coe, H.: Absorption closure in highly aged biomass burning smoke, Atmos. Chem. Phys., 20, 11201-11221, https://doi.org/10.5194/acp-20-11201-2020, 2020.

Titos, G., Cazorla, A., Zieger, P., Andrews, E., Lyamani, H., Granados-Muñoz, M. J., Olmo, F. J., and Alados-Arboledas, L.: Effect of hygroscopic growth on the aerosol light-scattering coefficient: A review of measurements, techniques and error sources, Atmos. Env., 141, 494-507, https://doi.org/10.1016/j.atmosenv.2016.07.021, 2016.

1955 Trenberth, K. E., Fasullo, J. T., and Kiehl, J.: Earth's global energy budget, Bull. Amer. Met. Soc., 311-324, https://doi.org/10.1175/2008BAMS2634.1, March, 2009.

Twohy, C. H., Anderson, J. R., Toohey, D. W., Andrejczuk, M., Adams, A., Lytle, M., George, R. C., Wood, R., Saide, P., Spak, S., Zuidema, P., and Leon, D.: Impacts of aerosol particles on the microphysical and radiative properties of stratocumulus clouds over the southeast Pacific Ocean, Atmos. Chem. Phys., 13, 2541–2562, 1960 https://doi.org/10.5194/acp-13-2541-2013, 2013.

Twomey, S.: The Influence of Pollution on the Shortwave Albedo of Clouds, J. Atmos. Sci., 34(7), 1149–1152. https://doi.org/10.1175/1520-0469(1977)034<1149:TIOPOT>2.0.CO;2, 1977.

van Marle, M. J. E., Kloster, S., Magi, B. I., Marlon, J. R., Daniau, A.-L., Field, R. D., Arneth, A., Forrest, M., Hantson, S., Kehrwald, N. M., Knorr, W., Lasslop, G., Li, F., Mangeon, S., Yue, C., Kaiser, J. W., and van der Werf, G. R.: Historic 1965 global biomass burning emissions for CMIP6 (BB4CMIP) based on merging satellite observations with proxies and fire models (1750–2015), Geosci. Model Dev., 10, 3329–3357, https://doi.org/10.5194/gmd-10-3329-2017, 2017.

Várnai, T., and Marshak, A.: Observations of three-dimensional radiative effects that influence MODIS cloud optical thickness retrievals, J. Atmos. Sci., 59(9), 1607–1618. http://doi.org/10.1175/1520-0469(2002)059<0668:LTTAIR>2.0.CO;2, 2002.

1970 Virkkula, A.: Correction of the Calibration of the 3-wavelength Particle Soot Absorption Photometer (3λ PSAP), Aerosol Sci. Technol., 44(8), 706–712, 2010.

Wagstrom, K. M. and Pandis, S. N.: Determination of the age distribution of primary and secondary aerosol species using a chemical transport model, J. Geophys. Res. 114, doi:10.1029/2009jd011784, 2009.

Werner, F., Wind, G., Zhang, Z., Platnick, S., Di Girolamo, L., Zhao, G., Amarasinghe, N. and Meyer, K.: Marine boundary 1975 layer cloud property retrievals from high-resolution ASTER observations: case studies and comparison with Terra MODIS. Atmos. Meas. Tech., 9(12), 5869–5894. http://doi.org/10.5194/amt-9-5869-2016, 2016.

Wilcox, E. M.: Stratocumulus cloud thickening beneath layers of absorbing smoke aerosol, Atmos. Chem. Phys., 10(23), 11769–11777. http://doi.org/10.5194/acp-10-11769-2010, 2010.

Wild, M., Hakuba, M. Z., Folini, D., Dörig-Ott, F., Schär, C., Kato, S., and Long, C. N.: The cloud-free global energy 1980 balance and inferred cloud radiative effects: an assessment based on direct observations and climate models, Climate Dyn., 52:4787–4812 https://doi.org/10.1007/s00382-018-4413-y, 2019.

Wilson, D. R., Bushell, A. C., Kerr-Munslow, A. M., Price, J. D. and Morcrette, C. J.: PC2: A prognostic cloud fraction and condensation scheme. I: Scheme description, Q.J.R. Meteorol. Soc., 134(637), 2093–2107, 2008.

Wood, R., Bretherton, C. S., and Hartmann, D. L.: Diurnal cycle of liquid water path over the subtropical and tropical 1985 oceans, Geophys. Res. Lett., 29(23), 7-1–7-4. https://doi.org/10.1029/2002GL015371, 2002.

Wood, R.: Stratocumulus Clouds, Mon. Weather Rev., 140, 2373–2423, https://doi.org/10.1175/MWR-D-11-00121.1, 2012.

Wyant, M. C., Bretherton, C. S., Chlond, A., Griffin, B. M., Kitagawa, H., Lappen, C.-L., Larson, V. E., Lock, A., Park, S., Roode, S. R. de, Uchida, J., Zhao, M., & Ackerman, A. S.: A single-column model intercomparison of a heavily

drizzling stratocumulus-topped boundary layer. J. Geophys. Res. Atmos., 112(D24), https://doi.org/10.1029/2007JD008536, 2007.

Yang, Y., and L. Di Girolamo: Impacts of 3-D radiative effects on satellite cloud detection and their consequences on cloud fraction and aerosol optical depth retrievals, J. Geophys. Res., 113, D04213, https://doi.org/ 10.1029/2007JD009095, 2008.

Zhang, G. J. and McFarlane, N. A.: Sensitivity of climate simulations to the parameterization of cumulus convection in the Canadian climate centre general circulation model, Atmosphere-Ocean, 33(3), 407–446, 1995.

Zhang, J. and Zuidema, P.: Sunlight-absorbing aerosol amplifies the seasonal cycle in low-cloud fraction over the southeast Atlantic, Atmos. Chem. Phys., 21, 11179–11199, https://doi.org/10.5194/acp-21-11179-2021, 2021.

Zhang, Y., Chen, Y., Fan, J. and Leung, L.-Y. R.: Application of an Online-Coupled Regional Climate Model, WRF-CAM5, over East Asia for Examination of Ice Nucleation Schemes: Part II. Sensitivity to Heterogeneous Ice Nucleation Parameterizations and Dust Emissions, Climate, 3(3), 753–774, 2015a.

Zhang, Y., Zhang, X., Wang, K., He, J., Leung, L. R., Fan, J. and Nenes, A.: Incorporating an advanced aerosol activation parameterization into WRF-CAM5: Model evaluation and parameterization intercomparison: An Advanced Aerosol Activation Scheme, J. Geophys. Res. D: Atmos., 120(14), 6952–6979, 2015b.

Zhao, G., and Di Girolamo, L.: Cloud fraction errors for trade wind cumuli from EOS-Terra instruments, Geophys. Res. Lett., 33, L20802, doi:10.1029/2006GL027088, 2006.

Zhou, J., Xu, X., Zhao, W., Fang, B., Liu, Q., Cai, Y., Zhang, W., Venables, D. S., and Chen, W.: Simultaneous measurements of the relative-humidity-dependent aerosol light extinction, scattering, absorption, and single-scattering albedo with a humidified cavity-enhanced albedometer, Atmos. Meas. Tech., 13, 2623–2634, https://doi.org/10.5194/amt-13-2623-2020, 2020.

Zhu, P., Bretherton, C. S., Köhler, M., Cheng, A., Chlond, A., Geng, Q., Austin, P., Golaz, J.-C., Lenderink, G., Lock, A., and Stevens, B.: Intercomparison and interpretation of single-column model simulations of a nocturnal stratocumulus-topped marine boundary layer. Mon. Weath. Rev., 133(9), 2741–2758, https://doi.org/10.1175/MWR2997.1, 2005.

Zuidema, P., Redemann, J., Haywood, J., Wood, R., Piketh, S., Hipondoka M., and Formenti, P.: Smoke and clouds above the Southeast Atlantic, BAMS, 1131-1135, https://doi.org/10.1175/BAMS-D-15-00082.1, 2016.